Microsystem-Compatible Heterogeneous Micro-Hydrophone for Use at High Static Pressures

by

Andrew S. Trickey-Glassman

A dissertation submitted in partial fulfillment
of the requirements for the degree of
Doctor of Philosophy
(Electrical and Computer Engineering)
in the University of Michigan
2019

Doctoral Committee:

Professor Yogesh B. Gianchandani, Chair
Associate Professor Tao Li, University of Cincinnati
Associate Professor Becky Peterson
Professor Yin Lu Young

Andrew S. Trickey-Glassman

trickey@umich.edu

ORCID iD: 0000-0001-8331-5996

Acknowledgements

I would like to express deep appreciation for my research adviser, Prof. Yogesh B. Gianchandani. His tireless effort, vision, dedication, research ability, and countless hours of instruction helped me advance my research as well as my personal development. His mentorship was invaluable. I always felt like part of a family during my time in Ann Arbor. I am also thankful to Prof. Tao Li. Tao is one of the brightest people I know, and I learned an incredible amount during my time with him. I am also thankful for the rest of my committee, Prof. Julie Young and Prof. Becky Peterson, for their keen research interest, expert guidance, and feedback.

I would like to thank my fellow lab mates and researchers at the University of Michigan. Neeharika, Alex, Scott, Yutao, Yushu, Xin, Shiyang, Qisen, Jiqing, Ramprasad, Johnny, Weilin, Tsenguun, Leo, Daniel, Amin, Tal, Sajal, Behnoosh, Farzad, Chris, Yu Heng, and many others. You made my Ph.D. journey a stimulating and enjoyable experience.

I'd also like to thank my friends, who make life so bright and are always there for me. Josh, Nick, Mia, Liz, T. Rex, Mark, Nebibe, Juan, Avish, Armin, Steven, Scott and many others. My time here in Ann Arbor has been a blast with all of you! Richie, Jamesy, Juan(cho), Dave, Jack, Greg, Brent, Nick, Steve, and other friends I've been lucky enough to keep in touch with over the years; here's to many more!

Lastly, and most importantly, I want to thank my family. My Ph.D. journey would not have been a possibility without the tireless love and support from my parents, Richard and Elizabeth. You guys are the best. I also want to thank my amazing big sister Arden, who was the best role model I could've possibly asked for. Thank you.

Table of Contents

List of Figures

List of Tables

List of Appendices

List of Symbols

A Electrode area

a Radius, is used for diaphragm radius as well as acoustic waveguide tube radius

α Angle of incidence for a planar wave propagating through a waveguide

C_{dia} Diaphragm compliance

C_F Feedback capacitor

C_i Op amp self input capacitance

C_0 Baseline capacitance

C_{par} Parasitic capacitance

C_{tot} Total amplifier capacitance at input node

c Speed of sound

c_{avg} Average experimentally measured speed of sound

c_p Phase speed

d_{nom} Nominal diaphragm deflection

d_0 Undeflected interelectrode gap

E Young's modulus

ε_0 Permittivity of free space

ε_r Relative permittivity

F Harmonic force

f Frequency

f_c Corner frequency

f_{co} Acoustic cutoff frequency

$\overline{f_n^2}$ Mean square noise force spectral density

ϕ Potential function used in classical wave equation

ϕ_{em} Mechanical to electrical transduction coefficient

ϕ_{me} Electrical to mechanical transduction coefficient

γ Figure of merit

H_1 First order Struve function

H Acoustic beam profile of ultrasonic acoustic transmitter

J_0 Zeroth order Bessel function of the first kind

J_1 First order Bessel function of the first kind

j_{1m} Value for the mth root of the first order Bessel function of the first kind

K Bulk modulus

k Wave number

k_r Wave number in radial axis

k_s Spring softening constant

k_z Wave number in z (longitudinal) axis

L Waveguide tube length or acoustic distance, context dependent

m_{dia} Diaphragm mass

P Static pressure

P_{ax} Axial acoustic pressure magnitude of ultrasonic acoustic transmitter

p Acoustic pressure

$\overline{p_{nr}^2}$ Total mean square radiation noise pressure spectral density

Q Electrical charge

R_1 Piston resistance function

R Incremental response

R_B Bias resistor

r_m Distance of the mth zero of axial acoustic pressure magnitude

ρ Density

R_{dia} Diaphragm mechanical resistance

R_n Incremental response of the nth sensing element

R_r Radiation resistance

R_{rn} Radiation resistance of the nth sensing element

R_{tot} Total sensor incremental response

S Diaphragm area

S_n Diaphragm area of the nth sensing element

s Diaphragm spring constant

σ Diaphragm stress

T Temperature

T_I Transmitted acoustic intensity

t Diaphragm thickness or time, context dependent

t_{ac} Acoustic time of flight

θ Angle from acoustic axis, ultrasonic acoustic transmitter

U_L Uncertainty due to acoustic distance measurement (in)accuracy

U_0 Velocity magnitude

$\dot{u}$ Lumped diaphragm velocity

υ Poisson's ratio

V Volume or voltage, context dependent

V_B Bias voltage

V_{DC} Static voltage

V_S Supply voltage

ω Radial frequency

X_1 Piston reactance function

Z_{dia} Diaphragm mechanical impedance

Z_F Feedback loop electrical impedance

Z_i Electrical impedance of electrical components at input

Z_{m0} Pressure vessel input mechanical impedance

Z_{mp} Pressure vessel plate mechanical impedance

Z_{ms} Stack actuator mechanical impedance

Z_{mtot} Total mechanical resistance

Z_r Diaphragm radiation impedance

z Characteristic acoustic impedance or longitudinal axis, context dependent

Abstract

Underwater acoustic sensing is important for multiple applications, including seismic sensing for the oil and gas industry, SONAR at extended ocean depth, localization of underwater vehicles, implementation in autonomous microsystems, and marine mammal research, to name a few; however, there is a lack of hydrophones that can operate at ambient pressures in the range of 5-50 MPa while still offering a miniature form factor, compatibility with lithographic manufacturing methods, and compatibility with autonomous microsystems. A miniature, high pressure hydrophone should additionally provide high sensitivity and sufficient bandwidth for a given application, while being immune to corrosive brines, debris, and water contamination.

Recently, a sapphire-based micromachining process was reported that shows promise in addressing these concerns. The thin-film MEMS process uses surface micromachining technology to create hermetically vacuum sealed, variable gap capacitive sensing elements with touch mode capability that eliminates element rupture due to pressure overloading. An insulating sapphire substrate provides low parasitic capacitance that allows for electrical connectivity in parallel for high sensitivity. The primary focus of this report is to investigate the suitability of this process flow for fabrication of micro hydrophones that satisfy the above criteria, as well as to demonstrate use of the sensor in several applications of interest.

The surface micromachined micro-hydrophone utilizes a heterogeneous arrayed architecture to provide high responsivity (up to 3.0 pF/MPa) over a wide range of static pressures (≥50 MPa) while maintaining a miniature form factor (1.4 × 1.6 × 0.5 mm^3). The sensor, H106,

uses 106 multiply sized sensing elements with diaphragms ranging from ϕ104 μm to ϕ56 μm. Experimental characterization was performed to verify the static pressure response (up to 34.406 pF capacitance change) over a pressure range of 50 MPa, verify repeatability, quantify how responses change over time, and verify sensor bandwidth in air and paraffin oil (Enerpac™ LX101). The first diaphragm resonances in air and oil were experimentally verified to occur at 4.105 MHz and 2.319 MHz, respectively, at atmospheric pressure.

Hydrophone operation in an autonomous, battery operated microsystem, intended for application to oil and gas exploration, was demonstrated through sensor-system integration and manipulation of existing microcontroller (MCU) programming. Static pressure sensing capability was demonstrated at up to 50 MPa, with sub-psi resolution throughout the entire static pressure range. Seismic sensing capability was demonstrated using pressure waves as large as 100 psi in ambient pressure levels up to 50 MPa and frequency up to 100 Hz. Minimum detectable pressure (MDP) at frequency was also quantified at several different static pressures and is below 0.1 psi over nearly the entire static pressure range above 2 Hz.

The sensor's potential use as a deep-sea hydrophone was demonstrated through integration with a custom charge amplifier circuit. The circuit provides a 3-dB bandwidth up to 8.9 MHz. All testing was performed in paraffin oil. The sensor was calibrated at atmospheric pressures up to 100 kHz frequency (-221 +/- 1.9 dB re V/μPa, 10V bias). Response up to 2 MHz was also demonstrated using a pulse-echo procedure. Flat band hydrophone sensitivity was experimentally characterized at up to 50 MPa static pressure. Lastly, noise power spectral density and resulting MDP were characterized (24.5 mPa/√Hz, 1 kHz, 1 atm, 40V bias). Bandwidth, form factor, and static pressure rating in particular compare extremely favorably to existing hydrophones.

Chapter 1: Introduction

1.1 Motivation

Acoustic sensors operate by converting sound pressure waves into a more easily measurable signal, such as electricity. Virtually all acoustic sensors respond to impinging pressure waves with a mechanical deflection, which changes a measurable property of the sensor. Underwater acoustic sensors, hereby referred to as hydrophones, are useful in several applications including extended ocean depth [Cra03, Kil11, Bag06, Sul78], seismic sensing applications [Cra03, Sin81], acoustic remote sensing [Dow15], medical ultrasound [Cian06, Erg03, Har88], and lithotripsy [Gra89, Col98, Jam15, Fil90, Sta93, Ino91]. Sound Navigation and Ranging (SONAR) is a common necessity in naval vehicles, and typically requires bandwidth ranging from several hertz to 10's of kilohertz [Moo10a] and in some cases up to several hundred kilohertz [Bjø13].

Hydrophones are acoustic sensors designed for operation in underwater environments. This introduces several distinct design challenges: an ideal hydrophone must (1) be able to withstand extremely high hydrostatic pressures without significant change in performance; (2) sense pressure waves with magnitudes much smaller than, and in some cases much larger than, the acting hydrostatic pressure; (3) be protected from corrosive and performance degrading environmental factors, such as water, debris, hydrocarbons, brine, and other chemicals; (4) maintain reasonable bandwidth despite added dynamic mass loading from an underwater environment; (5) maintain reasonable thermal-mechanical noise despite increased density and viscosity of water compared to air; and (6) in some cases provide sufficient sensitivity to

accommodate large parasitic capacitances associated with long electrical cables. Hydrophone design challenges are considerable.

Accommodating ambient pressure and heavy fluid loading is a significant challenge that leaves room for improvement among existing hydrophones. The most common method for accommodation is fluid balancing over the sensitive elements; in other words, the sensor is designed and packaged in such a way that ambient pressure can equalize across the sensing diaphragm, eliminating static deflections and most stresses that could alter performance or could even destroy the sensor. Although this method is intuitive, it has notable drawbacks. The most relevant to this work is the inevitably bulky nature of the packaging. Other major issues are increased thermal mechanical noise due to fluid interaction with the balanced sensing element, vulnerability to shockwaves, and in some cases increased temperature coefficients. Furthermore, some applications require static pressure response, which is not supported by this method.

Autonomous microsystems for application to oil and gas exploration are being developed to collect downhole static pressure and temperature data *in situ*. The addition of acoustic sensing capability to these systems could provide significant benefit: supplementary data for seismic imaging, real-time communication with the surface, and even geolocation are made possible. Such an application demands a sensor with form factor, packaging compatibility, and a static pressure rating not provided by currently available hydrophones. Furthermore, the ability to sense static pressure is prized in this application due to the limited size and power afforded by the microsystems. With a promising new microfabrication process in hand, the goal of this work is to develop and characterize a hydrophone sensor for use in an existing autonomous microsystem, and to demonstrate its use in other applications in which hydrophones are commonly used.

1.2 Background

1.2.1 Autonomous Sensing Microsystems

Autonomous sensing microsystems are functional, miniaturized systems that consist of integrated sensors, typically based on Micro Electromechanical Systems (MEMS) technology. These systems are designed to be deployed in an environment of interest for data collection. Microsystems usually use a wireless communication interface, micropower circuits, embedded power sources, and hermetic packaging [Wis09]. Data is oftentimes collected and stored in flash memory using a microcontroller unit (MCU). Recent applications for autonomous sensing microsystems include healthcare [Wis09] as well as harsh environmental sensing [Wij11]. Configuration of a typical microsystem architecture is shown in Fig. 1. 1. Sensors and/or actuators are packaged along with an MCU, battery, components for wireless communication, as well as an energy harvester. Packaging is a critical aspect of any microsystem; some degree of hermeticity is required, while still allowing mechanical and electrical interactions with the

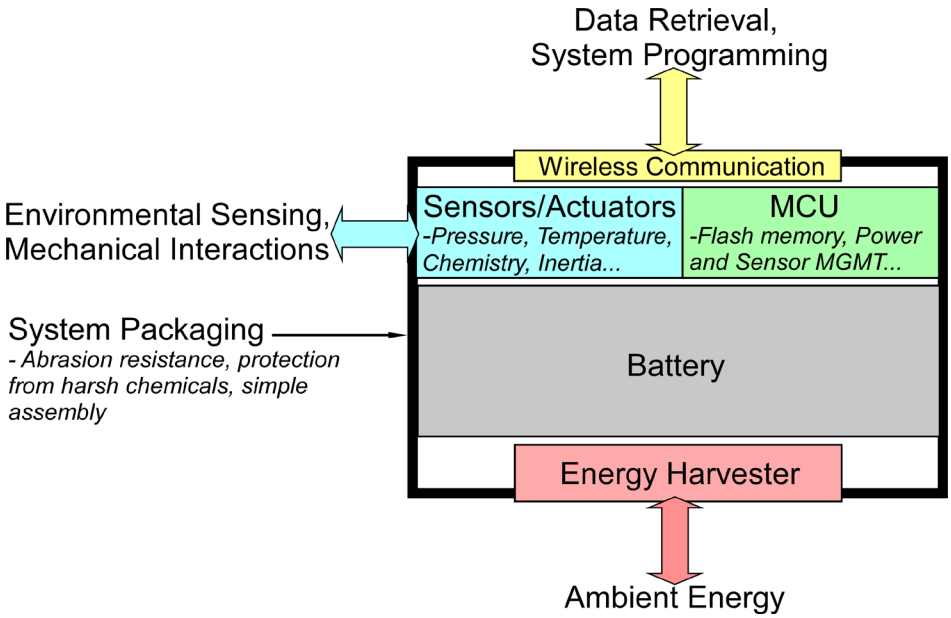

Fig. 1. 1: Configuration of a typical microsystem. Sensors and/or actuators along with a processing unit and power supply are fitted in packaging necessary for a specific application. The systems are interrogated wirelessly and must have an ability to harvest energy for reuse.

environment. In some applications, the packaging must withstand incredible pressures and harsh chemicals. Another critical aspect of the microsystem architecture is wireless communication. Wireless interrogation is the preferred method of data retrieval to preserve packaging integrity. RF communication is a common method [Cho17, Smi07, Sus05], as well as optical communication [Cho17]. Communication systems can also be used for harvesting energy to be stored in onboard batteries for system reusability.

A commercially viable application of autonomous microsystems is for use in harsh environmental sensing, with major industry influence flowing towards oil and gas exploration. In hydrofracturing processes, acquisition of well monitoring data such as temperature, pressure, resistivity, and chemical concentration is necessary for increasing well efficiency, extending well life, increasing safety, and lowering the cost of operation [Cha12, Fin10, Wod11, Yu12].

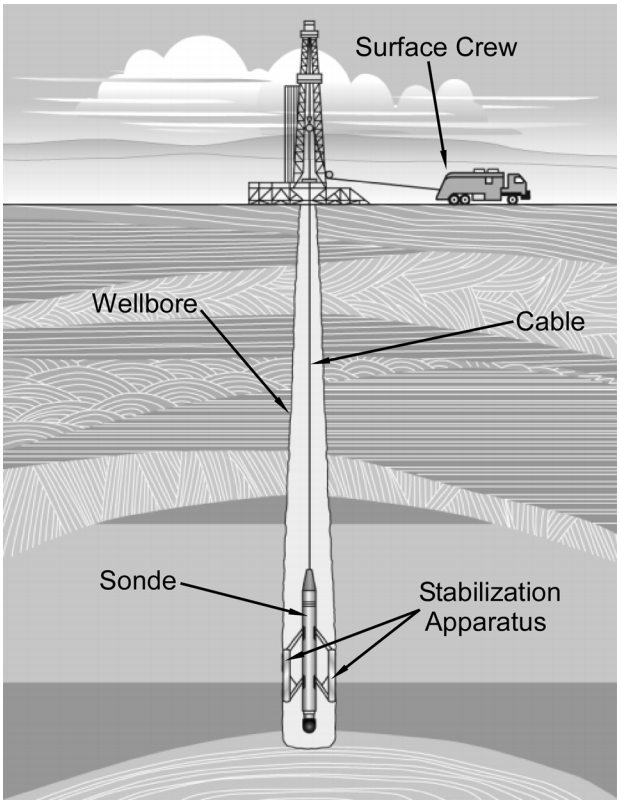

Fig. 1.2: Schematic of a wireline monitoring operation. A sonde is lowered into the wellbore to monitor well conditions such as temperature, pressure, and resistivity. Modified from [Ell07], original image courtesy of Schlumberger.

Traditional means of well monitoring involve long, electrically conductive cables that lower into the wellbore. Developed in the 1920s, wireline monitoring is a prominent method of well monitoring that involves lowering a measurement instrument, or *sonde*, into the wellbore via cable and winch (Fig. 1.2) [Ell07]. Sondes are typically under 4 inches in diameter to facilitate use in wellbore openings as small as 6 inches across. Their length is dependent on the array of integrated sensors; tool strings upto 100 ft in length have been reported [Ell07]. Each sonde typically requires some stabilization apparatus, such as a bow-spring or hydraulically actuated arm, to maintain a specific radial location in the wellbore. Wireline monitoring instruments with integrated sensors can be utilized with electrically conductive cables that transfer data to the surface, while some have integrated processing units that store data and are read out via USB once returning to the surface. Pressure, temperature, and resistivity measurements can be made at over 100 Hz (see products from OpenField^{TM} Technology), and are useful for geological mapping of the subsurface, evaluating hydrocarbon potential of a reservoir, and providing complementary data for seismic analysis among other things [Ell07]. Despite widespread use in the oil and gas industry, wireline monitoring data can only be collected near the wireline. This leaves a need for data collection inside fractures as well as deep into the reservoir.

Wireline monitoring and other techniques such as seismic analysis [Mar14] and crosswell imaging [Sch06, Mar14] can be supplemented with autonomous sensing microsystems. Autonomous microsystems have a distinct advantage in being able to collect data throughout the entire wellbore and show promising trends in miniaturization to eventually provide data directly from inside fractures. Large numbers of autonomous microsystems can be flowed into the wellbore using a fluid medium (Fig. 1. 3). There are few existing microsystems for harsh environmental sensing applications. The University of Tulsa and Saudi Aramco developed a 7.5

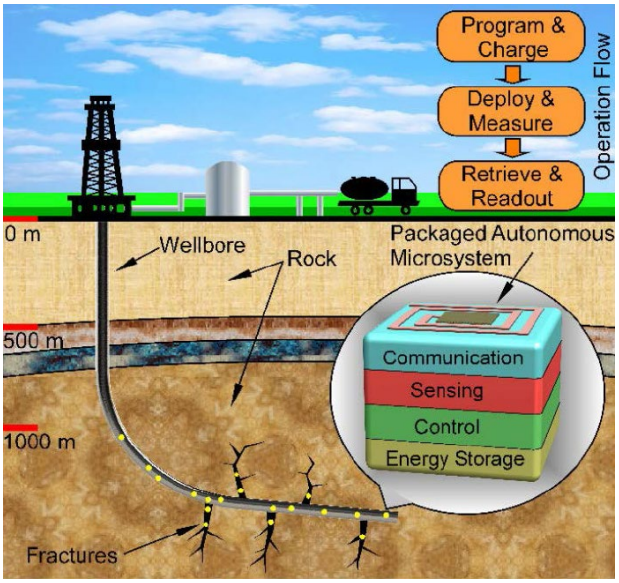

Fig. 1. 3: Deployment of packaged autonomous microsystems in a wellbore. Image courtesy of Dr. Yu Sui.

mm system encapsulated in a spherical polymer packaging, for temperature and pressure monitoring in downhole environments [Yu12, Shi15]. OpenField^{TM} Technology has also developed a pressure and temperature monitoring microsystem encased in a 50.8 mm spherical titanium shell that can flow through well pipes [Ope13].

Integration of a micro-hydrophone with downhole microsystems can provide several functions. The hydrophone-equipped microsystem could be used to provide supplementary data to assist in seismic imaging [Mar14]. Seismic sources are routinely used in the oil and gas industry for reflection seismology, which uses acoustic waves to image rock layers. Another possibility is real-time communication with the surface. Naturally occurring down-hole liquid consists of harsh brines that attenuate RF communications to the diameter of the micro-antenna. As a result, current microsystem technology is not capable of sending a wireless signal directly to the surface [Cha12]. However, acoustic waves travel freely through the environment of interest. An acoustic source at the surface could therefore be used to send commands to the microsystem when it is deployed downhole. Yet another possibility is geolocation. A

hydrophone could be used to record simple time of flight measurements from three seismic sources; such information could triangulate the system to provide location data.

1.2.2 Existing Hydrophone Technologies

The most prominent transduction techniques for underwater acoustic detection are piezoelectric, capacitive, optical, and piezoresistive. Piezoelectric sensors are widely used due to their high sensitivity, low power requirements, and low temperature coefficients. They do not, however, have a static pressure response. Capacitive hydrophones can provide high sensitivity, low temperature coefficients, and are capable of static response depending on implementation, but require interface circuitry to be close to the sensor and are not typically accommodating to high static pressures. Optical hydrophones offer high performance but require additional transduction within a complex interface. Piezoresistive hydrophones offer improved low frequency response compared to piezoelectric devices, but do not offer low temperature coefficients. Piezoresistive hydrophones are capable of static response depending on implementation.

Piezoelectric Hydrophones

Piezoelectric materials create an electric field in response to applied mechanical force, and vice versa. Generation of an electric field from applied force is known as the direct piezoelectric effect, while the opposite is the converse piezoelectric effect. Piezoelectric transduction is attractive for use in MEMS applications due to low hysteresis, high available energy densities, high sensitivity, and low power requirements [Tro04]. Notably, piezoelectric acoustic sensors do not require a power input other than that needed by readout circuitry.

The most commonly used piezoelectric materials are lead zirconate titanate (PZT), AlN, polyvinylidene fluoride (PVDF), and ZnO. PZT was developed for high piezoelectric coupling coefficients, with little focus on improving other characteristics. PZT can be deposited by sputtering [Ino03], sol-gel deposition [Amb10], and metal oxide chemical vapor deposition (MOCVD) [Li97]. AlN is most commonly deposited by sputtering [Rez13], and, unlike PZT, is compatible with CMOS processes. ZnO is also usually deposited by sputtering [Tro04] and is not CMOS compatible. It can also be difficult to deposit ZnO with a reasonably high resistivity, which leads to charge leakage issues in applications under 10 kHz. Such applications typically require deposition of an insulating layer such as SiO2 [Che80, Lit10, Tro04]. PVDF is a polymeric material that is often used in underwater ultrasonic sensing applications with wide bandwidth [Lum96, Dae16, Gra89]. PVDF has an acoustic impedance close to that of water, making it a desirable material for high frequency applications *in vivo* [Dae16, Pla87]. Piezoelectric composites are also commonly used to overcome the poor coupling efficiency in piezoelectric ceramics due to acoustic impedance mismatch [Lee14].

Piezoelectric hydrophones are ideal in many cases due to thermal stability and absence of vulnerable components, such as an interelectrode gap. However, piezoelectric transducers do not offer a DC response, which is a desirable attribute for use in an autonomous microsystem. Furthermore, hydrostatic mass loading can easily cause ruptures in devices that employ a diaphragm. Moon *et al.* [Moo10a, Moo10b] presented a micromachined piezoelectric hydrophone that utilizes hydrostatic air backing, as seen in Fig. 1. 4. As mentioned previously, this technique is extremely common and results in bulky packaging. This hydrophone uses a 3 μm thick layer of PZT deposited on a 10 μm thick silicon diaphragm, 1400 μm in diameter, using the sol-gel method [Amb10]. A 300 μm thick silicon substrate is anodically bonded to a Pyrex

7740 glass wafer. The hydrophone is sealed inside a rubber housing, along with castor oil (Fig. 1. 4(c)). The backside microchannel and backchamber are filled with air. As hydrostatic pressure increases, so does pressure inside the housing. Oil enters the inlet port and increases air pressure, which in turn equilibrates pressure over the diaphragm. Experimental testing shows a sensitivity of -227 dB re 1 V/μPa (at 2 kHz) and a demonstrated bandwidth of 100 Hz to approximately 10 kHz. Units of hydrophone sensitivity are by convention in decibels, with 0 dB = 1 V/μPa. Hydrophone characterization was performed at up to 1.5 MPa hydrostatic pressure, which is above the rupture pressure of the diaphragm without pressure equalization.

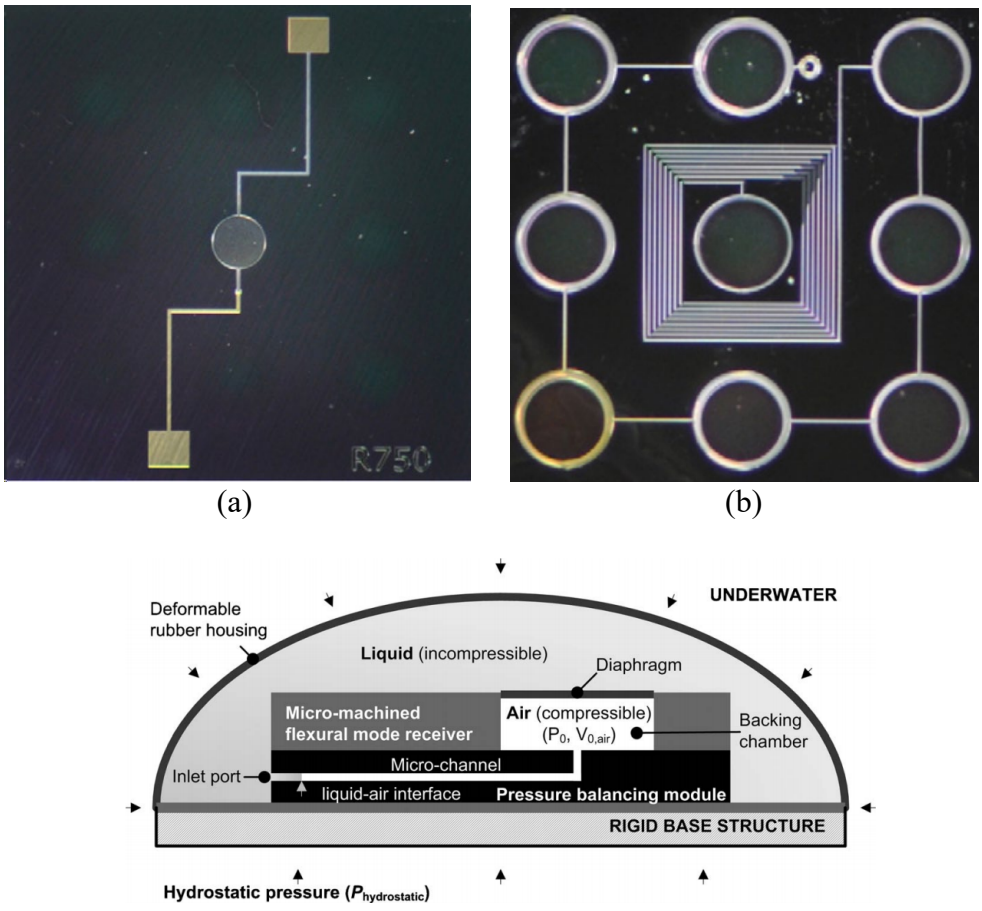

Fig. 1. 4: Hydrostatically balanced hydrophone presented by Moon et al. [Moo10a, Moo10b]. (a) Optical image of device frontside, with diaphragm and contact pads visible. (b) Optical image of device backside showing micro channel, diaphragm, and auxiliary chambers. (c) Schematic of pressure balancing system.

Acoustic imaging transducers are commonly made with piezoelectric materials, particularly PVDF. Daeichin *et al.* [Dae16] presented such a hydrophone for intravascular photoacoustic imaging. A commercial PVDF film 52 μm in thickness was laser micromachined into a 0.6 × 0.6 mm2 element and integrated onto a custom integrated circuit. The hydrophone frequency response was flat within 10 dB from 1 MHz to 15 MHz, with a maximum sensitivity of -225 dB re 1 V/μPa. Integrated RMS output noise voltage from 1 MHz to 20 MHz limited the minimum detectable pressure to 30 Pa. Lum *et al.* [Lum96] presented a high frequency hydrophone for characterization of acoustic fields generated by similar medical ultrasound imagers and is suitable for calibrating devices operating in the 10 to 40 MHz range. The sensitive PVDF-TrFE (trifluoroethylene) element was limited in size to minimize averaging of acoustic pressure, which can lead to underestimation of the spatial-peak acoustic pressure. A 4 μm thick film of spot-poled PVDF-TrFE with on-membrane electronics provides a -3 dB bandwidth above 150 MHz and an effective spot diameter of 100 μm. The hydrophone yielded a sensitivity of -263 dB re 1 V/μPa from 5 to 20 MHz. Response was not characterized at higher frequencies due to absence of a suitable calibration technique.

Capacitive Hydrophones

Capacitive, also known as condenser, hydrophones consist of two electrodes that form a variable gap capacitor. One of the electrodes is normally perforated to facilitate fluid flow. Acoustic pressure waves change the interelectrode gap and hence the device capacitance, which generates a measurable voltage, current, or frequency output signal [Ber92]. A polarization voltage is usually applied across the electrodes, the magnitude of which generally has major effect on device sensitivity. Condenser hydrophones are particularly vulnerable to debris inside the interelectrode gap, which can alter or even destroy the device's response. Performance is also

dependent on the relative dielectric constant of the fluid between the electrodes. Capacitive sensors in general are known for high pressure sensitivity, low noise, and low temperature sensitivity [Kim12, Aka01, He07, Cha01, Par03]. Interface circuitry is also readily available, which facilitates microsystem integration.

Condenser hydrophones are not usually sealed at vacuum because hydrostatic pressure would deflect the sensing electrode, making a constant change in interelectrode gap. This profoundly changes device performance and poses risk of rupturing the diaphragm. Additionally, the sensor could short if uninsulated electrodes contact each other. Fig. 1. 5 shows the cross section of a generic variable gap capacitive acoustic sensor. This configuration is commonly employed in microphones. The baseline capacitance of the depicted device can be approximated by

$$C_0 = \frac{\varepsilon_r \varepsilon_0 A}{d_0}, \tag{1.1}$$

where ε_r is the relative dielectric constant, ε_0 is permittivity of free space, A is electrode area, and d_0 is the interelectrode gap with no diaphragm deflection. Incoming pressure waves cause diaphragm deflection d, which changes the device capacitance by a measurable amount. Various readout techniques have been reported for capacitive acoustic sensors [Sen01]. To reduce

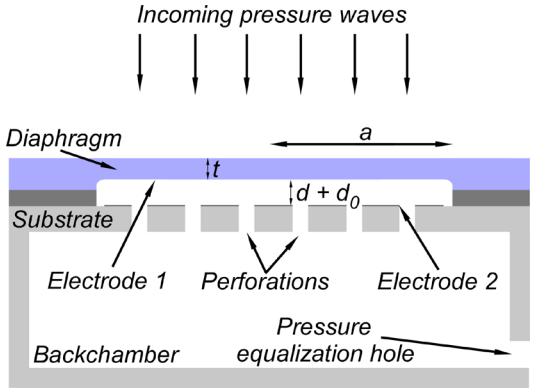

Fig. 1. 5: Cross section of a generic variable gap capacitive acoustic sensor. Incoming pressure waves deflect the diaphragm, which changes the interelectrode gap d_0. Backplate perforations allow free movement of fluid to reduce damping and thermal mechanical noise. Pressure equalization negates deflection caused by static pressure.

frequency response limitations caused by fluid damping, thermal mechanical noise, and to equilibrate pressure, perforations are commonly added to one of the electrodes [Sch94], as shown in Fig. 1. 5.

Notable work on capacitive hydrophones is presented by Bernstein [Ber92] and White *et al.* [Whi05]. Bernstein developed a micromachined capacitive hydrophone that is encapsulated in a fluid-filled housing (Fig. 1. 6(a)), like that of Moon in Fig. 1. 4(c). The device was fabricated on a silicon wafer, with the diaphragm formed using anisotropic ethlylene di-amine pyro-catechol (EDP) anisotropic liquid etching and a boron doped p+ silicon etch stop. Experimental results yielded a sensitivity of -206 dB re 1 V/μPa at 2 kHz, with a demonstrated bandwidth of 200 Hz to 2 kHz. Fluid-fill selection was done with viscosity, dielectric strength, leakage current, low ionic content density, toxicity, cost, and compatibility considerations. Triacetin, 2-nonanone, and silicone oil were investigated. Testing was only reported at shallow depths. White *et al.* developed a capacitive micromachined hydrophone that utilizes a viscous fluid-structure coupling (Fig. 1. 6(b)). This was done to address mass loading issues associated with submerging the sensor. A chamber is filled with 200 cSt viscosity silicone oil. A sensing membrane was located at the center

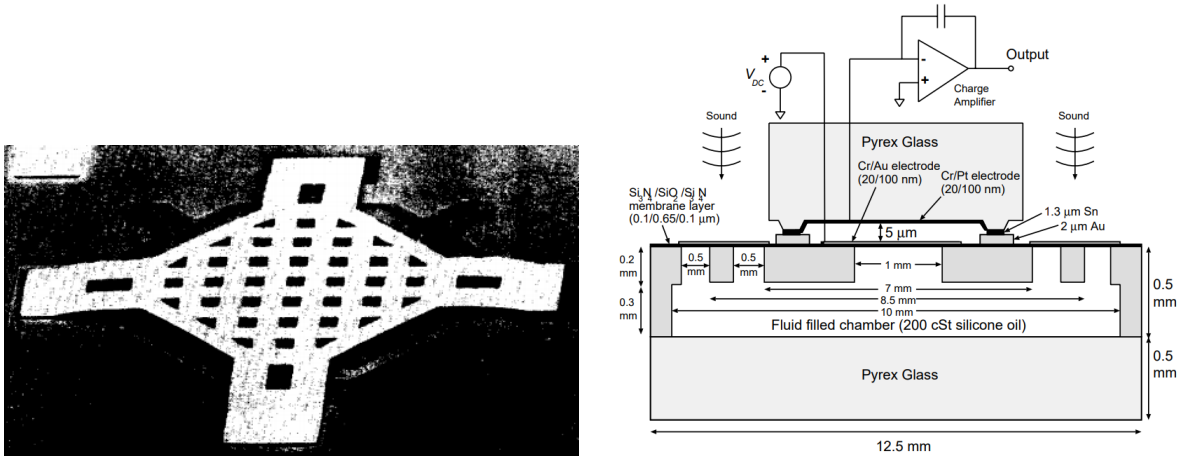

(a) (b)

Fig. 1. 6: Capacitive micromachined hydrophones. (a) Displacement "trampoline" device with perforated silicon electrode [Ber92]. (b) Micromachined hydrophone with viscous fluid-structure coupling [Whi05].

of the device, which acted as a variable gap capacitor. Input membranes located around the edges of the sensor transmit cylindrical pressure waves through the fluid chamber to the sensing membrane. Hydrostatic pressure was counteracted by stress in the input membranes, meaning that perforations in the sensing membrane were not necessary. Experimental results showed a maximum sensitivity of -180 dB re 1 V/μPa, including a 26 dB preamplifier gain. Bandwidth was demonstrated from 300 Hz to 15 kHz. The complicated architecture of this device led to setbacks in packaging; as a result, measurements were only made in air.

Capacitive micromachined ultrasonic transducers (CMUTs) are acoustic sensors that have a wide range of applications, including microphones and other airborne ultrasonic acoustic sensors [Hal94, Han04, Köy18], hydrophones and immersed TX/RX ultrasonic imagers [Bay13, Cris09, Khu11, Nik09, Son15], and even ultrasonic pumps [McL03]. CMUTs are electrostatic transducers that are fabricated by micromachining processes. They consist of arrays of thin membranes that form parallel plate capacitors with a silicon substrate, as shown in Fig. 1. 7 [Erg03]. Insulating substrates have also been reported [Kni04, Yam15]. Fabrication is normally done with either surface micromachining using a sacrificial layer or wafer bonding [Khu11]. The device in Fig. 1. 7 was made using the former.

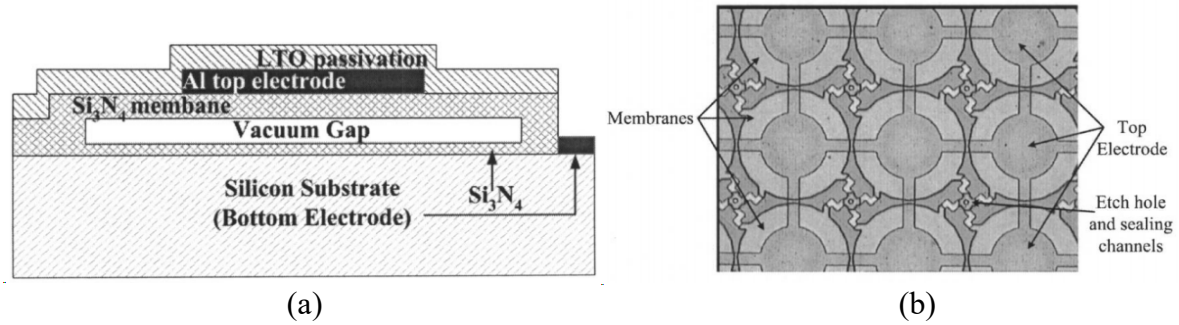

Fig. 1. 7: Capacitive micromachined ultrasonic transducers. (a) Cross section of a surface micromachined cell. Low temperature silicon dioxide (LTO) is used to electrically insulate the CMUT from the environment. (b) Multiple cells are connected to form an array. [Erg03]

CMUTs are usually sealed at vacuum to allow for high frequency immersion applications. Since these applications are at low static pressure, the interelectrode gap can be easily controlled and tuned using a bias voltage. CMUT arrays are commonly insulated from the environment using a thin layer that does not greatly affect device performance, such as low temperature silicon dioxide (LTO) They are also commonly coated in polymers such as parylene [Zhu07]. While in immersion, CMUT membranes have a lower mechanical impedance than the loading impedance over a large frequency range, resulting in ultrasonic transmission capabilities over a wide bandwidth [Khu11].

Oralkan *et al.* [Ora06] and Cristman *et al.* [Cris09] present notable work on CMUTs. Oralkan *et al.* provided experimental characterization results of CMUT operation in collapse-mode. Collapse-mode, also referred to as touch-mode, is the regime in which the insulated top and bottom electrodes make contact. This is induced by applying a high DC voltage; in deep-sea applications, this is caused by hydrostatic pressure. The device under test was a 205 × 205 μm^2 2D CMUT array consisting of 36 capacitance cells, each 30 μm in diameter. Cells were surface micromachined on a silicon substrate using CVD silicon nitride. Electromechanical frequency response was demonstrated by applying a unipolar RF pulse to the array in air and measuring real and imaginary impedance at different bias voltages. Results showed that as the membrane approached touch mode, the resonant frequency dropped from 15 MHz to 10 MHz due to a phenomenon called spring softening [Lad98]. As the membrane went into contact, the resonant frequency jumped to approximately 30 MHz, and increased to 45 MHz as voltage increased.

When a membrane goes into touch mode, the moveable region starts to make an annular shape; as it goes farther into touch mode, this region gets smaller and effectively has a larger spring constant. This leads to a higher resonant frequency and demonstrates that bandwidth can be increased by initiating touch mode operation. Cristman *et al.* characterized a 4 mm × 4 mm 2D

CMUT hydrophone array containing 256 capacitance cells. Experimental results showed that the device could perform as a tunable hydrophone, with sensitivities ranging from 1 to 76 μV/Pa depending on bias voltage. The device was tested in water at 950 kHz.

Other Types of Hydrophones

Other notable hydrophone transduction techniques include optical and piezoresistive. A major advantage of optical hydrophones is the electrically passive nature of fiber sensors and the ability to multiplex hundreds of hydrophones on a single fiber line [Kil11]. Optical transduction is done with either amplitude, polarization, or phase sensing [Bil97]. Of these, phase sensing typically provides the highest sensitivity. A common method of phase sensing is Fabry-Perot (FP) interferometry. This technique involves two parallel, flat, semi-transparent mirrors placed at a fixed distance; an assembly commonly referred to as an *etalon*. An incident monochromatic light at an arbitrary angle normal to the mirror surface will undergo multiple reflections within the etalon. The intensity distribution of the reflected and transmitted interfering beams creates concentric rings, whose angular diameters depend on the etalon spacing and the frequency of the incident light [Her86]. Optical hydrophones tend to offer low temperature coefficients, high sensitivity, and excellent bandwidth. However, optical signal processing signals are not readily available and inconvenient for integration into data logging microsystems.

Kilic *et al.* [Kil11] presented an optical hydrophone based on FP interferometry (Fig. 1. 8). The device utilizes four single mode fibers (SMFs). Three of the fibers lead to photo crystal (PC) diaphragms micromachined on a silicon chip. The fourth fiber is used for reference. Each fiber tip is coated with a stationary mirror, which creates an etalon with the diaphragms. Three different diameter diaphragms are utilized (150, 212, and 300 μm) to increase dynamic range. To protect from debris and corrosion, the device is encased in a fluid filled bladder containing clean

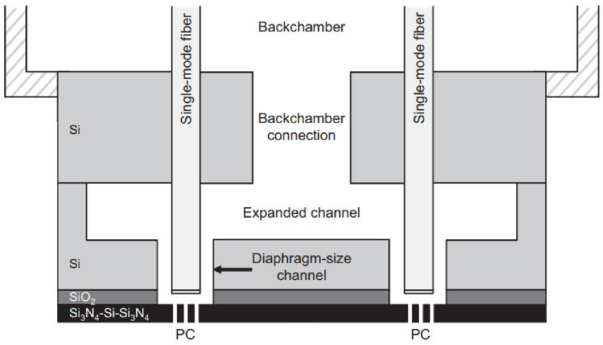

Fig. 1. 8: Cross section of a miniaturized photonic crystal hydrophone. Mirror-tipped single mode fibers create an FP interferometer. The sensor is encased in clean fluid, which can displace through a channel into the backchamber. [Kil11]

water. The PC diaphragms are perforated. Encased water flows through a channel into the device backchamber, which facilitates diaphragm deflection. Experimental results in distilled water show a measurable response from at least 1 Hz to 100 kHz, though the response is flat only to approximately 10 kHz. Lastly, a minimum detectable pressure as low as 12 μPa/√Hz (20 kHz) was measured. This extremely low value highlights the benefit of electrical passivity afforded by optical hydrophones.

Piezoresistive transduction is most commonly applied to pressure sensing and other static sensing applications, because the technique is inherently static. Its largest advantage over piezoelectric transduction is response at low frequency. Piezoresistive materials respond to applied mechanical stress with a change in resistance. Piezoresistive materials are often deposited at the edges of diaphragms in a Wheatstone configuration, and read out using the same [Gia06]. Semiconductor materials are commonly used as piezoresistors because in addition to geometrical changes from applied stress, the charge carrier mobility of the material also changes. This results in extremely high gage factors compared to other materials. Unfortunately, piezoresistive materials are not favored in harsh environmental sensing applications due to relatively high temperature coefficients.

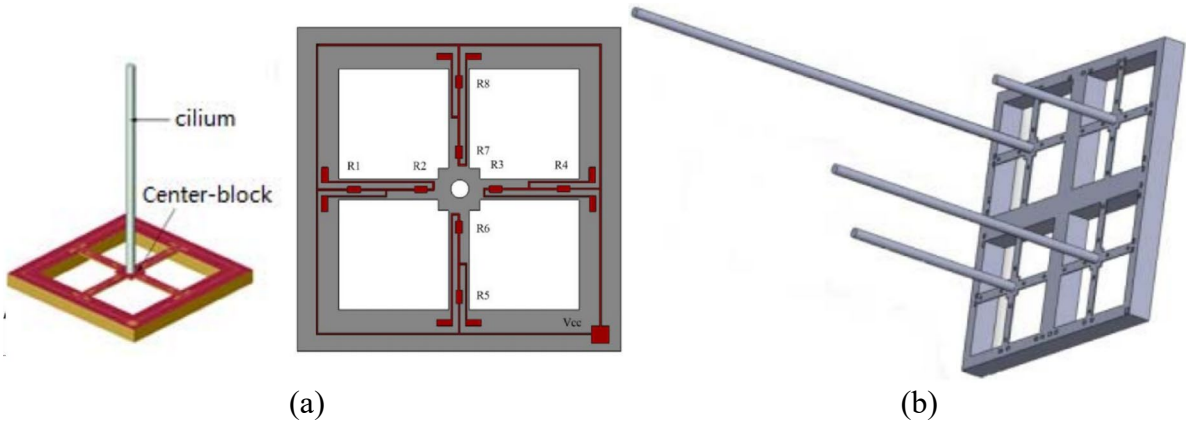

(a) (b)

Fig. 1. 9: Biomimetic piezoresistive vector hydrophone array. (a) A single array element. (b) Arrayed elements of different length provide higher bandwidth. [Men16]

Considerable work has been reported on piezoresistive vector hydrophones inspired by fish lateral line organs [Men16, Gua12, Wan17]. Similar designs have also been reported using piezoelectric transduction [Gan18]. Mengran *et al.* [Men16] presented an array of biomimetic cilia structures to increase sensitivity at higher frequencies. Each structure consists of a single beam with a pair of Wheatstone bridges about its base (Fig. 1. 9(a)). Acoustic pressure displaces the beam, inducing a measurable resistance change. This design has a sensitivity tradeoff with bandwidth: increasing beam length increases the sensitivity, but also decreases bandwidth. To have high sensitivity and high bandwidth, an array of differently sized beams is presented (Fig. 1. 9(b)). Experimental results yielded an amplified maximum sensitivity of -179 dB re 1 V/μPa and a bandwidth ranging from 20 Hz to 5 kHz.

Hydrophone Performance

Hydrophone performance is measured in sensitivity (standard units of dB re V/μPa), MDP, size, bandwidth, and static pressure rating. Table 1.1 benchmarks several different hydrophones published in academic journals and conferences. Four different types of transduction are included. The highest static pressure rating of any hydrophone is 4.0 MPa [Sul78], which employs a flexural disk piezo ceramic design. There is no pressure balancing in this macro scale design. The air-

Table 1. 1: Comparison of hydrophones published in academia.

		Sensitivity	Footprint [mm^2]	MDP	*BW (demonstrated)	Static Pressure (demonstrated)
Moo10a	P.E.	-227.5 dB	49	?	100 Hz to 1 kHz	1.5 MPa
Sul78		-200 dB	N/A (macro)		1 Hz to 1 kHz	4.0 MPa
Cris09	Cap.	-202 dB	16	2.5 Pa 1.86 MHz	? to 3.4 MHz	0.1 MPa
Whi05		-180 dB (in air)	156	7.0 Pa 1 kHz	300 Hz to 15 kHz	
Ber92		-206 dB	?	?	200 Hz to 2 kHz	
Kil11	Opt.		28.3	3 mPa 1 kHz	400 Hz to 100 kHz	0.1 MPa, pressure balanced
Gua12	P.R.	-180 dB	0.46	0.98 Pa 1 kHz	20 Hz to 2 kHz	0.1 MPa

* +/- 3dB bandwidth where applicable

filled back chamber design presented in Fig. 1. 4 [Moo10a] accomplishes a miniature form factor with a non-insignificant static pressure capability of 1.5 MPa. The capacitive hydrophones were not demonstrated to operate beyond 1 atm, although the fluid-filled architectures of Bernstein [Ber92] and White *et al.* [Whi05] could accommodate some increase in static pressure. The CMUT hydrophone [Cris09] demonstrates bandwidth capabilities provided by hermetically sealed capacitive sensing elements. The optical hydrophone [Kil11] is notable for an extremely low MDP at 1 kHz, which is from the electrically passive nature of optical transduction. The pressure-balanced design was not characterized at elevated static pressure but can certainly accommodate an increase in pressure. Lastly, Guan *et al*. [Gua12] present a cantilevered piezoresistive sensor with an extremely small footprint.

Table 1. 2 benchmarks hydrophones from industry. All hydrophones listed are presumably piezoelectric. The highest static pressure rating is of the High Tech, Inc. HTI-94-SSQ hydrophone, which is capable of operation at 61 MPa static pressure. The MDP is surprisingly low, able to

Table 1. 2: Comparison of hydrophones developed by industry.

	Sensitivity	BW	*Static Pressure	MDP	Size
Benthowave BII-7002	-205 dB	1 Hz to 200 kHz	20 MPa	?	?
Aquarian Scientific AS-1	-208 dB	1 Hz to 100 kHz	0.2 MPa	?	4,523 mm^3
Cetacean Research Technology CR3	-207 dB	60 Hz to 180 kHz	9.8 MPa	31.6 mPa @1 kHz	12,723 mm^3
Ocean Sonics iListen HF	-169 dB	10 Hz to 100 kHz	60 MPa	31.6 mPa @1 kHz	483,152 mm^3
High Tech, Inc. HTI-94-SSQ	-198 dB	2 Hz to 30 kHz	61 MPa	5.6 mPa @1 kHz	30, 561 mm^3
Bruel & Kjaer Type 8106	-173 dB	7 Hz to 80 kHz	10 MPa	1 Pa @1 kHz	146, 373mm^3

*Gage pressure

resolve 5.6 mPa at 1 kHz. The Ocean Sonics iListen HF is a smart hydrophone with integrated signal conditioning and analog to digital converter. This hydrophone provides excellent performance, with an MDP of 31.6 mPa at 1 kHz, static pressure up to 60 MPa, and sensitivity of -198 dB. However, the hydrophone is large. The commercial hydrophones in this table show clear capability at elevated static pressure, but at the cost of size.

1.3 Focus of This Work

The focus of this work was to develop a micro hydrophone that is compatible with existing microsystems for collection of seismic acoustic data, fully characterize the sensor, demonstrate its use in the existing microsystem for seismic data collection, and to investigate application to other areas of interest. These applications of interest included use as a deep-sea hydrophone and ultrasonic transducer.

1.4 Organization of Thesis

The design of a new kind of hydrophone sensor is detailed, along with experimental characterization and demonstration of several applications of interest. Chapter 2 presents a description and characterization of the sensor itself. The chapter begins with a description of the heterogeneous architecture and its design concept. The sensor is fabricated on an insulating sapphire substrate, utilizes 106 sensing elements, and is diced into $1.4 \times 1.6 \times 0.5$ mm^3 chips. Finite element analysis and lumped element modeling is performed. Static pressure response is experimentally verified up to 50 MPa static pressure. Sensor repeatability and usage over time is also demonstrated. The maximum static capacitance change over the 50 MPa range was 34.406 pF. Responsivity was measured up to 3.0 pF/MPa. Electromechanical resonance testing was performed in air and paraffin oil. The first diaphragm resonances are demonstrated to occur in air and oil at 4.105 MHz and 2.319 MHz, respectively. These values match extremely well to the lumped element model.

Chapter 3 details application of the hydrophone to an autonomous microsystem for oil and gas exploration. The millimeter scale (8 mm on a side) microsystems utilize off the shelf electronic components integrated on a flexible printed circuit board and encapsulated in polymer. The hydrophone is integrated with an unpackaged microsystem, which was programmed to measure seismic acoustic signals up to 100 Hz frequency. The seismic signals reached as high as 100 psi (689 kPa) in magnitude. The frequency response is characterized and shown to be completely flat over the 100 Hz band, as expected. The incremental response vs. static pressure was characterized, along with static response with pressure, static pressure resolution, and MDP at varying static pressure. For signal frequencies above 2 Hz, the MDP was demonstrated to be

below 0.1 psi (689 Pa) over almost the entire static pressure range. Lastly, seismic data collection was demonstrated for signals up to 100 Hz.

Chapter 4 explores application as an ultrasonic transducer and a deep-sea hydrophone. The hydrophone is experimentally calibrated in paraffin oil at atmospheric pressure up to 100 kHz (-221 +/-1.9 dB re V/μPa, 10V bias). The response is completely flat, as expected. The sensitivity vs. applied static pressure at 1 kHz is characterized up to 50 MPa applied static pressure. This information is representative of the flat band response, which increases when static pressure is applied. Next, hydrophone response up to 2 MHz frequency was demonstrated using a pulse-echo technique at atmospheric pressure. Noise and MDP were characterized at atmospheric pressure and were found to be 0.92 $\mu V/\sqrt{Hz}$ and 24.5 $mPa/\sqrt{Hz}$ (40V bias) at 1 kHz, respectively.

Chapter 5 summarizes the thesis, lists research contributions, and proposes future work. The future work consists of two efforts: 1) design and construction of a high-pressure acoustic test setup with MHz band capability, and 2) application of the hydrophones to high resolution SONAR at extended ocean depth. The proposed test setup involves a pressure vessel that is submerged in oil. The vessel has one side wall that is composed of a rigid plastic. This plastic wall is designed to be acoustically transparent when submerged in oil, which drastically increases which acoustic transmitters are compatible with the setup. Additionally, since the transmitter is not in contact with the setup, the mechanical considerations of transmitter operation are greatly reduced. For use in deep-sea, high resolution SONAR, the chip architecture can provide an unparalleled combination of form factor, bandwidth, and ocean depth operation. A preliminary design is discussed, as well as possible challenges and process improvements for this application.

Chapter 2: Heterogeneous Hydrophones

This chapter describes the heterogeneous hydrophone design concept and architecture, employed using surface micromachined, variable gap capacitive sensors deposited on an insulating sapphire substrate. Capacitive sensors are usually unfavorable for use as deep-sea hydrophones due to complications from the interelectrode gap. The interelectrode gap is vulnerable to debris and normally requires pressure balancing. Hydrophones of all transduction types typically use a housing that encases sensors or sensing elements inside a neutral medium to avoid some of these issues [Whi05, Ber92, Kil11, Moo10a, Moo10b]. These schemes can be effective, but they are incompatible with autonomous microsystems due to size. To bypass the issue, this work investigates a micro hydrophone with surface micromachined, hermetically vacuum-sealed capacitive sensing elements arrayed in a heterogeneous architecture. Vacuum-sealed structures provide unparalleled protection to interelectrode gaps, vastly simplified packaging, vastly reduced thermal mechanical noise compared to existing acoustic capacitive sensors, as well as static pressure sensing capability. Furthermore, heterogeneous configuration allows for a small chip size, improved linearity, and bandwidth exceeding 1 MHz.

2.1 Heterogeneous Concept and Architecture

Hermetic sealing of variable gap capacitive sensors like the one shown in Fig. 2. 1 has benefits and compromises. For example, vacuum sealing is immune to reduced diaphragm compliance from compressed gas as well as energy dissipation due to viscous flow through

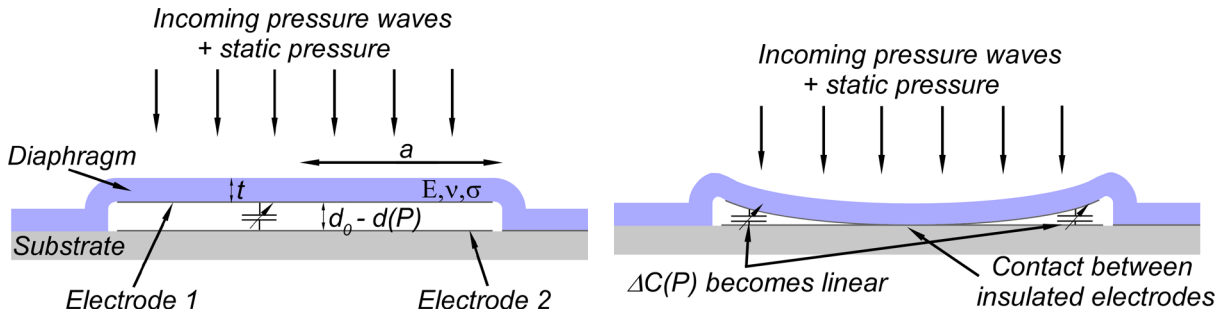

(a) (b)

Fig. 2. 1: Diagram of a hermetically sealed variable gap capacitive sensing element. (a) Undeflected case. Pressure is not able to equalize over the diaphragm, meaning the sensor is responsive to static changes in pressure. (b) As static pressure increases, electrodes eventually make contact and response becomes linear; this region of operation is referred to as touch mode.

perforations. However, a sealed diaphragm is sensitive to changes in static pressure, which can have drastic impact on hydrophone performance: the device incremental response is defined by the static bias pressure applied to the diaphragm. In the case of an acoustic sensor, this warrants large signal and small signal considerations. Nominal static diaphragm deflection with respect to bias

pressure is described by the following equation modified from [Tim59]:

$$d_{nom}(P) = \frac{a^4(5+\upsilon)}{3Et^4(1+\upsilon)} P \left[\frac{16}{3(1-\upsilon^2)t} + \frac{4a^2\sigma}{(1-\upsilon)Et^3}\right]^{-1}, \tag{2.2}$$

where a is diaphragm radius, E is Young's Modulus, t is diaphragm thickness, v is Poisson's ratio, and σ is residual stress in the diaphragm. The static (bias) pressure, P, is interchangeable with acoustic pressure magnitude, p. The capacitance response to pressure is therefore

$$C(P) = \frac{\varepsilon_r \varepsilon_0 A}{d_0 - d_{nom}(P)}, \tag{2.3}$$

where A is diaphragm area and d_0 is the undeflected interelectrode gap. The nominal sensitivity of a sensing element such as the one shown in Fig. 2. 1 is therefore

$$S'_{nom} = \frac{\partial C(P)}{\partial P} = \frac{\varepsilon A}{\left(d_0 - d_{nom}(P)\right)^2} \frac{a^4(5+\upsilon)}{3Et^4(1+\upsilon)} \left[\frac{16}{3(1-\upsilon^2)t} + \frac{4a^2\sigma}{(1-\upsilon)Et^3}\right]^{-1}. \tag{2.4}$$

It is desirable to measure static pressure changes for downhole autonomous microsystem applications, though it does introduce a unique design challenge. From equation 2.4, the incremental response rises dramatically as the deflection approaches d_0. This highlights a massive non-linearity with respect to interelectrode gap. When the diaphragm contacts the bottom electrode, the sensor enters a regime called touch mode in which the response is linear. This is depicted in Fig. 2. 1(b). Of course, the electrodes must be insulated. As pressure increases, the diaphragm will eventually go completely into touch mode after which there will be no response to pressure. The regime immediately before touch mode is referred to as transition mode, which has a characteristic peak in incremental response over a small range of applied pressure. Fig. 2. 2(a) shows simulation results of a single sensing element with the same structure as that of Fig. 2. 1. The FEA simulation was performed using COMSOL Multiphysics® with a silicon nitride diaphragm of ϕ96 μm, 5 μm thickness, and 1 μm interelectrode gap. Fig. 2. 2(b) shows a simple derivative of capacitance with respect to pressure (incremental response), plotted with respect to pressure. Transition mode is marked by the massive spike in incremental response, in this case occurring at approximately 2.5 MPa.

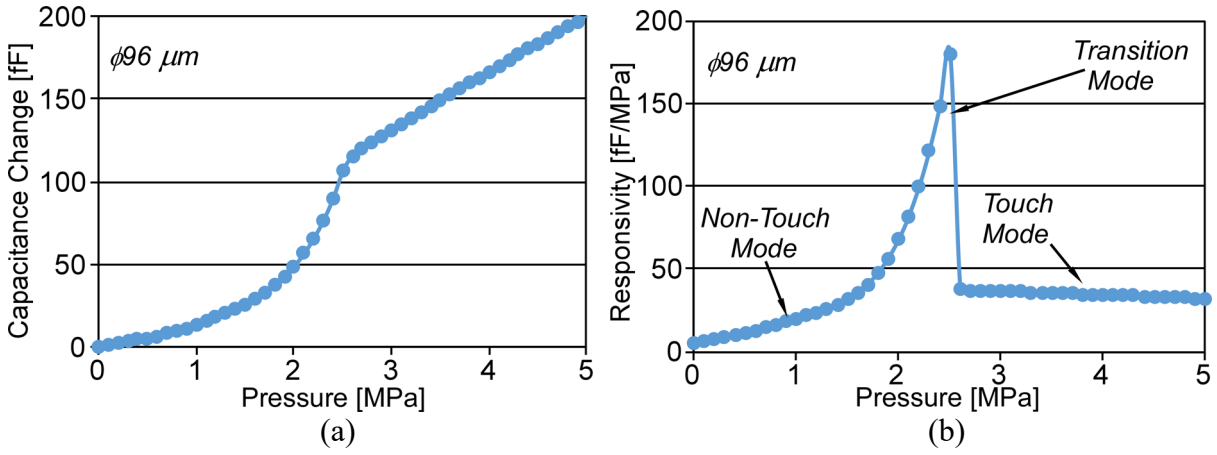

Fig. 2. 2: COMSOL simulation of a diaphragm of ϕ96 μm, 5 μm thickness, with an interelectrode gap of 1 μm. (a) Capacitance response to pressure. (b) Incremental response at different pressure biases. A large spike in incremental response is seen in transition mode.

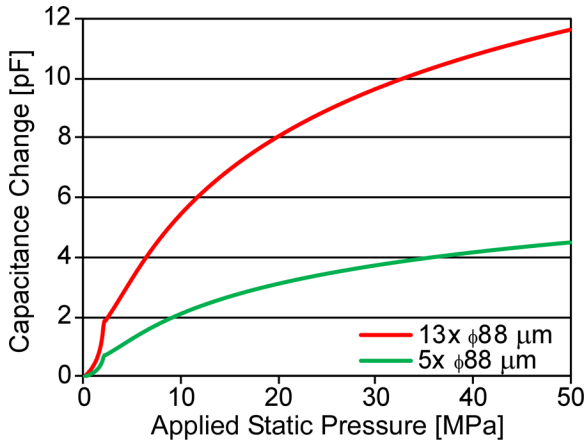

Fig. 2. 3: Simulation of two different homogeneous arrays, each containing only ϕ88 µm sensing elements. A 450 nm interelectrode gap and 4.5 µm thick diaphragms were used. The larger curve is the exact same shape as the smaller curve. Both curves show large response at low pressures and diminishing response as diaphragms enter deeper into touch mode.

Multiple sensing elements can be electrically connected in parallel to make an array. A homogeneous array, i.e. an array with diaphragms of all the same diameter, would have a response *N* times larger than that pictured in Fig. 2. 2(a,b), with *N* being the number of capacitive sensing elements connected in parallel. Two simulated homogeneous arrays are shown in Fig. 2. 3. Both arrays utilize only ϕ88 µm sensing elements, hence they are homogeneous. The silicon nitride diaphragms are simulated to be 4.5 µm thick and interelectrode gaps are 450 nm. The larger curve (red) is an array that utilizes thirteen sensing elements electrically connected in parallel, while the smaller curve (green) represents an array of 5 sensing elements. The increased number of sensing elements in the red curve results in more response at higher pressures, but it also accentuates a massive non-linearity at low pressure. Additionally, as a large diaphragm completely enters touch mode, the baseline capacitance can become large and inconvenient. A homogeneous array may provide sufficient signal to perform as a hydrophone but is not preferred due to lack of linearity, inefficient generation of incremental response at elevated pressure, and unruly baseline capacitance that limits readout options. To increase static

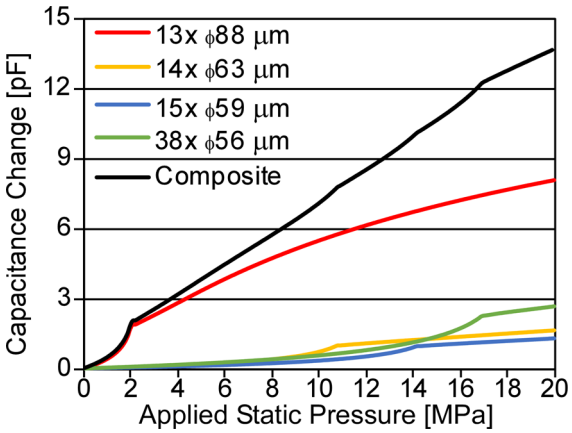

Fig. 2. 4: Simulation of a heterogeneous array with four separate diaphragm sizes. A 450 nm interelectrode gap and 4.5 µm thick diaphragms were used. Smaller sensing elements do not have a notable response until reaching transition mode; this results in an extension of static pressure range with negligible impact on low pressure response.

pressure range, incremental response at high pressure, bandwidth, as well as linearity, a heterogeneous architecture is utilized.

As its name implies, a heterogeneous array consists of sensing elements with a range of different diaphragm diameters. An example of such an array is shown in Fig. 2. 4. Here, four differently sized sensing elements are connected in parallel, with the response from each discretely sized sensing element as well as the composite response. The same 13x ϕ88 µm array from Fig. 2. 3 is included in the plot, once again in red. By adding a large number of smaller sensing elements, the incremental response at high pressure can be increased without changing the low-pressure response. This is because the responses of the smaller elements are negligible until they reach transition mode. The applied static pressure (bias pressure) in which a given sensing element enters transition mode changes by a factor of $d_0 t^3 a^{-4}$. Since the interelectrode gap and diaphragm thickness cannot be varied from element to element, diaphragm diameter is the design variable of choice. Smaller sensing elements also provide higher bandwidth, which changes with $a^{-4}t$. The incremental response of a single element before touch mode changes by a

factor of $a^6 d_0^{-2} t^{-3}$; for this reason, smaller diaphragms are required to be in higher numbers to maintain good linearity.

Familiar work by Chavan and Wise [Cha02] presents a capacitive pressure sensor that utilizes five separate diaphragms over a 300 Torr dynamic range. Each diaphragm composes a variable gap capacitive element. Diaphragm diameters range from 1000 μm to 1100 μm. One of the diaphragms, the "global" diaphragm, operates over the entire dynamic range with low resolution, and is used to determine the approximate pressure. On-board circuitry selects one of the remaining diaphragms based on highest incremental response at the given pressure, whose signal provides higher pressure resolution. Bossed diaphragms provide a slight increase in linearity. A silicon substrate creates parasitic capacitance that discourages parallel connection of diaphragms.

The insulating sapphire substrate is critical to this work because it reduces parasitic capacitances by up to two orders of magnitude when compared to conductive substrates. Conducting metal layers used for electrode connections must be insulated, which forms a capacitive gap with the substrate that at times can be under 100 nm in thickness; with a conducting substrate this creates a significant addition to baseline capacitance of the sensor, which degrades sensitivity by a factor of $(C_0+C_p)^{-1}$ where C_0+C_p is the baseline capacitance. Capacitive sensors have been reported that have parasitic capacitance composing 90% of the total baseline capacitance. Each capacitive sensing element in an array introduces its own parasitic capacitance, which would reduce the performance of this work if fabricated on a conducting substrate.

This work presents a heterogeneous hydrophone array designed for miniature size, high bandwidth, improved linearity, and high incremental response over a wide range of static

pressure. A surface micromachining process is used to fabricate the devices on an insulating sapphire substrate, which results in lowered parasitic capacitance. The device is mechanically robust and can be applied in situations that involve extremely high hydrostatic pressures and/or large pressure waves. Hermetically vacuum-sealed diaphragms eliminate thin film damping, increase reliability by eliminating inter-electrode debris, facilitate touch mode operation that virtually eliminates pressure overloading concerns, and enables simplified packaging and small form factor for microsystem compatibility.

2.2 H106 Heterogeneous Hydrophone

A 3D representation of the H106 heterogeneous hydrophone is shown in Fig. 2. 5. The H106 design contains 106 sensing elements ranging from ϕ104 μm to ϕ56 μm and is designed for operation from atmospheric pressure to 50 MPa static pressure. The capacitive sensing elements are deposited on a sapphire substrate. Wire leads are made with sputtered aluminum, and lead to two connection terminals. Specifications are tabulated in Table 2. 1.

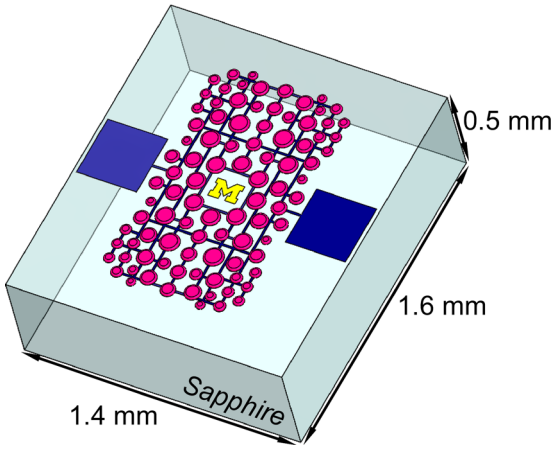

Fig. 2. 5: 3D representation of the H106 heterogeneous hydrophone. 106 capacitive sensing elements are electrically connected in parallel, with two sensor connection terminals.

Table 2. 1: H106 physical specifications

Diaphragm Thickness	4.5 μm
Interelectrode Gap	450 nm
N Diaphragms	106
Static Pressure Range	1 atm to 50 MPa
Total Chip Area	1.585 mm × 1.380 mm = 2.187 mm^2
Chip Thickness	0.5 mm
Diaphragm Area	0.37 mm^2
Active Area	0.90 mm^2
Largest Diaphragm	ϕ104 μm
Smallest Diaphragm	ϕ56 μm

The H106 heterogeneous hydrophone is fabricated [Ben19] through a five-mask process flow[1] shown in Fig. 2. 6. The first mask is used for sputtering and liftoff of the Ti/Al/Ti (15/370/15 nm) bottom electrode. A 100 nm thick layer of silicon nitride is then deposited by plasma enhanced chemical vapor deposition (PECVD) as an insulation layer over the bottom electrode (mask 2). Next, 450 nm thick sacrificial layer of amorphous silicon (α-Si) is deposited by PECVD and patterned using reactive ion etching (RIE) (mask 3). This layer defines the capacitive gap. The fourth mask is used for sputter and liftoff of the Ti/Al/Ti upper electrode (15/170/15 nm). Evaporation is avoided in this step to provide good step coverage. A thin layer of silicon oxide/nitride/oxide (ONO) (200/1900/200 nm) is then deposited by PECVD and patterned with RIE (mask 5). Etchant access holes and contact pad openings are formed during this step. The nitride is sandwiched between the two oxide layers for protection during etching of the sacrificial layer. Etchant access holes of 5 μm × 0.8 μm allow XeF_2 gas to enter the cavity and etch the sacrificial layer. Gas phase XeF_2 is used due to its selectivity, isotropy, and ability to

[1] Fabrication performed by Dr. Alexander Benken.

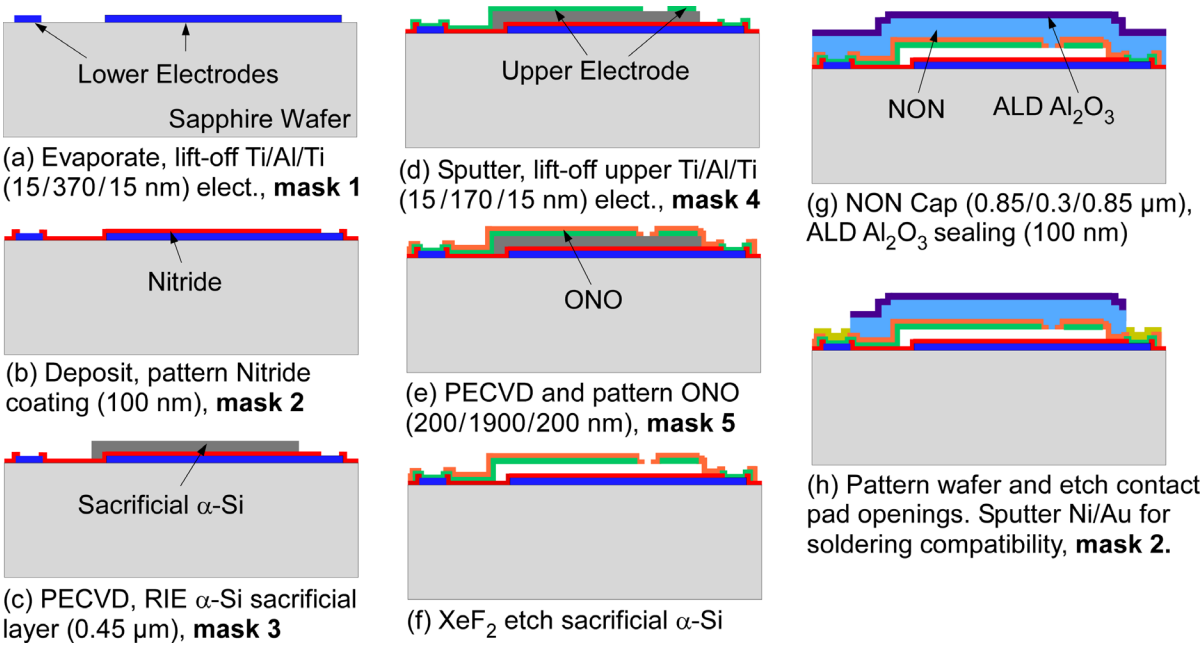

Fig. 2. 6: Fabrication process flow

etch without causing stiction. The dimensions of the holes were chosen to allow for sealing of the ONO layer once etching is complete, while still providing adequate etching ability. Once etching of the sacrificial layer is completed, the the ONO layer is then capped by a 2.0 µm layer of PECVD NON (850/300/850 nm). Finally, a 100 nm layer of Al_2O_3 is deposited by ALD for added hermiticity [An13] and chemical resistance. Optical images can be found in Fig. 2. 7 and Fig. 2. 8.

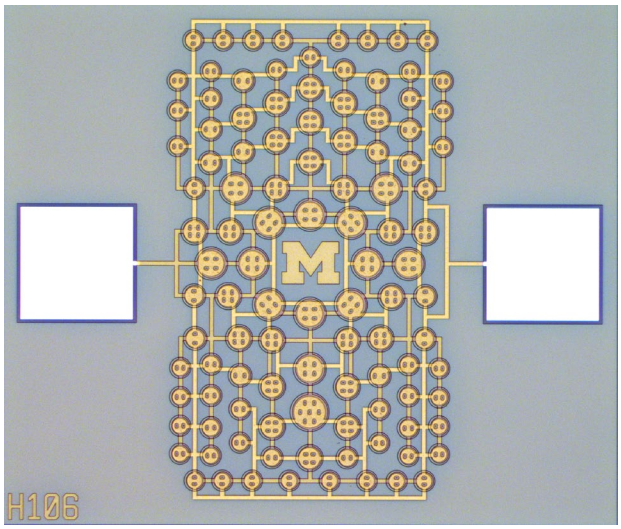

Fig. 2. 7: Optical images of the H106 heterogeneous hydrophone. (a) Closeup image. (b) Macroscale image.

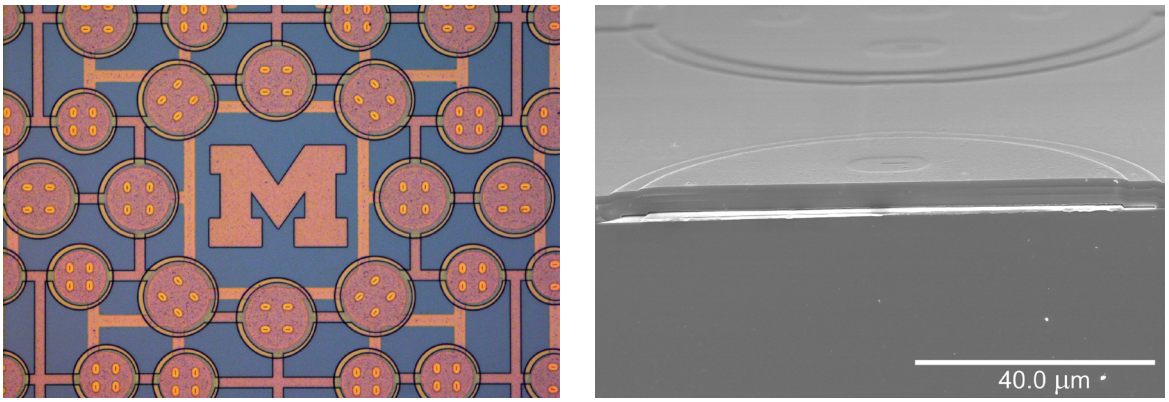

(a) (b)

Fig. 2. 8: Optical and SEM images of the H106 heterogeneous hydrophone. (a) Closeup optical of the wire leads. Both the top and bottom electrodes are connected using sputtered Ti/Al/Ti. (b) SEM image of a diaphragm cross section.

2.3 Modeling and Simulation

2.3.1 FEA Modeling of the Capacitance Response

Computer simulations were completed using COMSOL Multiphysics ® 5.1. The *MEMS Electromechanics* module to study the device's capacitance response to change in external static pressure. The technique used is presented by Luo and Gianchandani [Luo15, Luo16]. Touch mode of the two electrodes was simulated by applying a distributed force to the top electrode once it contacts the insulating layer over the bottom electrode. Please see Fig. 2. 9 for reference. The permittivity of the insulating nitride layer is higher than vacuum and was simulated accordingly. Additionally, the RMS surface roughness, R_q, of the insulating layer was simulated

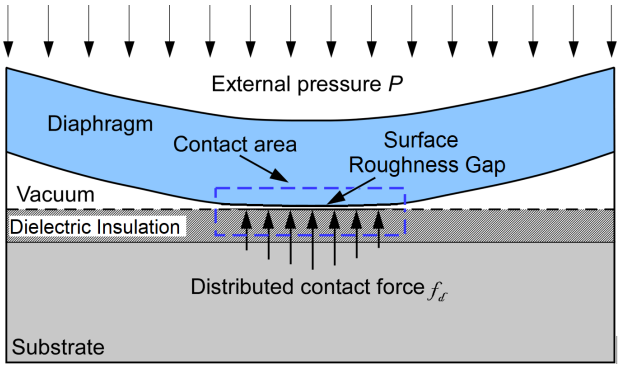

Fig. 2. 9: Cross sectional image illustrating the FEA technique used to simulate the sensing elements when in touch mode. The diaphragm is kept from intersecting the bottom electrode through use of a distributed force. The insulating dielectric layer plays a major role in touch mode sensitivity, as does the surface roughness of that layer [Luo15].

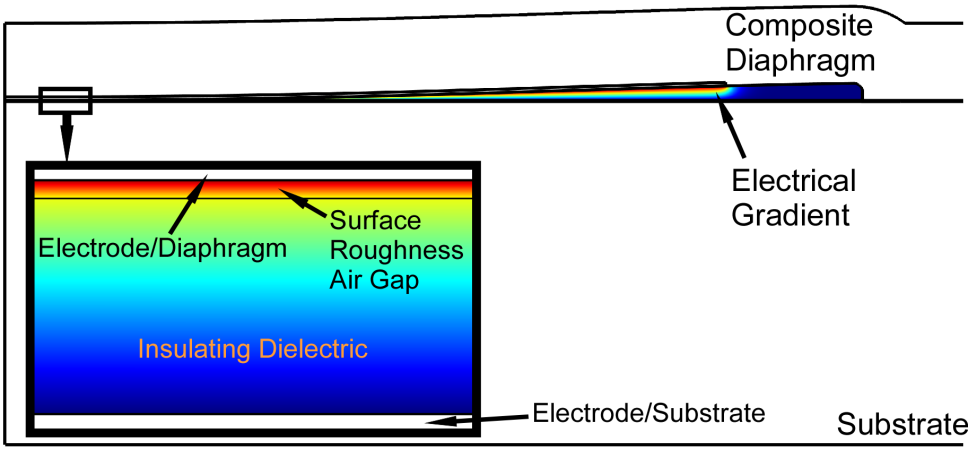

Fig. 2. 10: Depiction of the 2D axisymmetric FEA geometry used for this work. Surface roughness of the insulating layer is simulated with a thin air gap.

as a small gap between the diaphragm and insulating dielectric. The 2D axisymmetric FEA geometry is shown in Fig. 2. 10.

Due to the large number of simulation non-idealities, it is not practical to simulate an exact static pressure response without matching simulation parameters to experimental results. This is because small changes in some non-idealities, namely the Young's Modulus, RMS surface roughness, and nitride layer thickness have major effects on the sensor response. The simulation parameters are listed in Table 2. 2, along with estimated variation ranges.

The simulated capacitance response to applied static pressure is shown in Fig. 2. 11. The composite response of all sensing elements in parallel is shown in (a). The slope of the curve,

Table 2. 2: Simulation parameters for static pressure response

Parameter	Nominal Value	Est. Variation
Interelectrode Gap, d_0	450 nm	+/-1%
Diaphragm Thickness, t	4.50 µm	+/-1%
Young's Modulus, E	80 GPa	+/-5%
Diaphragm Stress	35 MPa	+/-20%
Insulation Layer Thickness	100 nm	+/-20%
Surface Roughness	20 nm	+/- 50%

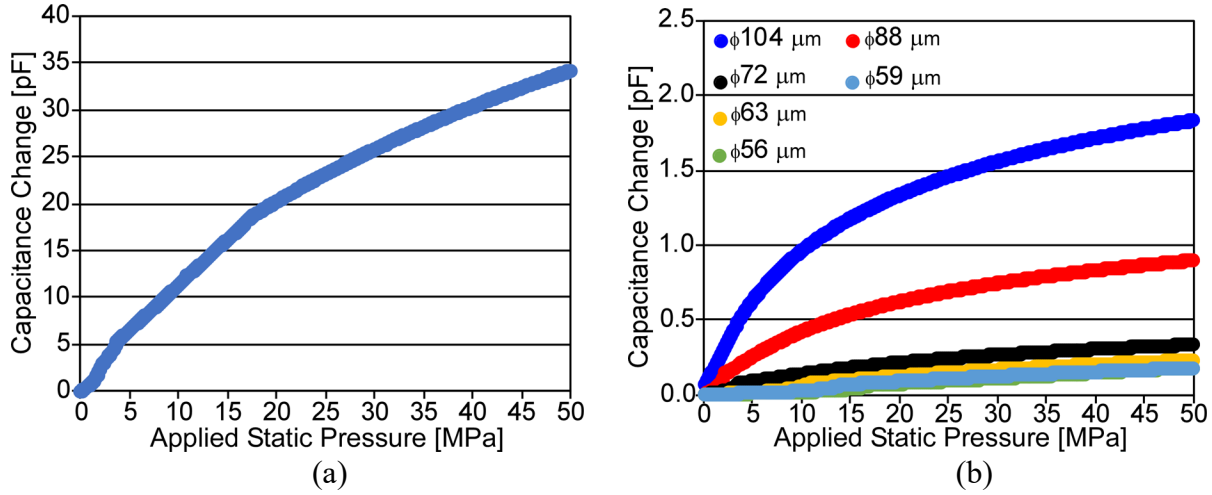

Fig. 2. 11: Simulated capacitance response to static pressure. (a) Composite response. (b) Individual response from each discrete size of diaphragm.

also known as the incremental response, R, increases when any sensing elements enter transition mode. The incremental response is defined as

$$R(P) = \frac{\partial \Delta C(P)}{\partial P}, \tag{2.5}$$

where P is applied static pressure and ΔC is the capacitance response. The incremental response is approximated in Fig. 2. 12. The largest diaphragm (ϕ104 μm) enters transition mode at approximately 70 kPa applied static pressure (171 kPa absolute pressure). There is only one of such diaphragms and is not easily seen in Fig. 2. 12. The next largest diaphragm enters transition

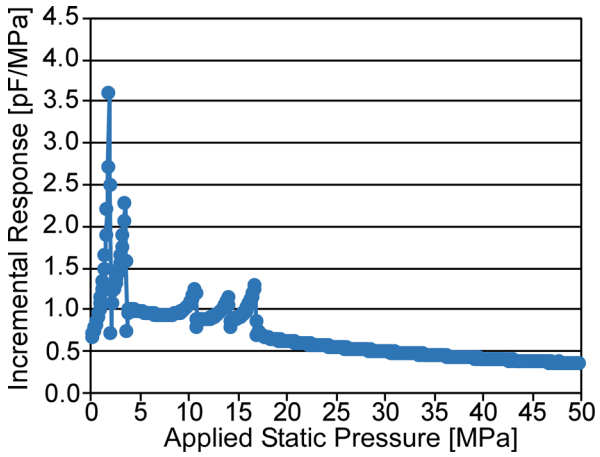

Fig. 2. 12: Extrapolated incremental response from simulated composite response to static pressure.

mode at approximately 1.8 MPa applied static pressure. This creates a major peak in incremental response that is clearly visible in Fig. 2. 12. There are four more peaks in the incremental response plot, each corresponding to differently sized sensing element diaphragms. The discrete static pressure responses from single diaphragms of each diameter are shown in Fig. 2. 11(b).

2.3.2 Diaphragm Stress

Residual and induced diaphragm stresses can play an important role in diaphragm stiffness. The extent of this role is dependent on the diaphragm's behavior as either a plate or a membrane [Far92]. A diaphragm is described as a plate if the dominant restoring force is due to bending of the diaphragm itself. On the other hand, the diaphragm is considered a membrane if the dominant restoring force is due to residual stresses in the thin film. The nominal displacement per unit applied pressure in equation 2.2 is useful for predicting how a diaphragm will behave. For both situations, changes in stress can change the diaphragm stiffness. This is thoroughly described by Gianchandani et al. [Gia06]. In this work, the diaphragm dimensions result in behavior as a plate. That said, the immense static pressures do induce stresses in the diaphragms that could alter performance.

Simulations were performed to quantify how stresses in the diaphragm change with applied static pressure. The volume-averaged radial stress has the largest impact on diaphragm spring constant, and scales with a^2t^{-2}. Only the largest sensing element was simulated to show the worst-case scenario. Simulation results are shown in Fig. 2. 13. The average values of normal stresses in the radial, phi (angular), and z (vertical) axes are plotted on the primary axis while the maximum Von Mises stress is plotted on the secondary axis. As pressure is increased, the average stress in the phi direction becomes compressive to accommodate deflection. The

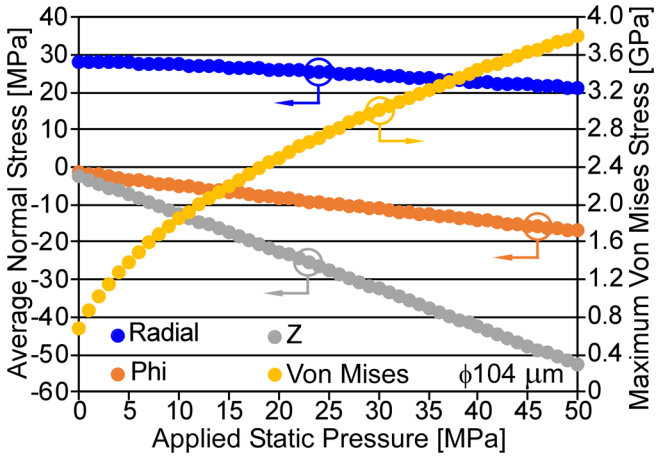

Fig. 2. 13: Simulated diaphragm stresses. Average normal stresses are shown on the primary axis while maximum Von Mises stress is shown on the secondary axis. The radial stress can affect sensor performance, however its change over 50 MPa static pressure has a negligible effect on performance since the diaphragm behaves as a plate. The Von Mises stress reaches a maximum value of 3.81 GPa.

average z stress changes linearly with the applied static pressure, entering deep into compression. This is expected due to the compressive nature of the applied static pressure. The average radial stress decreases as parts of the diaphragm enter compression. This change is small, however, and has a negligible effect on the spring constant. When the diaphragms are in touch mode, however, the spring constant is effectively higher due to decreased motion. This is unrelated to stress. The maximum Von Mises stress increases to a relatively large value of 3.81 GPa at 50 MPa static pressure. This number is much larger than the yield stress of the PECVD silicon nitride composite diaphragm. However, the stress occurs at a miniscule region at the edge of the diaphragm; yielding is only expected to occur in very small regions of the largest diaphragms.

The radial and Von Mises stress profiles are shown in Fig. 2. 14 and Fig. 2. 15, respectively. The applied static pressure is 50 MPa. The radial profile shows a mostly uniform stress profile throughout the diaphragm. The diaphragm edge shows both compressive and tensile stresses. The Von Mises stress profile shows mostly uniform stress ass well, with stress

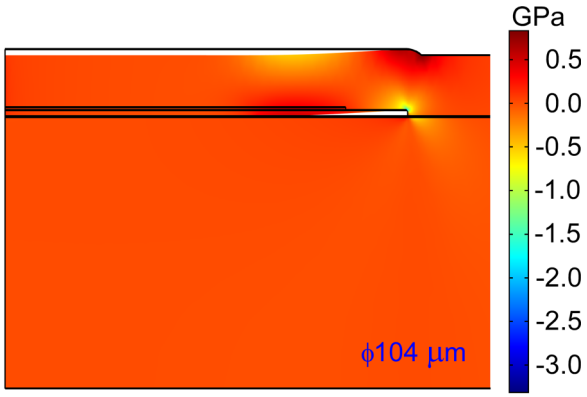

Fig. 2. 14: Radial stress profile of a ϕ104 µm diaphragm at 50 MPa applied static pressure. As expected, the maximum stresses occur around the circumference of the diaphragm.

concentrations occurring at the edges. The maximum stress occurs at a concentration that is extremely small and hardly visible in the scale of Fig. 2. 14. Beyond the maximum stress, there is elevated stress around 1.5 GPa in the same vicinity. There is likely some yielding that occurs here. In practice, the diaphragms appear to have some "breaking in" that completes after several pressure cycles up to 50 MPa.

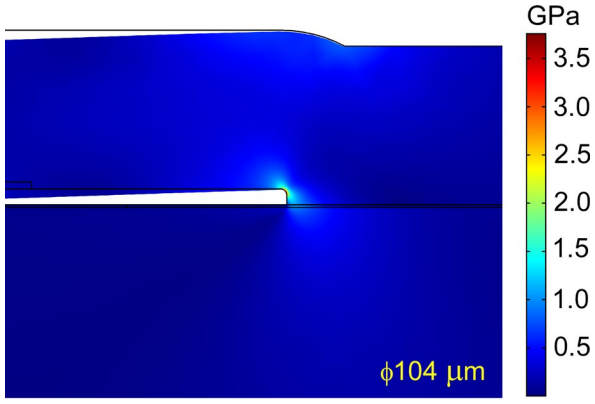

Fig. 2. 15: Von Mises stress of a ϕ104 µm diaphragm at 50 MPa applied static pressure. The diaphragm stress is almost entirely below 0.5 GPa. The maximum stress occurs in a miniscule region at the junction between the diaphragm and substrate.

2.3.3 Bandwidth

The introduction of a dense fluid loading such as water has a well-known effect of reducing bandwidth of hydrophone sensors. As the diaphragms oscillate, some of the fluid moves in phase with the diaphragms. This results in an added dynamic mass that effectively increases the mass of the diaphragm and lowers its resonance frequency. Fig. 2. 16 shows a lumped element model of the diaphragm from a single sensing element in the array. Acoustic pressure p applied over element area S produces a harmonic force that acts over the mechanical impedances of the diaphragm. The diaphragm velocity, $\dot{u}$, induced by acoustic pressure is dependent on the combined values of all impedances acting over the diaphragm, and is described as

$$\dot{u} = \frac{F}{Z_{mtot}} \tag{2.6}$$

Where force $F = F_0 exp(j\omega t)$ and the total mechanical impedance, Z_{mtot}, is

$$Z_{mtot} = Z_{dia} + Z_r \,. \tag{2.7}$$

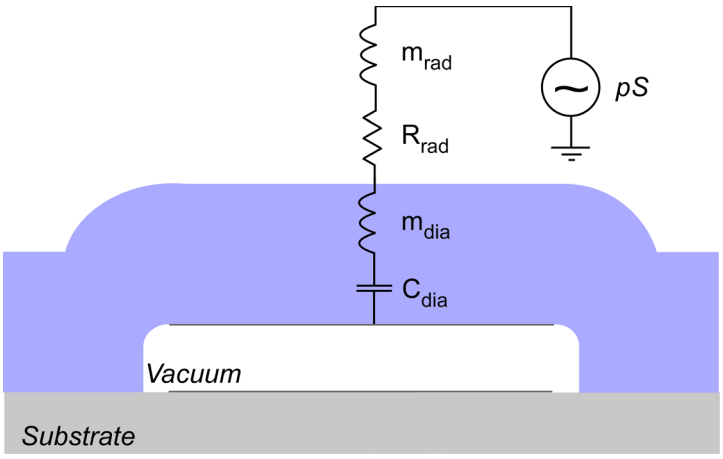

Fig. 2. 16: Lumped element model of a single sensing element from the heterogeneous array. Acoustic masses are represented as inductors, mechanical compliances as capacitors, and mechanical resistances as resistors.

The quantities Z_{dia} and Z_r are diaphragm impedance and radiation impedance, respectively. The diaphragm impedance, Z_{dia}, is from the stiffness and mass of the diaphragm, as well as mechanical resistance of the diaphragm material.

$$Z_{dia} = R_{dia} + j\left(\omega m_{dia} - \frac{1}{C_{dia}\omega}\right) \tag{2.8}$$

The quantity C_{dia} is the mechanical compliance of the diaphragm and is equivalent to the inverse of its spring constant. The diaphragm mass, m_{dia}, is simply the diaphragm density multiplied by its volume. The mechanical resistance, R_{dia}, is dependent on the diaphragm material as well as deposition parameters. This value is dwarfed by the fluid medium radiation resistance and therefore is neglected in calculations. From equation 2.2, the diaphragm compliance is described as

$$C_{dia} = \frac{d_{nom}(p)}{pS}. \tag{2.9}$$

The expression for radiation impedance is more involved than for diaphragm impedance. The radiation impedance of a circular piston is described by [Kin82] as

$$Z_r = \rho c S[R_1(2ka) + jX_1(2ka)], \tag{2.10}$$

where a is diaphragm radius, ρ is fluid density, c is speed of sound in the fluid, k is the wave number ($k = \omega/c$), R_1 is the piston resistance function, and X_1 is the piston reactance function. Functions R_1 and X_1 are described as

$$R_1(x) = 1 - \frac{2J_1(x)}{x} = \frac{x^2}{2\cdot 4} - \frac{x^4}{2\cdot 4^2\cdot 6} + \frac{x^6}{2\cdot 4^2\cdot 6^2\cdot 8} - \cdots \tag{2.11}$$

$$X_1(x) = \frac{2H_1(x)}{x} = \frac{4}{\pi}\left(\frac{x}{3} - \frac{x^3}{3^2\cdot 5} + \frac{x^5}{3^2\cdot 5^2\cdot 7} - \cdots\right). \tag{2.12}$$

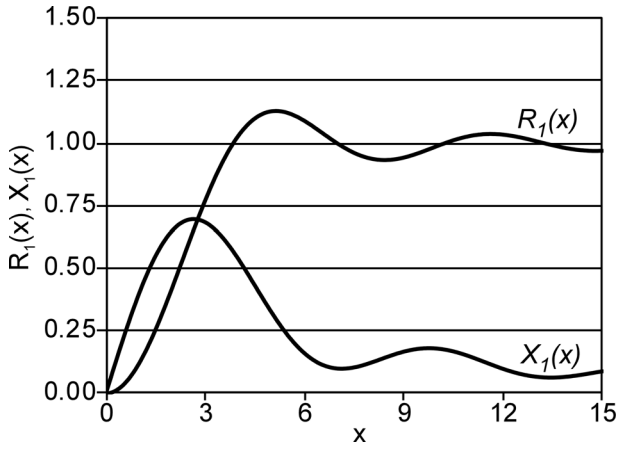

Fig. 2. 17: Analytical plots of piston resistance and reactance functions, $R_1(x)$ and $X_1(x)$.

Functions H_1 and J_1 are the first order Struve function and first order Bessel function of the first kind, respectively. Both R_1 and X_1 are tabulated in Appendix A6 of [Kin82] and plotted in Fig. 2. 17.

Another important factor to consider is the increased compliance due to applied bias voltage, V_{DC}. The applied voltage administers force to the diaphragm, which effectively increases compliance. This phenomenon is referred to as *spring softening* and is described by [Lad98] as

$$k_s = \frac{\varepsilon_r \varepsilon_0 S V_{DC}^2}{d_0^3} \ . \tag{2.13}$$

The resultant diaphragm compliance, C'_{dia}, now becomes

$$C'_{dia} = \left(\frac{S}{d_{nom}} - k_s \right)^{-1} \ . \tag{2.14}$$

The radiation impedance model does not consider viscosity and is therefore technically incomplete. Analysis of conventional hydrophones includes fluid flow through pressure balancing channels, which provides viscosity dependent mechanical resistance that dominates any viscous terms describing diaphragm interaction with the fluid. For this reason, other viscous

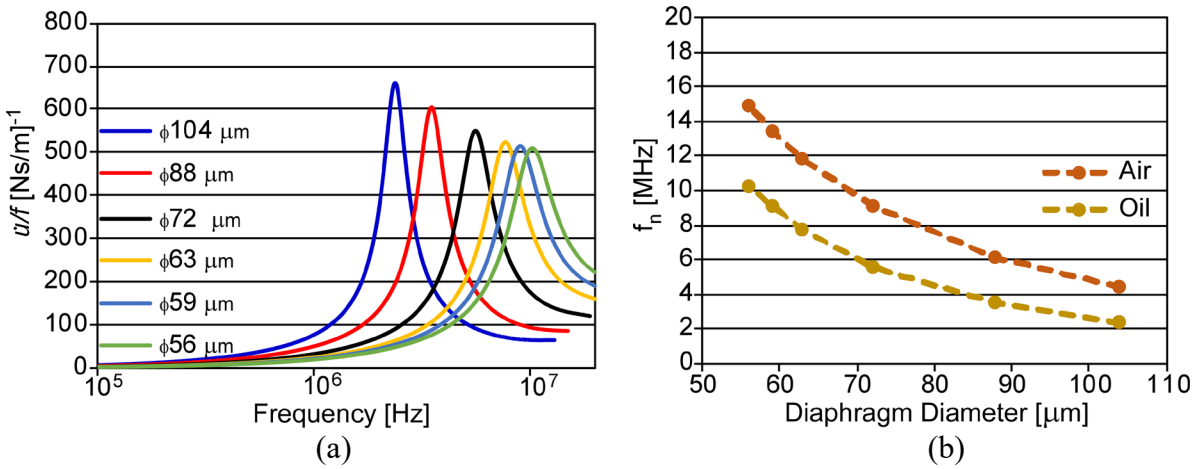

Fig. 2. 18: Analytical lumped diaphragm velocity at frequency obtained using lumped element modeling. (a) Individual diaphragm velocities vs. frequency in oil. The peak of each curve defines the resonant frequency of the diaphragm. (b) Resonant frequencies of individual diaphragms in air and Enerpac™ LX101 paraffin oil deduced from (a).

terms are usually neglected. Although there is an absence of pressure balancing, this viscosity term may still be neglected due to the large effect of radiation impedance [Köy18]. The complete, viscosity dependent mechanical impedance can be found using the Navier-Stokes equation.

The lumped diaphragm velocity in oil per unit applied force is plotted in Fig. 2. 18(a). Each curve represents a single diaphragm. The velocity at low frequency is low, as would be expected from the inverse of equation 2.6. When the mechanical inductance and compliance reach equal and opposite phase, the velocity becomes maximum and resonance occurs. In vacuum, the resonant frequency occurs at

$$\omega_n = \sqrt{\frac{1}{C_{dia} m_{dia}}} \quad . \tag{2.15}$$

When the diaphragms are immersed some fluid will move in phase with the diaphragm, which effectively increases the diaphragm mass and reduces the resonant frequency. This added mass is known as the radiation mass. In this case, equation 2.15 becomes

$$\omega_n = \sqrt{\frac{1}{C_{dia}(m_{dia} + m_r)}} \tag{2.16}$$

where m_r is the radiation mass:

$$m_r = \frac{X_r}{\omega} \ . \tag{2.17}$$

X_r is the radiation reactance and can be calculated from equation 2.10. The resonant frequencies in air and Enerpac™ LX101 paraffin oil are plotted in Fig. 2. 18(b) with respect to diaphragm diameter. Properties of the paraffin oil are listed in Table 2. 3 and detailed in Appendix A. The lumped element modelling shows a distinct drop in resonant frequency between operation in air and oil.

Table 2. 3: Pertinent properties of Enerpac™ LX101 paraffin oil.

Density, ρ	850 kg/m^3 [Ene18]
Speed of Sound, c	1400 m/s

2.3.4 Noise

A major benefit of the microfabrication process is that the diaphragms are hermetically sealed at vacuum. This drastically reduces the amount of diaphragm interaction with sources of random noise. Hydrophones that employ pressure equalization across a sensitive element are particularly susceptible to large amounts of thermal mechanical noise due to flow resistance through perforations and flow channels [Gab93]. Mechanically resistive lumped elements contribute an equivalent noise force that is proportional to the square root of the mechanical

resistance. The relationship that describes this phenomenon is known as Nyquist's Relation [Gab93]. The equivalent noise force spectral density is described as

$$\overline{f_n^2} = 4k_B TR\,, \tag{2.18}$$

where k_B is Boltzmann's constant (1.38×10^{-23} J/K), T is absolute temperature in Kelvin, and R is mechanical resistance. The diaphragm of each sensing element has two mechanically resistive elements; the diaphragm's own mechanical resistance as well as radiation resistance from the fluid medium. The diaphragm mechanical resistance, R_{dia}, is from factors such as losses due to thermoelasticity of the material. For hydrophone applications, thermal mechanical noise is dominated by radiation resistance. The diaphragm's mechanical resistance is therefore neglected.

Each sensing element provides thermal mechanical self-noise to the sensor through interactions with fluid molecules. This noise is due to Brownian motion and radiation resistance, though radiation resistance is the dominant noise source. The noise from each sensing element is found using Nyquist's Relation as well as the radiation resistance, which, from equation 2.10, is

$$R_r = \rho c S R_1(2ka) \tag{2.19}$$

The equivalent noise source from equation 2.18 gives the equivalent mean square noise force, which is converted to pressure and multiplied by an element's incremental response to obtain the resultant capacitance noise value. The contribution from each sensing element is combined and divided by total sensor incremental response to find the total mean square radiation noise pressure spectral density, $\overline{p_{nr}^2}$, experienced by the sensor:

$$\overline{p_{nr}^2} = \frac{\sum_{n=1}^{n=N} 4k_B TR_{rn}R_n / S_n^2}{R_{tot}} \tag{2.20}$$

R_n refers to incremental response of the nth sensing element in units of Farads·Pressure^{-1}, S_n is diaphragm area of the nth sensing element, R_{rn} is the radiation resistance of the nth sensing element, R_{tot} is the total sensor incremental response, and N is the total number of sensing elements present in the array. Both the total sensor incremental response and the incremental response of each individual sensing element must be known for equation 2.20 to be viable. Brownian noise, on the other hand, is only dependent on frequency and temperature of the fluid. The one-sided power spectral density due to Brownian noise is as follows [Cha87a]:

$$\overline{P_n^2} = \frac{4\pi k_B T \rho f^2}{c} \tag{2.21}$$

where $\overline{P_n^2}$ is the mean square power spectrum of the pressure fluctuation associated with thermal mechanical noise. The power spectrum increases with the square of frequency and as a result is most notable at high frequencies.

Analytical noise pressure spectral density due to Brownian motion as well as radiation impedance is plotted in Fig. 2. 19(a). The radiation impedance noise was calculated for each individual diaphragm size in the array, ranging from ϕ104 μm to ϕ56 μm, using equation 2.22. As is shown in the figure, all diaphragms yield the exact same equivalent noise spectral density until well above 1 MHz. A closeup of the radiation impedance noise from 4 to 10 MHz is shown in Fig. 2. 19(b). The maximum difference in noise spectral densities between diaphragms is 2.7 dB, between the smallest and largest diaphragms. Larger diaphragms yield lower impedance due to the area^{-1} term used to obtain pressure from force in equation 2.14. The similarity in noise spectral density between diaphragms affords a simplification in equation 2.20 when calculating the total noise spectral density contributed by radiation impedance. The identical pressure for each diaphragm, $\overline{p_r^2}$, is factored out of the summation:

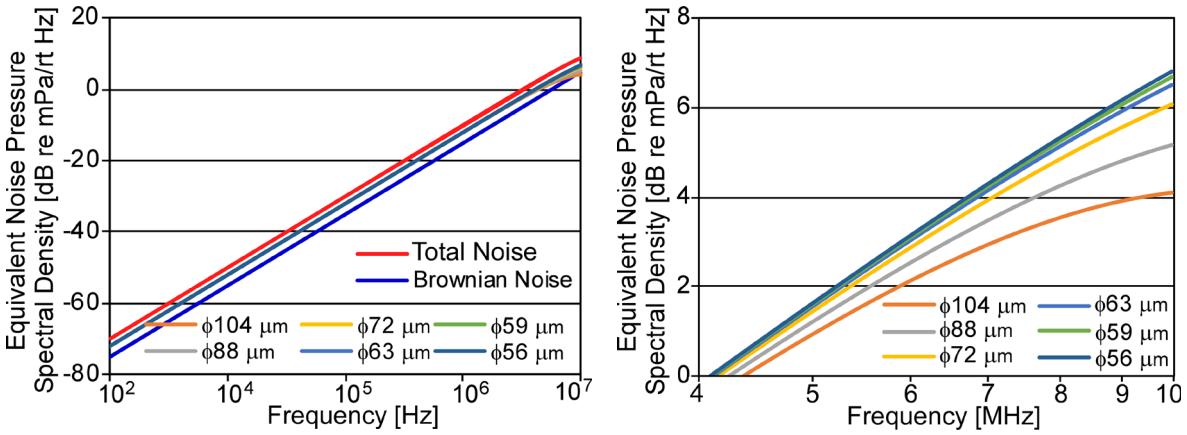

Fig. 2. 19: Analytical thermal mechanical noise at 298 K. (a) All thermal mechanical noise sources, including Brownian noise and noise from radiation impedance for each individual diaphragm. Total thermal mechanical noise is also plotted. (b) Closeup view of radiation impedance noise of each individual diaphragm. Spectral density of all diaphragms is identical until above 4 MHz. At 10 MHz, the maximum difference between diaphragms is 2.7 dB.

$$\overline{p_{nr}^2} = \overline{p_r^2}\frac{\sum_{n=1}^{n=N} R_n}{R_{tot}} = \overline{p_r^2}\frac{R_{tot}}{R_{tot}} = \overline{p_r^2}\,. \tag{2.22}$$

This means that the total mean square radiation noise pressure experienced by the sensor is equal to that calculated for a single diaphragm. The equation used to calculate diaphragm radiation noise is therefore

$$\overline{p_{nr}^2} = \frac{4k_B T R_r}{(\pi a^2)^2}\,. \tag{2.23}$$

Equation 2.23 is derived from equations 2.18 and 2.19. The total noise spectral density, including Brownian noise, is plotted in Fig. 2. 19(a).

2.4 Experimental Testing

2.4.1 Static Pressure Response

The sensor capacitance response to change in applied static pressure is shown in Fig. 2. 20. The experimental curve (green) is compared to FEA simulation (blue), which shows a close

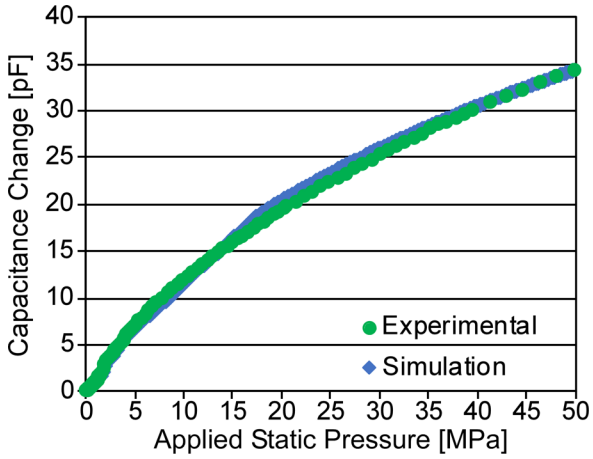

Fig. 2. 20: Capacitance change with applied static pressure from sensor H106 B1.

match. The simulated curve does show a less rounded response, particularly just before diaphragms enter touch mode (transition mode). This is reflected in the extrapolated incremental response plot, shown in Fig. 2. 21. This plot is obtained by manually approximating the incremental response (equation 2.5). Each curve shows five prominent peaks in incremental response, with each peak from the simulated curve being larger in magnitude. This is likely from the simulation assumption that surface roughness is linear, when in actuality there could be a gradient with higher thickness at the center. Such a gradient would result in similar response in

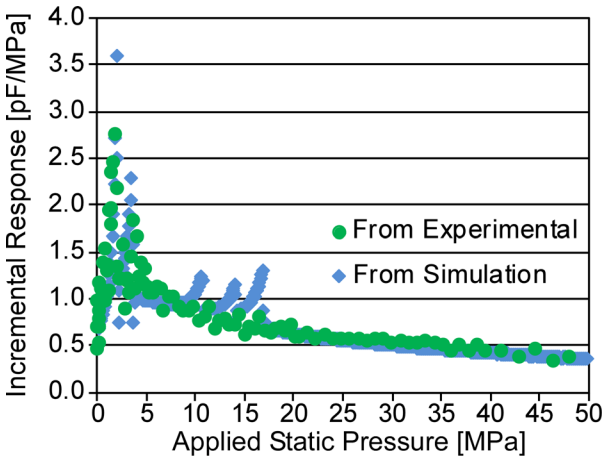

Fig. 2. 21: Sensor H106 B1 incremental response, extrapolated from both experimental and simulated static pressure responses. The curves are well aligned. The simulated curve shows higher incremental response in transition mode than the experimental.

touch mode but reduced incremental response in transition mode as is observed here. The gradient cannot be estimated due to the virtually random nature of these fabrication non-idealities. It is therefore more meaningful to quantify such non-idealities experimentally than to attempt to predict them.

2.4.2 Repeatability

Repeatability is a required aspect of virtually any microfabricated sensor. This quality is demonstrated Fig. 2. 22. Here, the static pressure response from four unique H106 sensors is shown. All sensors are from the same fabrication batch, and the responses are representative of the entire batch. The curves show a general agreement, with some variation in response present. Some variation is expected. The total capacitance change over the full static pressure range,

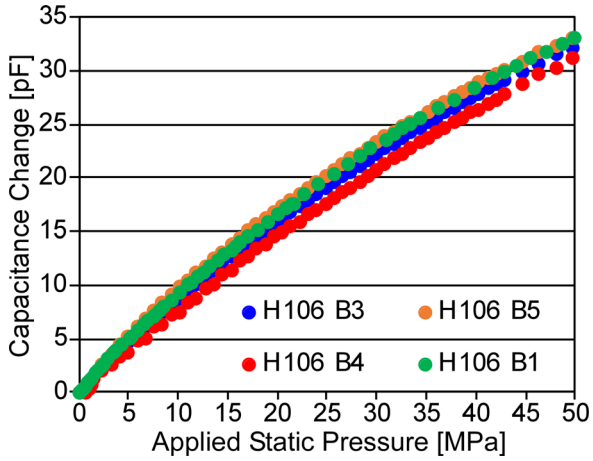

Fig. 2. 22: Static pressure response from four unique H106 heterogeneous hydrophones. Chips were fabricated in the same batch. There is an acceptable spread between sensors.

Table 2. 4: Maximum capacitance change values from each curve, along with deviation.

	ΔC_{max}, 49.8 MPa	%Deviation from Average
H106 B1	33.117 pF	2.23%
H106 B3	32.176 pF	0.68%
H106 B4	31.207 pF	3.67%
H106 B5	33.079 pF	2.11%
Average ΔC_{max}, 49.8 MPa	32.395 pF	

ΔC_{max}, for all sensors is tabulated in Table 2. 4 along with their deviations from the average. The average value was 32.395 pF. There was very little deviation from this value, the largest being 3.67% and smallest being 0.68%. These numbers are acceptable and demonstrate repeatability of the sensor.

Next, the incremental response from all four static curves is extrapolated and plotted in Fig. 2. 23. All four curves show a large peak in incremental response at low pressures corresponding to the large diaphragms entering transition mode. The peaks from each curve are close in value. As pressure increases, the incremental response decreases at the same rate for all sensors.

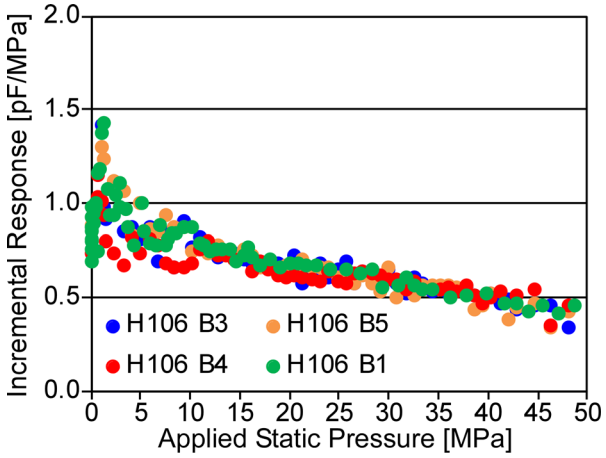

Fig. 2. 23: Extrapolated incremental response from each of the four H106 sensors. Sensors are in general agreeance throughout the 50 MPa static pressure range.

2.4.3 Observed Change in Response

The static pressure response and hence the extrapolated incremental response vs. applied static pressure were found to change over time as the sensors were in use. These changes are quantified in H106 B1 and H106 B5 in Fig. 2. 24 and Fig. 2. 25, respectively. The static pressure response of H106 B1 is shown in Fig. 2. 24(a). The response changed over a period of

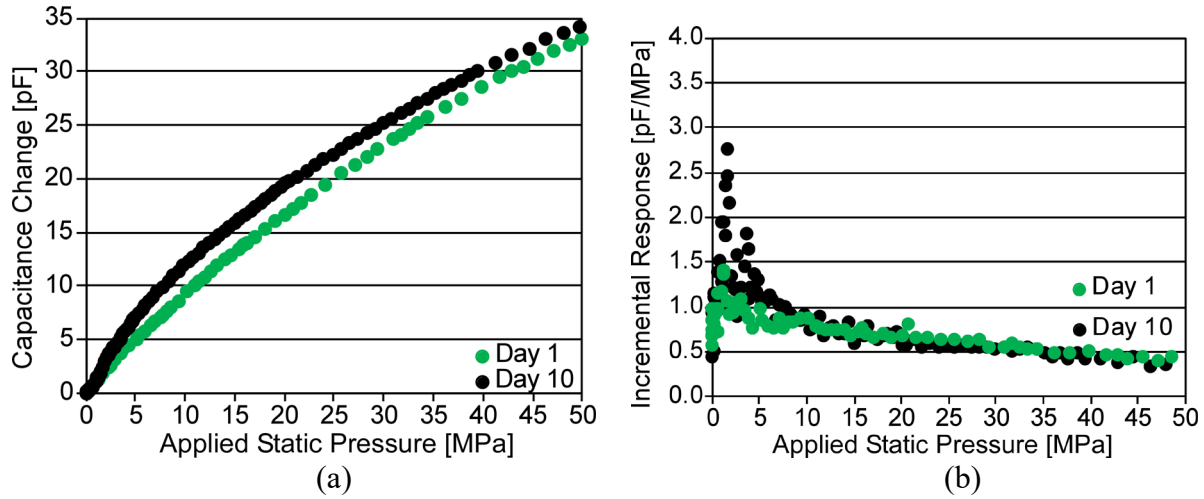

Fig. 2. 24: Observed change in sensor H106 B1. The day 10 curve from both plots is shown in Fig. 2. 20 and Fig. 2. 21. (a) Measured static pressure response. (b) Extrapolated incremental response.

10 days; this sensor was used extensively in multiple tests. The curve in (a) shows a pronounced increased in capacitance change almost entirely at low static pressures, which implies that the larger sensing elements have considerable change in incremental response. The change in static response is reflected in the extrapolated incremental response change in (b). The incremental response at lower pressures is high while the incremental response at higher pressures is about the same. The static response from H106 B5 in Fig. 2. 25(a) shows a similar increase in

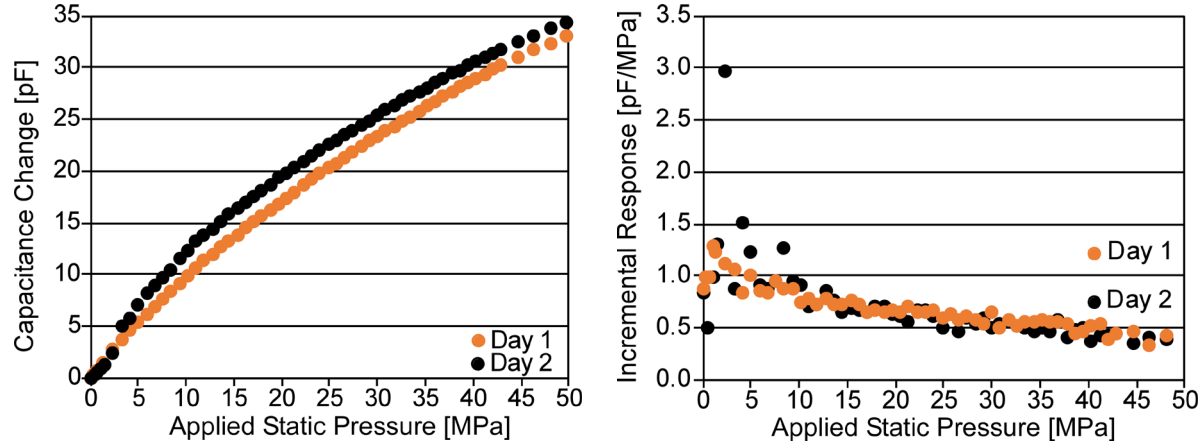

Fig. 2. 25: Observed change in sensor H106 B5. (a) Measured static pressure response. (b) Extrapolated incremental response.

response at low static pressures. Comparing the results from both sensors, it is deduced that the larger sensing elements have some yielding while the smaller sensing elements have very little if any yielding. This observation is intuitive, because both the radial and tangential stresses change proportionately to a^2h^{-2}. Both sensors show about the same change in response, regardless of the fact that H106 B1 encountered much more use. This implies that the diaphragms undergo some "breaking in." This is explained by the Von Mises stress simulation in Fig. 2. 14, which reveals some yielding in the largest diaphragm.

2.4.4 Electromechanical Resonance Testing

The resonant frequencies of each diaphragm size can be experimentally validated by applying an RF signal to the sensor and measuring sensor impedance as a function of frequency. The resonant frequency is defined as the frequency at which the real part of the impedance is maximum [Ora06]. In this work, the H106 hydrophone was connected to an Agilent 4395A Impedance/Spectrum/Network Analyzer in impedance analyzer mode. An RF signal was applied

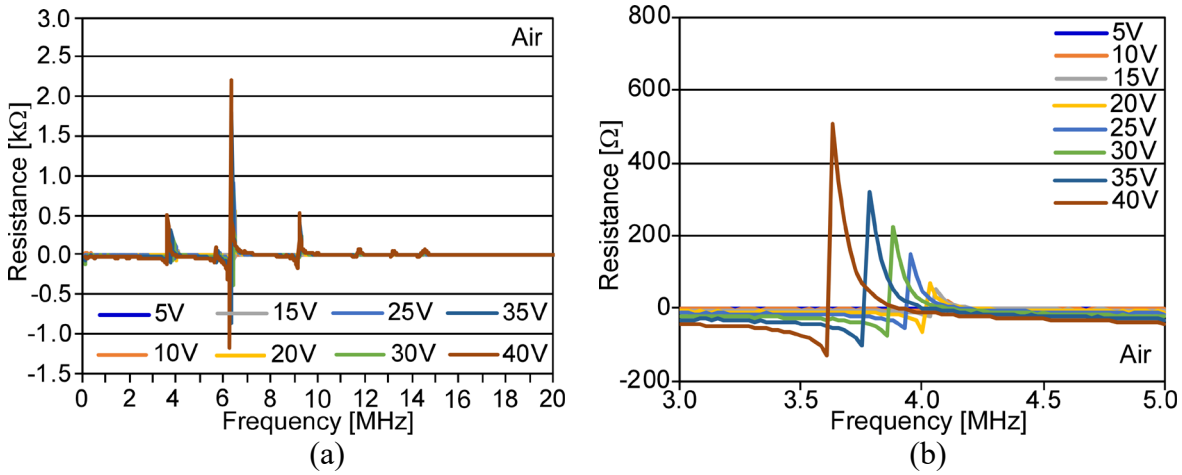

Fig. 2. 26: Real part of the measured H106 B1 electrical impedance vs. frequency at varying bias voltages in air. (a) Full spectrum resistance. Each positive peak denotes the resonant frequency of one diaphragm size. There are six different sizes of diaphragm used in the array. (b) Closeup of the largest diaphragm resonating. The change in frequency and magnitude is from spring softening, resulting from increased bias voltage.

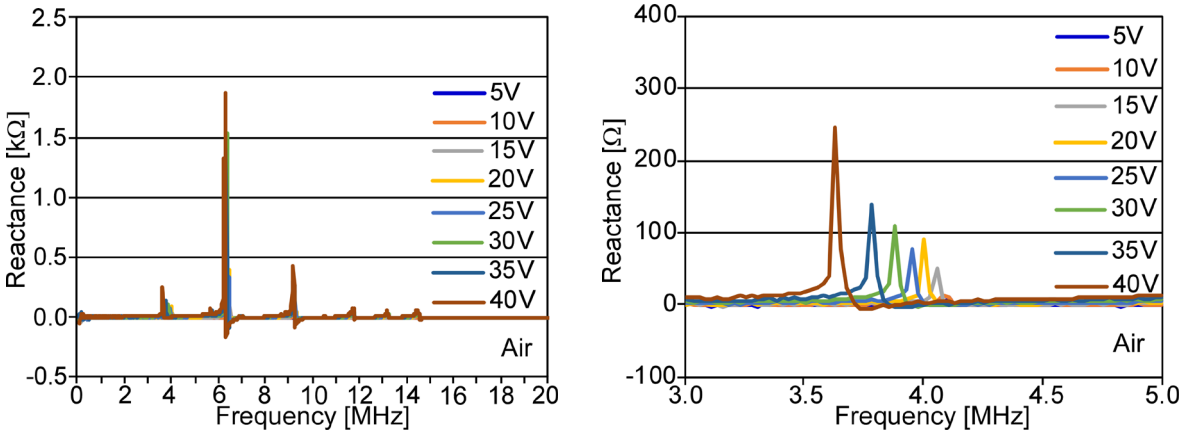

Fig. 2. 27: Imaginary part of the measured H106 B1 electrical impedance vs. frequency at varying bias voltages in air. Results compare favorably to resistance measurements. (a) Full spectrum reactance. (b) Closeup of the largest diaphragm resonating. Just as in the real part, the change in frequency and magnitude is due to spring softening from the applied bias voltage.

over different bias voltages. The electrical resistances representing the real part of the impedance measurement in air is shown in Fig. 2. 26. The entire testing bandwidth up to 20 MHz is shown in (a) at varying bias voltage, while (b) shows a closeup view of the first diaphragm to resonate. There are six diaphragm sizes used in the array, the larger of which resonate at lower frequencies. There are seven discrete peaks shown in (a); an extra peak is likely caused by a distribution of resonant frequencies of the ϕ88 μm diaphragm, of which there are 13. The application of a bias voltage lowers the resonant frequency and raises the diaphragm displacement due to spring softening. This effect can be clearly seen in (b). The resonant frequency of the largest diaphragm occurs at 4.105 MHz with a 10V bias and 3.632 MHz with a 40V bias. The imaginary component of impedance is shown in Fig. 2. 27 for reference.

Next, electromechanical resonance measurements were performed with the diaphragms submerged in Enerpac™ LX101 paraffin oil and biased to 40V. Results are shown in Fig. 2. 28, with resistance in (a) and reactance in (b). Both plots show an increased number of resonances relative to air ambient, with the first resonance occurring at 2.314 MHz compared to 3.632 MHz

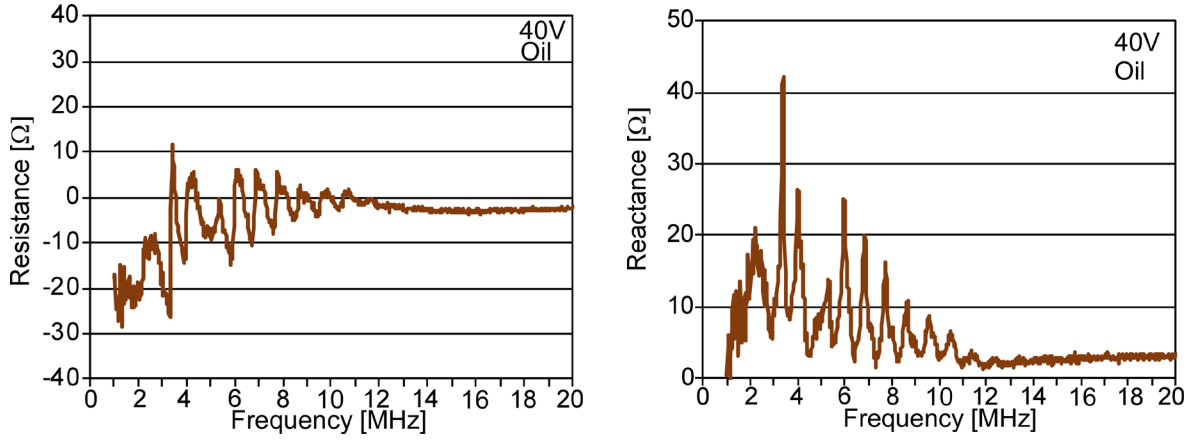

Fig. 2. 28: H106 B1 electrical impedance measurements in Enerpac™ LX101 paraffin oil at 40V bias. (a) Real part. The lowest resonant frequency is 2.314 MHz. (b) Imaginary part. Both plots show more resonances than expected when compared to air ambient.

in air at 40V. The magnitude of impedance magnitude at each resonance is lower than those seen in air due to the increased mechanical resistance provided by the radiation impedance of the fluid. The increased number of resonances in both (a) and (b) imply that some diaphragms of the same size are affected differently by the fluid loading. Fig. 2. 29(a) shows the experimental resonant frequencies in air and oil compared to the frequencies predicted by lumped element modeling. Since there are more resonances in oil than anticipated, only the first two resonant frequencies are

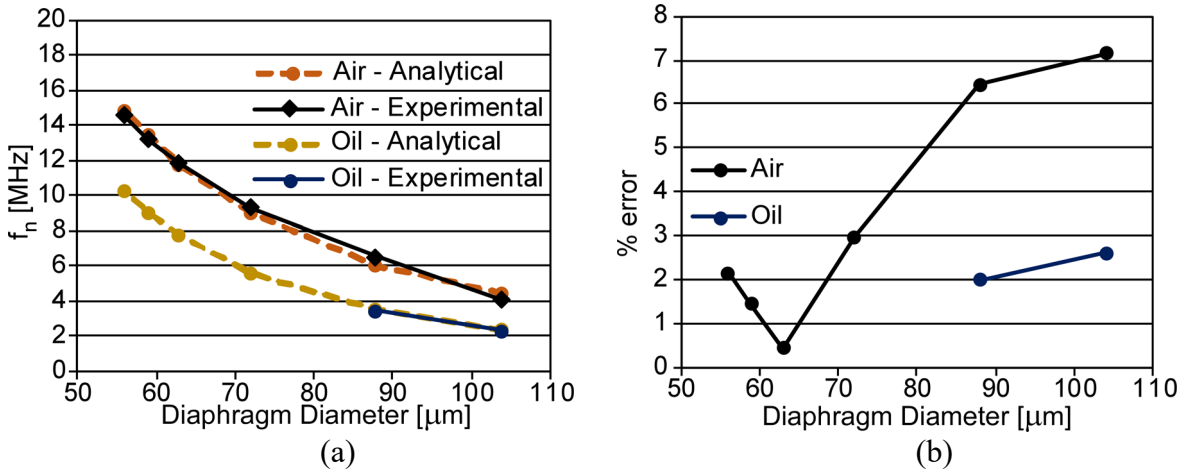

Fig. 2. 29: Experimental H106 B1 resonant frequencies in air and oil. (a) Resonance values of different diaphragm sizes plotted with analytical values for comparison. (b) Percent error. Maximum percent error occurs with larger diaphragm sizes.

plotted for oil. These two major resonances are for certain the two largest diaphragms, and therefore can be easily plotted in the figure. The diaphragm sizes for remaining resonances cannot be known with certainty and are not plotted in Fig. 2. 29(a). The percent error between analytical and experimental resonant frequencies are shown in Fig. 2. 29(b).

2.5 Discussion and Summary

Chapter 2 presents a new type of microfabricated hydrophone. The design concept and architecture are described. The static pressure response is modeled using FEA. Performance in the frequency domain is modeled with lumped element modeling (LEM). The sensor design is experimentally verified, including static response, extrapolated incremental response, repeatability, performance over time, and bandwidth. Electromechanical resonance testing in air and oil confirms extremely wide bandwidth well into the MHz band.

The heterogeneous micro-hydrophone has qualities not available in current hydrophone technology. The surface micromachined sensing elements are hermetically sealed at vacuum. This allows for packaging using only deposited parylene [Zhu07] or some other polymer. It also allows for extremely small form factor, provides unparalleled protection of the interelectrode gap, enables static sensing capability, and drastically reduces thermal mechanical noise. Touch mode operation virtually eliminates concerns of pressure overloading. This hydrophone is compatible with autonomous microsystems, which has not been previously reported.

Chapter 3: ELM Integration and Seismic Testing

This chapter describes the Environmental Logging Microsystem (ELM) for monitoring of conditions in harsh environments (Fig. 3. 1(a)). As mentioned previously, pressure and temperature data are needed for oil well production efficiency and safety. The autonomous microsystems presented can be deployed downhole and autonomously collect pressure and temperature data, all while managing system power and functionality. Integration of an acoustic sensor can enable collection of supplementary seismic data, wireless downhole communication, and even geolocation of the microsystem. Each microsystem consists of a flexible printed circuit board (PCB) and custom selected, commercial, off-the-shelf electronic components. The PCB can be folded and packaged in custom designed, low cost, high throughput packaging that provides abrasion resistance and chemical resistance. A lithium coin-cell battery provides power to the system. Optical communication is utilized for system programming and data retrieval, as

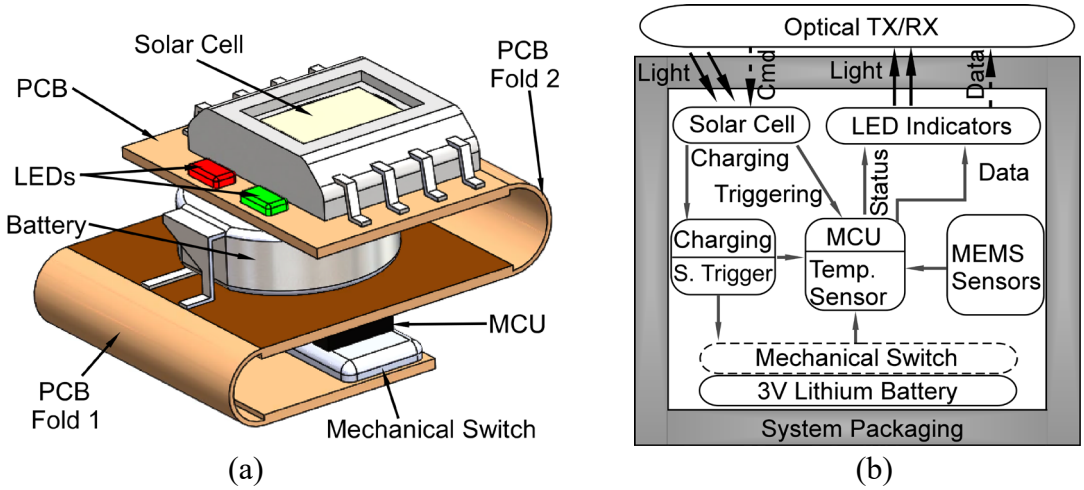

Fig. 3. 1: ELM autonomous microsystem. (a) 3D depiction of an unpackaged microsystem. (b) Block diagram of ELM system.

well as energy harvesting. System state is managed using software written into the microcontroller unit (MCU). There are two variations in ELM models[2]; the differentiating characteristic is a mechanical power switch that commands larger PCB area. These systems are intellectually identical. This work focuses on the third generation ELM system, which includes a mechanical switch for increased battery shelf life.

3.1 ELM Architecture and System Hardware

The major components of the ELM system are the PCB, MCU, charging circuit, solar cell, LEDs, and micromachined sensor. Fig. 3. 1(b) shows a block diagram of the system and its operation. An optical transceiver (TX/RX) readout box is utilized to communicate with the MCU. A solar cell generates a voltage from incoming light, which produces a binary signal for communication with the MCU. The MCU is responsible for functional control, data storage, communication, and power management. Notably, the MCU has on onboard temperature sensor

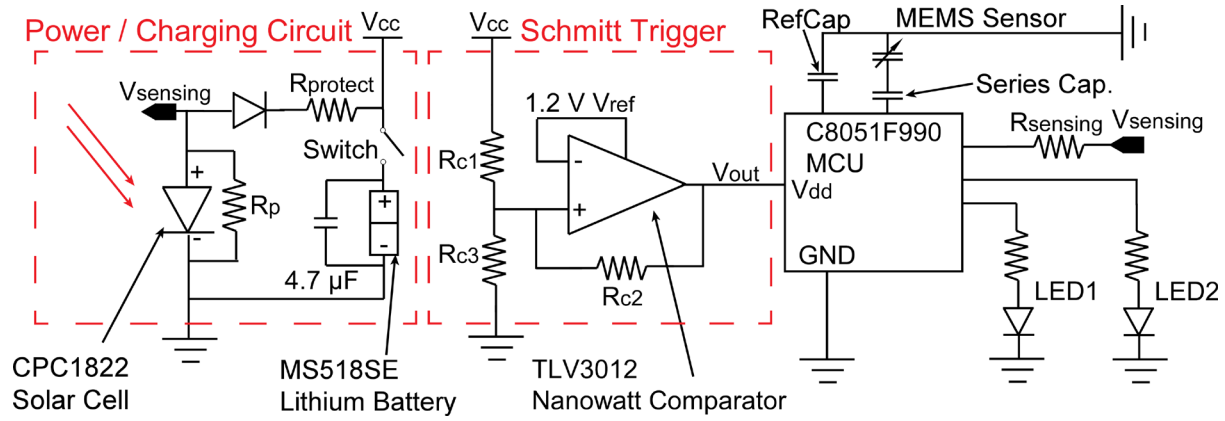

Fig. 3. 2: ELM system circuit diagram.

[2]The systems were developed in a collaborative effort that included Dr. Yu Sui, Dr. Yushu Ma, Mr. Ryan Meredith, and Ms. Neeharika Vellaluru.

as well as capacitance to digital converter; these modules are used extensively. A charging circuit is integrated with the PCB and assists with wireless optical charging of the 3V lithium coin cell battery as well as triggering of the MCU. Wireless charging occurs when the solar cell is continuously exposed to bright light from an external source. Measured data is stored in the MCU's flash memory and is relayed back to the readout box through LED indicators. A mechanical switch manages connection of the battery to the system to increase shelf life.

A diagram of the ELM circuitry can be found in Fig. 3. 2. The circuitry consists of three sections: charging circuit, Schmitt trigger, and MCU sensing and communication. The charging circuit contains a Clare CPC1822 solar cell, a rectifier diode to prevent reverse flow of charging current, resistor $R_{protect}$ to limit charging current, a mechanical switch, a Seiko Instruments MS518SE lithium coin cell battery, and a buffer capacitor in parallel with the battery. The buffer capacitor is used to provide any transient current needed when the system is active. Resistor R_p is used for optical triggering and has no function in the charging circuit. Incident light on the solar cell generates a charging current that flows through the rectifier diode and protection resistor to the battery, assuming the switch is closed. Pulsed light patterns on the solar cell also generate

Table 3. 1: Major ELM electrical components.

Component	Part No.	Footprint	Features
MCU	Silicon Labs C8051F990	3 × 3 mm^2	0.8 µA sleep mode current, 80 µA active current, 32 kHz internal oscillator, integrated temperature sensor
Battery	Seiko MS518SE	Φ5.8 mm	3.4 mAh nominal capacity, 150 µA max. discharge current
Solar Cell	Clare CPC1822N	6 × 5 mm^2	4.2V nominal output voltage, 50 µA nominal current (6000 lux input)
Comparator for Schmitt Trigger	TLV3012AIDCKR	2.1 × 2.4 mm^2	2.8 µA current usage, 1.2V reference
Mechanical Switch	401-2016-1-ND	8.3 × 5 mm^2	300 mA at 6 V DC, 100 MΩ min. resistance when closed

voltages at the $V_{sensing}$ node, which is measured by a comparator circuit inside the Silicon Labs C8051F990 MCU. Resistor R_p creates a current flow path between the two terminals of the solar cell, which generates the measured $V_{sensing}$ voltage drop. The MCU's comparator reads a binary signal from the $V_{sensing}$ node, based on the timing of pulsed light from the readout box. The Schmitt trigger is used to protect the system from waking up when the battery voltage is low. This is because the current draw of the system is extremely high when the battery voltage is low. The Schmitt trigger provides hysteresis to avoid the system waking up below a predetermined voltage. A list of major circuit components and their characteristics can be found in

The Silicon Labs C8051F990 microcontroller unit measures capacitance using an onboard capacitance to digital converter (CDC). A reference capacitor with negligible temperature coefficients is used for calibration purposes. The custom micromachined sensor, whether a single diaphragm pressure sensor or a hydrophone array, is in series with a capacitor to avoid damaging the MCU circuitry if the sensor were to short. Once a measurement is taken, data is first stored in onboard flash memory and then relayed to the readout box through the LEDs. The system state is determined by the MCU software programming, which is explained in the next section.

3.2 System Software

The onboard microcontroller unit is programmed using C++ software[3] to manage system state, control system functionality, manage power, collect and store data, and bidirectional

[3] The control software was developed by Dr. Yu Sui and Mr. Ryan Meredith

communication with the transceiver readout box. The software is optimized for low power consumption, low memory usage, stability at high temperature, and straightforward operation.

The entirety of the system's operation consists of 10 states listed in the Fig. 3. 3 state diagram. State 1 is the MCU off state in which $V_{cc}<V_{th}$; the MCU is off and the system is unable to operate. When the battery voltage is high enough so that $V_{cc}>V_{th}$, the system enters State 2. The MCU turns on and initializes its function registers, then enters State 3 – Deep Sleep State. Deep Sleep State renders the system in a low power mode where the system can either rest or be triggered into another state. The system will typically spend most of its time in the Deep Sleep State. State 4, the Readout State, puts the system in a mode in which it can optically relay measurement data previously stored in the MCU's flash memory. Data transfer occurs using a cyclic redundancy check (CRC) to ensure accurate communication. Before being deployed in the environment to be monitored, the system is triggered into the Detection State. In the Detection State, the system wakes up from Deep Sleep every 2 minutes (or other programmed time interval) and activates the temperature sensor, CDC module, and analog to digital converter

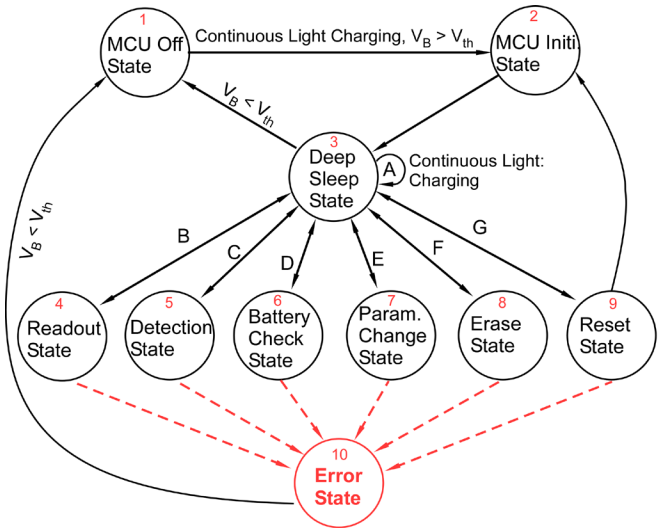

Label	# Pulses (n)	Range
A	1	0 = n < 2
B	2	2 = n < 3
C	4	3 = n < 6
D	7	6 = n < 8
E	8	8 = n <10
F	10	10 = n < 12
G	12	12 = n < 15

Fig. 3. 3: ELM software state diagram. Transition between states is done through optical triggering. The number of pulses for each state is tabulated.

module. Data measurements are taken and stored in flash memory before the system goes back into a deep sleep mode. This process is repeated until the system is manually triggered out of Detection State or the battery depletes. State 6 is the Battery Check State in which the MCU uses its onboard comparator to measure the battery voltage. This voltage value is converted to digital and relayed through wireless communication. The Parameter Change State, State 7, is used when the system is being interrogated by the optical readout box. This state allows for parameters such as measurement time interval and capacitive sensor channel to be changed. State 8 is the erase state, where the MCU erases all collected data from flash memory. State 9, the Reset State, the system is manually reset and all function registers are refreshed. Lastly, the system will enter State 10, the Error State, if any unexpected failure occurs.

3.3 ELM Implementation

The ELM system has previously been packaged and tested with integrated sensors. These tests were performed in different environments, including an active brine well. Depending on the situation, the PCB can be folded to reduce overall form factor. Fig. 3. 4 shows an

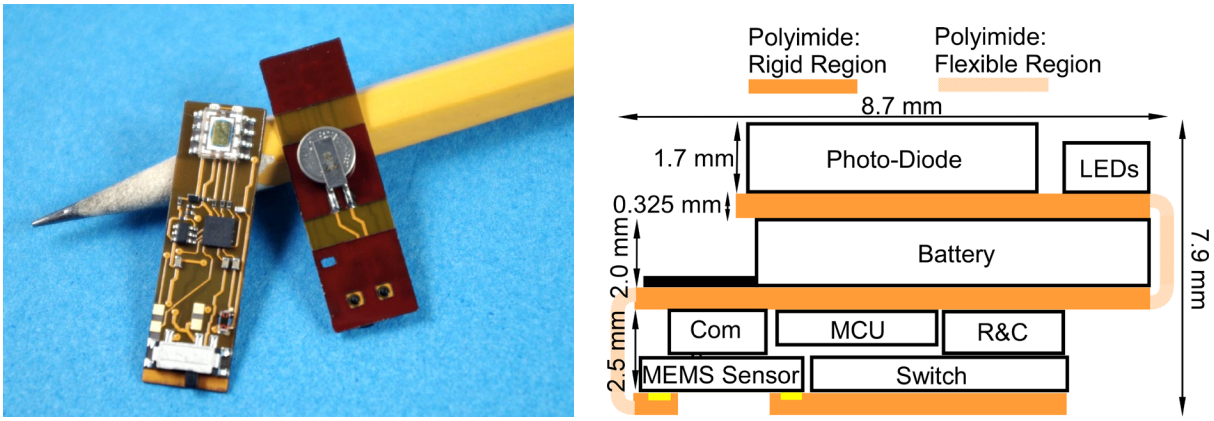

(a) (b)

Fig. 3. 4: Unpackaged ELM system and stack configuration. (a) Unpackaged ELM system with an integrated pressure sensor. (b) Folded PCB dimensions. PCB is 8.6 mm into the page.

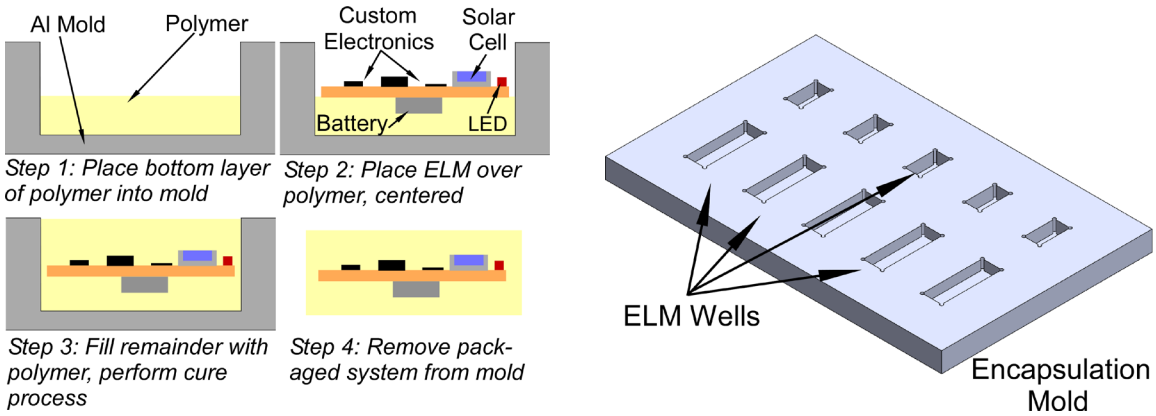

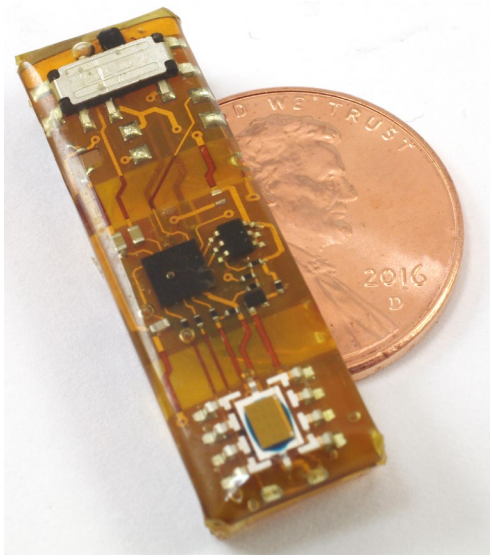

(c)

Fig. 3. 5: ELM encapsulation. (a) Simplified encapsulation procedure. (b) Aluminum mold. (c) Fully packaged ELM system. Here, proprietary epoxy is used as the encapsulant.

unfolded, unpackaged ELM system in (a), along with a diagram of a folded system in (b). The diagram shows approximate folded dimensions of the stack, with the depth into the page listed in the caption as 8.6 mm. When implemented in a testing scenario, the microsystem is encapsulated in a protective polymer; in the past, silicone caulk (Do It Best® Clear Silicon Caulk) or proprietary epoxy have been used. Fig. 3. 5(c) shows a fully encapsulated ELM system encapsulated in proprietary epoxy. The testing scenario did not require a folded PCB, hence the PCB is laid flat. An aluminum mold is used to encapsulate the ELM systems in

parallel. Fig. 3. 5(a) shows the simplified process flow. First, the bottom layer of the mold is filled with a small amount of polymer to ensure total coverage of the system. To facilitate removal at the end of the process, a thin plastic layer of hydrophobic polysiloxanes such as Rain-X^{TM} can be applied before any polymer is introduced. Next, the flat system is placed in the mold and centered. The remainder of the mold is then filled with polymer and allowed to cure.

The microsystem was field tested in an active brine well. Systems such as the one shown in Fig. 3. 5(c) were integrated with a JONC rod and lowered via winch into the well. Please see Fig. 3. 6 and Fig. 3. 7 for reference. These systems were encapsulated and laid flat in metal clamps, as shown in Fig. 3. 7. These clamps were wrapped around a rod, referred to as a JONC rod, which is a plastic rod with a metal core, and lowered into the well via winch. A macroscale wireline monitor was also integrated with the rod for reference pressure and temperature values.

Fig. 3. 6: Field testing. A wireline runs from a winch situated in a truck (left), which lowers the microsystems into the well. The systems are attached to a JONC rod (right) using metal clamps. A macroscale wireline monitor is also connected to the rod for reference.

Fig. 3. 7: The ELM systems are laid flat inside metal clamps, which are then tightened around a JONC rod and lowered into the well.

The field-tested microsystems were integrated with single diaphragm pressure sensors, specifically model C100. This C100 consisted of a single ϕ100 µm capacitive sensing element with a 5.0 µm thick diaphragm and 1.0 µm interelectrode gap. The systems were lowered into the well to a maximum depth of 1235 m. Pressure increase was due entirely to the increase in depth. The maximum hydrostatic pressure reached was not enough to induce touch mode operation in the sensor. In its non-touch mode regime, this C100 sensor can resolve 32.4 kPa (4.7 psi) and has a capacitance response of 31.0 fF/MPa (0.21 fF/psi).

The field-testing results are shown in Fig. 3. 8. The systems were lowered into the well and halted for three short time intervals on the return to the surface to generate a staircase profile, as seen in the figure. The capacitance and temperature measurements stored by the

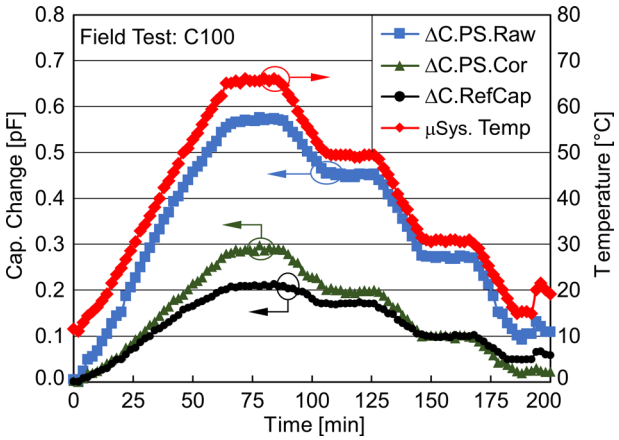

(a)

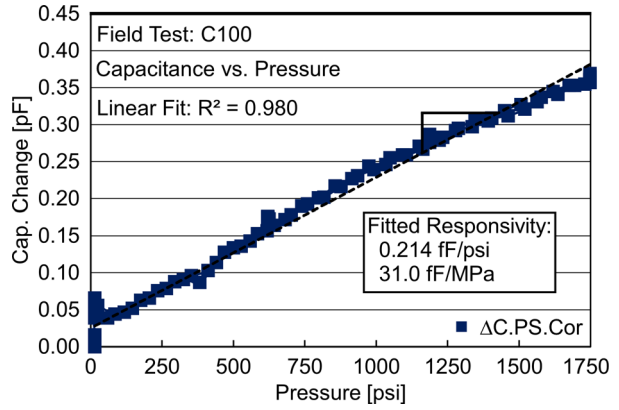

(b)

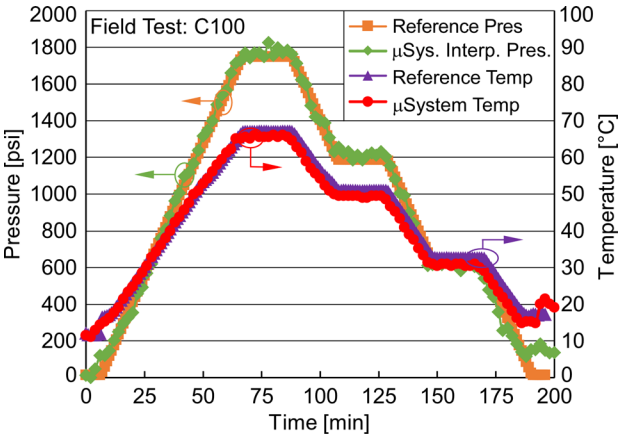

(c)

Fig. 3. 8: ELM field testing results with an integrated C100 pressure sensor. (a) Capacitance and temperature data collected from the microsystem. The value of a reference capacitor is subtracted from the raw capacitance data to correct for temperature effects. (b) Extrapolated capacitance response. The sensor never enters transition or touch mode, resulting is quasi-linear operation. (c) Interpreted pressure measurements compared to reference values.

microsystem are shown in (a). A temperature insensitive reference capacitor measurement (ΔC.RefCap) is included in each measurement cycle to allow for temperature calibrations. The reference capacitor's value is subtracted from the raw pressure sensor value (ΔC.PS.Raw) to create a corrected pressure sensor value (ΔC.PS.Cor). The extrapolated capacitance vs. static pressure response of the pressure sensor is shown in (b). Since the pressure doesn't reach a high enough value to induce transition or touch mode in the sensor, the sensor's response is quasi-linear in non-touch mode. Fig. 3. 8(c) shows the interpreted pressure values, along with the reference wireline monitor data for comparison. There is a slight disagreement in ELM interpreted pressure and reference pressure near 200 minutes; this is caused by residual stresses in the PCB solder joints. This issue has since been resolved through annealing.

3.4 Hydrophone Sensor Integration

Integration of the hydrophone with an ELM system required modification of the capacitance sensing protocol and integration with PCBs that were not originally intended for use with the hydrophone. The existing MCU capacitance conversion software was modified to increase the number of capacitance measurements per detection cycle, as well as to modulate the acoustic sampling frequency. An onboard timer was programmed to count to a predetermined value, after which it generates an interrupt that informs the MCU to perform another capacitance conversion. The timer count determines the sampling frequency. The converted capacitance data is briefly stored in RAM before being written to flash memory before the system enters Deep Sleep. The system can make 30 capacitance conversions per measurement cycle, limited by available RAM and flash memory. The MCU is capable of sampling frequencies as high as 30 kS/s, however the

sampling rate for this work was chosen to be 200 S/s based on the acoustic frequency band of interest.

A noise analysis was done through analytical calculation. The dominant noise source from the sensor is Johnson noise. Brownian noise was also considered but was found to be negligible compared to Johnson noise. The hydrophone operates at extremely low frequency and is sealed at vacuum, so thermal mechanical noise sources that influence most hydrophones are not applicable in this case. The noise from radiation resistance associated with fluid interactions with the diaphragm is negligible in the frequency range of interest. Furthermore, there is no squeeze film damping because the diaphragms are sealed at vacuum. Chau and Wise [Cha87b] describe the mean square noise pressure due to Johnson noise as

$$\overline{P_n^2} = \frac{k_B T (C_0 + C_{par})}{(V_s R)^2}. \tag{3.1}$$

Using Boltzmann constant $k_B = 1.38\ 10^{-23} J/K$, absolute temperature $T = 300\ K$, nominal baseline capacitance $C_0 = 9.0\ pF$, parasitic capacitance $C_{par} = 0.2\ pF$, sensing voltage $V_s = 3V$, and nominal incremental response $R = 560\ fF/MPa$, equation 3.1 yields a value of $P_n^{rms} = 116.2\ Pa$. This value describes the hydrophone sensor's self-noise and serves as the theoretical minimum pressure change the sensor can measure. Multiplying by incremental response yields the noise capacitance value $C_n^{rms} = 0.065\ fF$, which is significantly lower than the published C8051F990 MCU minimum detectable capacitance change of 1 fF [Sil11]. This means the dominant noise source is the MCU. Therefore, pressure resolution of an ELM-hydrophone system is the pressure associated with a capacitance change of 1 fF.

Hydrophone chip integration with the ELM printed circuit board takes special care due to limitations set by the PCB. The chip must be deposited on the PCB with diaphragms facing

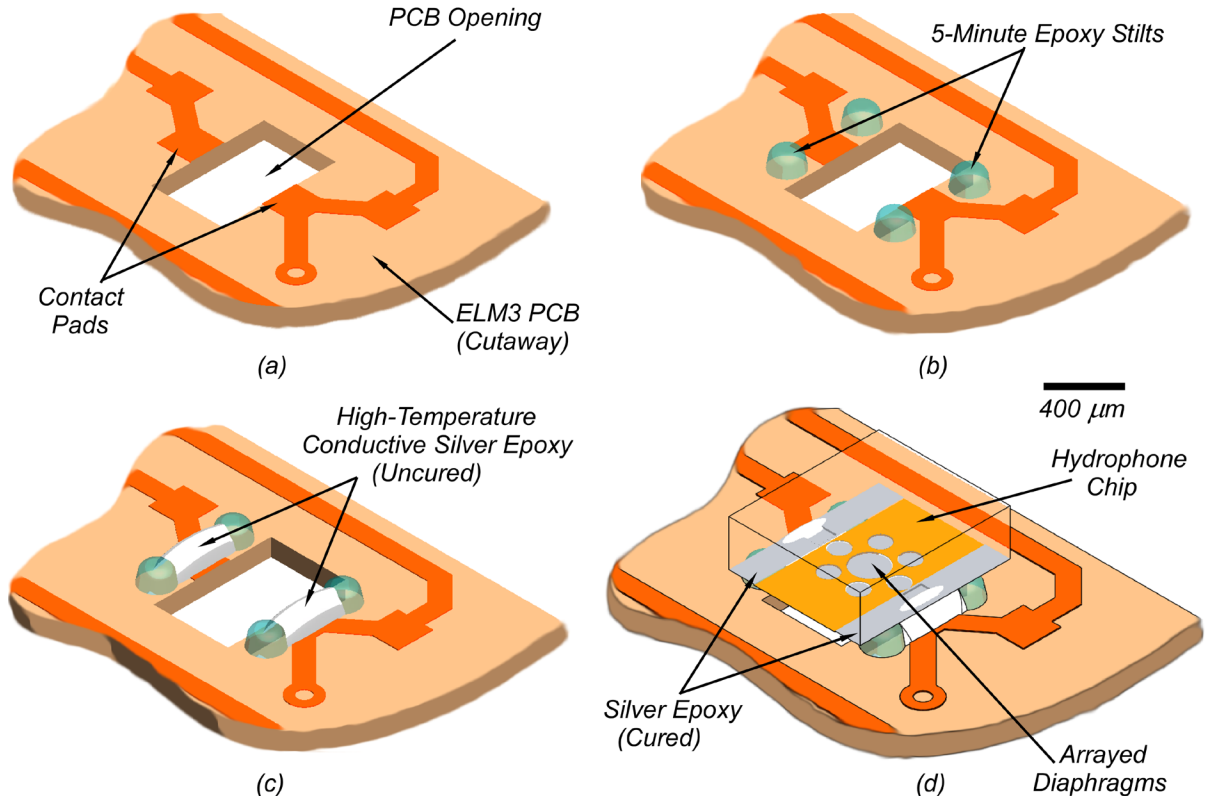

Fig. 3. 9: Hydrophone-ELM integration procedure. (a) The bare PCB is cleared of any debris. (b) 5-Minute Epoxy is used to make four chip "stilts". (c) Silver epoxy is placed over the ELM contact pads. The epoxy is not allowed to cure until the chip is integrated. (d) The hydrophone chip with cured, pre-applied silver epoxy is placed on top of the stilts. The silver epoxy is then allowed to cure at room temperature.

downward through a laser micromachined hole in the PCB. This hole allows pressure transfer to the diaphragms, even when the PCB is folded as shown in Fig. 3. 1(a). To ensure free movement of diaphragms, a custom chip integration procedure was developed that includes epoxy "stilts" that keep the diaphragms lifted and out of contact with the PCB. This procedure is depicted in Fig. 3. 9. To aid with electrical connections, the hydrophone chip, shown in Fig. 3. 10, is prepared for integration by applying a thin layer of Duralco™ 120 silver conductive epoxy over the edges of the chip. The contact pads are completely covered. The epoxy is fully cured before integration with the ELM system. Pre-application of the epoxy is done because the silver epoxy easily adheres to itself, whereas adhesion to the chip contact pads requires more effort that cannot be afforded.

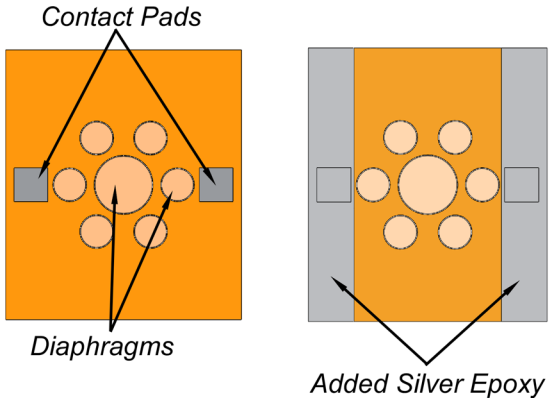

Fig. 3. 10: Chip preparation procedure. Contact pads are coated by hand with a layer of silver conducting epoxy. The epoxy layer is made significantly larger than the pads to ensure excellent electrical connection with the PCB. Epoxy is cured before integration.

Once chip preparation is complete, the PCB is cleaned and cleared of any debris around the PCB contact pads as shown in Fig. 3. 10(a). Next, four epoxy stilts are added at each corner of the PCB opening, as seen in (b), using Devcon™ 5 Minute Epoxy. Each stilt is approximately 1 mm in diameter and 0.5 mm in height. When the stilts are cured, silver conductive epoxy is applied over the contact pads and between the stilts (c). Before the epoxy can cure, the prepared chip is carefully placed in position as shown in (d). The wet epoxy easily wicks onto the chip.

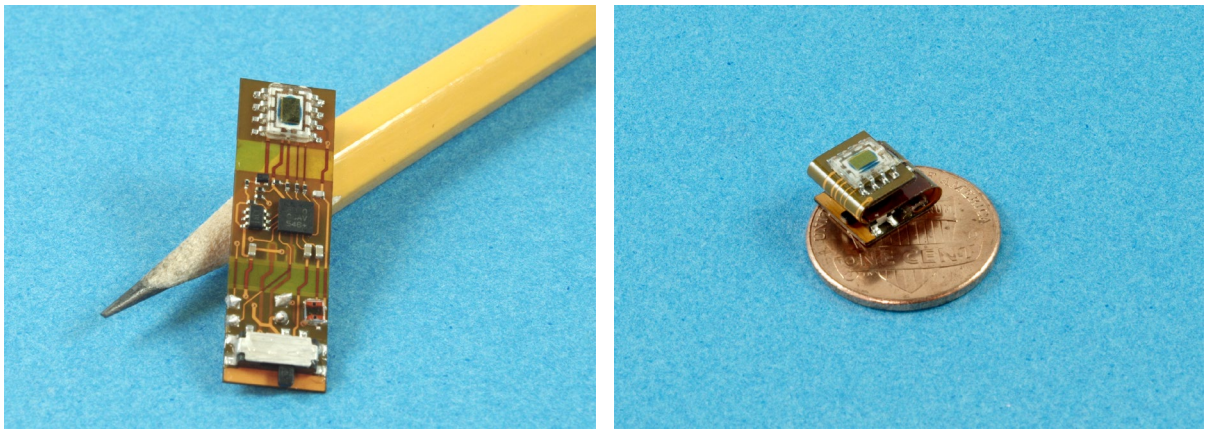

(a) (b)

Fig. 3. 11: ELM system with integrated heterogeneous hydrophone. (a) Unfolded system. The chip is near the bottom right corner of the PCB. (b) Folded system. The chip is better protected from abrasion; a folded system is also effectively smaller, which facilitates testing.

Fig. 3. 11 shows an ELM system with an integrated heterogeneous hydrophone in (a) unfolded configuration and (b) folded configuration. Testing is conducted using only a folded PCB; this minimizes the effective size of the system and provides added protection to the integrated sensor. Systems are tested in non-conductive hydraulic oil, which allows for the systems to remain unpackaged (as shown).

3.5 Experimental Methods

The desired static pressure and seismic acoustic data was obtained using a single test setup pictured in Fig. 3. 12(a). The setup consists of a pressure vessel, to which a manual hydraulic pump, hydrophone housing, commercial pressure transducer, and a plate housing are attached. This setup can generate acoustic shock waves as large as 100 psi in magnitude at any static pressure up to 50 MPa. The hydrophone housing is a custom machined part that includes a cylindrical bore in which the device under test (DUT) is located. The plate housing holds a round disc, or plate, that is deflected by a piezoelectric stack actuator (Piezosystem Jena Pst 1000/16/100) that creates the acoustic waves of interest. A Measurement Specialties M5241 pressure transducer is used as a reference. The transducer is used for static pressure measurements as well as acoustic measurements up to 100 Hz in frequency. The manual hydraulic pump (Enerpac^{TM} P142) provides change in static pressure. Enerpac^{TM} LX101 99% paraffin oil is used as the fluid medium. An optical picture of the test setup is found in Fig. 3. 13.

A block diagram of the testing setup is shown in Fig. 3. 14. An electrical signal of the desired frequency is applied to a Viking Industrial Products VP7250 driver using an Agilent 33210A function generator. The driver is a DC-DC switch that only supports square wave

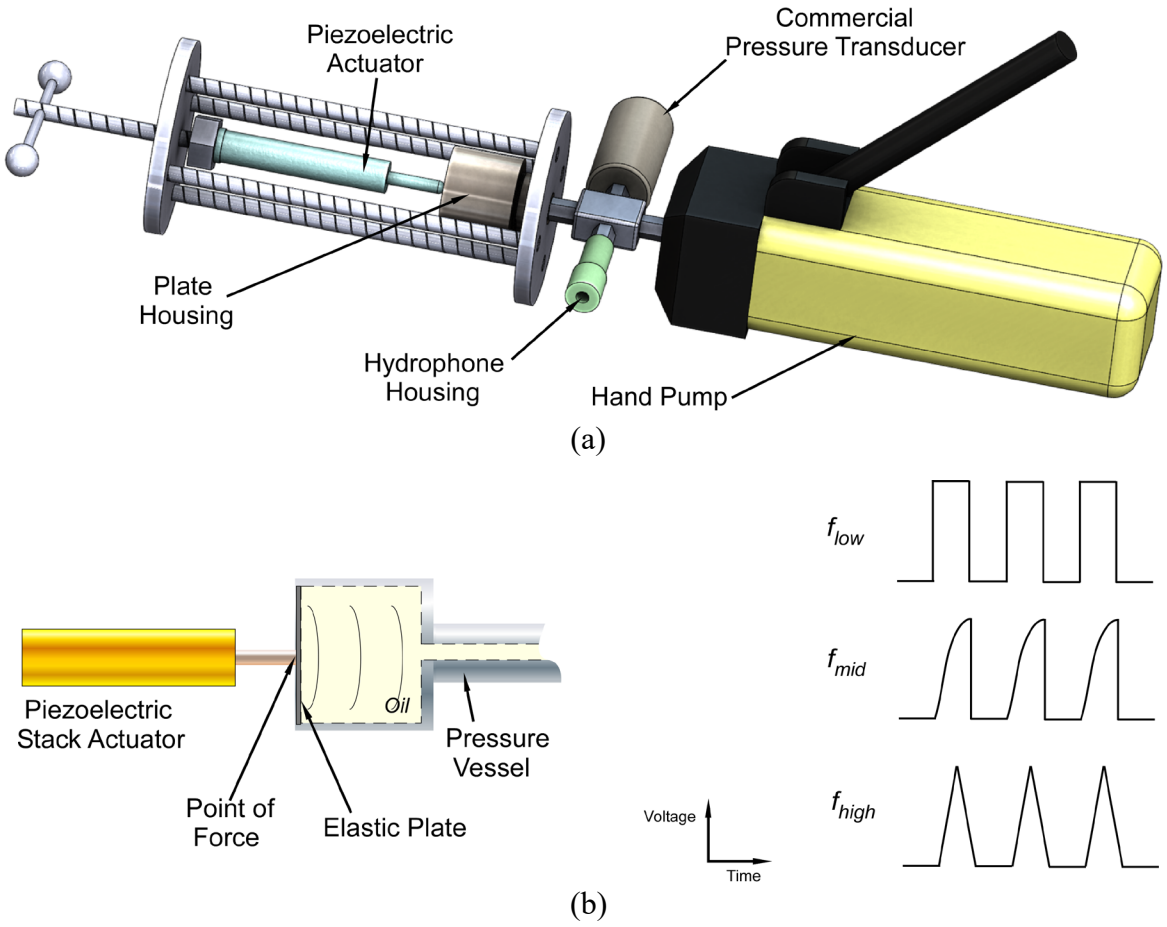

Fig. 3. 12: CAD representation of the high pressure acoustic setup used for testing ELM-hydrophone systems. (a) Overall view of the test setup. (b) A piezoelectric stack actuator generates acoustic waves. Electrical current limitations of the driver result in frequency dependent voltage profiles over the stack, which are manifested in the generated acoustic signals.

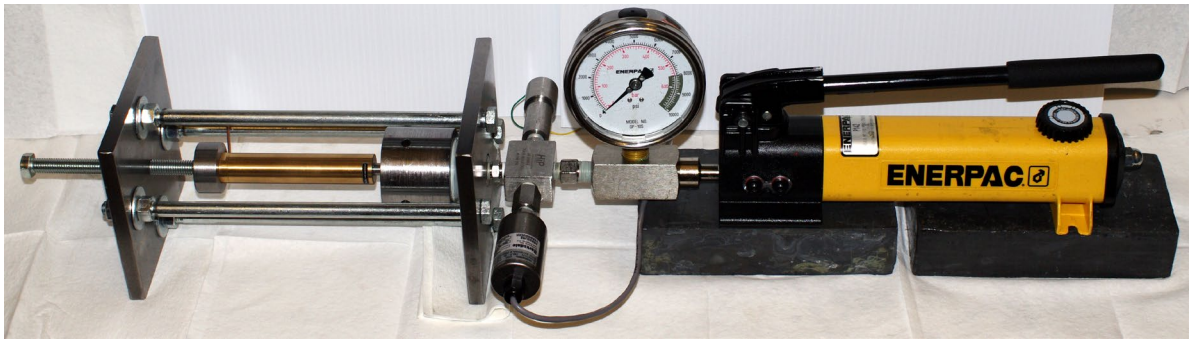

Fig. 3. 13: Optical image of the high pressure acoustic test setup.

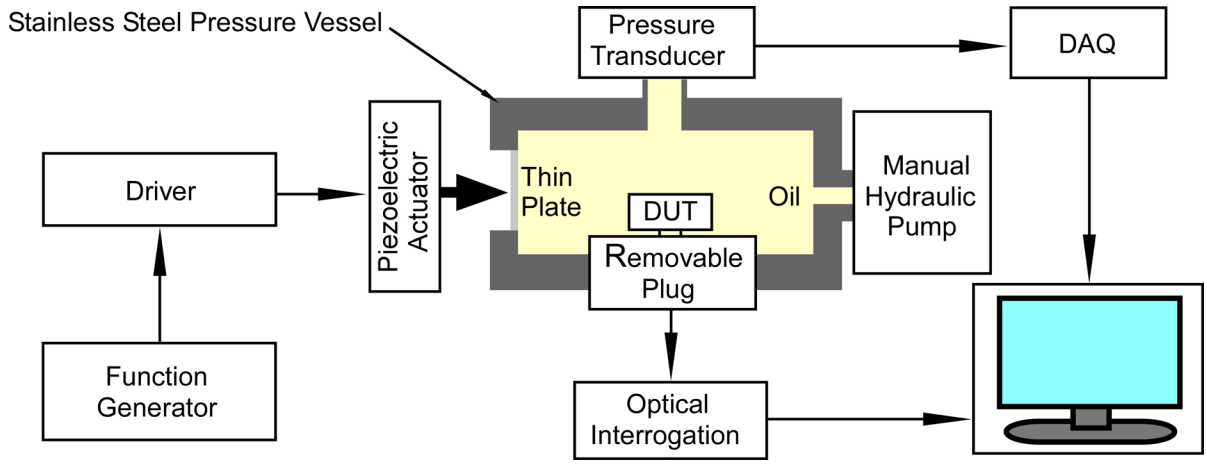

Fig. 3. 14: Block diagram of the testing setup. For acoustic testing, a function generator and driver operate the piezoelectric actuator to create acoustic waves inside the pressure vessel at different static pressures. Reference data is collected using a DAQ and computer interface.

signals. The driver is connected to the piezoelectric stack actuator and charges the stack up to $700V_{pp}$ at frequencies up to 100 Hz. Reference pressure readings are measured using a National Instruments™ USB-6211 data acquisition card (DAQ) and LabVIEW™ 2011 SP1. During testing, the ELM system is put into Detection State and sealed inside the hydrophone housing. Once the ELM data is collected, the vessel is pumped back down to atmospheric pressure and the ELM is interrogated optically using a custom readout box.

The acoustic signal generated by the stack actuator is up to 100 psi in magnitude and no more than 100 Hz. The frequency limit is chosen based on typical frequency bands used in applications to oil and gas exploration. The wavelength of these signals is extremely large (14 m at 100 Hz) compared to the test setup, resulting in uniform pressure distribution throughout the pressure vessel. Furthermore, the small vessel dimensions result in propagation of only planar radial profiles. The magnitude of the complex acoustic signal, $\boldsymbol{p}$, is equal to

$$|\boldsymbol{p}| = |\boldsymbol{\alpha}| U_0 \rho c + |\boldsymbol{\beta}| \frac{K \Delta V}{V}, \tag{3.2}$$

where U_0 is the resultant velocity magnitude of the plate, ρ is fluid density, c is speed of sound, K is bulk modulus, V is pressure vessel volume, and $\boldsymbol{\alpha}$ and $\boldsymbol{\beta}$ are appropriate complex constants. The first term in equation 3.2 is from the radiation impedance of the plate into the fluid, while the second term is from changes in pressure due to changes in volume of the pressure vessel. Due to low frequency and use of a reference transducer, further analysis was not performed for ELM testing; however, in depth analysis of the setup can be found in Chapter 4.

3.6 Experimental Results

All data from Section 3.6 was obtained from a single ELM – hydrophone system, which is referred to as ELM – hydrophone system 1.

3.6.1 ELM – Hydrophone Static Pressure Response

The static pressure response from ELM – hydrophone system 1 is shown in Fig. 3. 15. The curve shows very similar shape to those documented in Chapter 2. The response at low static pressure is high, then drops quadratically. This particular sensor appears to have a larger

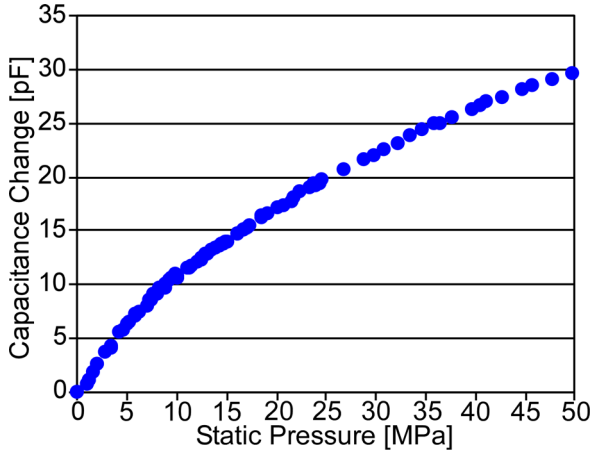

Fig. 3. 15: ELM – hydrophone system 1 experimental static pressure response.

diaphragm deflections than other devices, resulting in this undesired quadratic response. The total capacitance change is under 30 pF, which is notably lower than other sensors.

The minimum detectable static pressure, also known as pressure resolution, is shown in Fig. 3. 16. This plot is obtained by dividing the MCU minimum resolvable capacitance change, ΔC_{min}, by the incremental response R, which is defined as the approximate slope ($\Delta C/\Delta P$) of the curve in Fig. 3. 15:

$$\Delta P_{res} = \frac{\Delta C_{min}}{R} = \frac{1\ fF}{\Delta C/_{\Delta P}} \tag{3.3}$$

C is capacitance change and P is static pressure. The curve in Fig. 3. 16 reveals an extremely high resolution (low pressure value), which agrees with the observations made regarding Fig. 3. 15. The large pressure response at low static pressure leads to high incremental response, which, according to equation 3.3, reduces the minimum resolvable static pressure. The resolution is approximately 0.1 psi (689 Pa) at atmospheric static pressure and increases almost linearly to a value of approximately 0.6 psi (4,135 Pa) at 45 MPa static pressure.

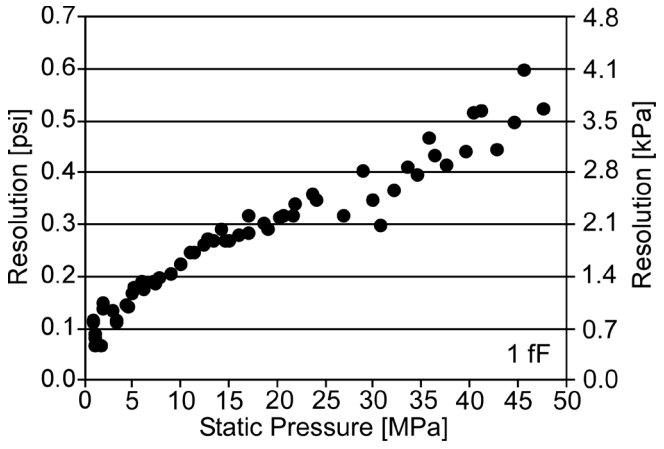

Fig. 3. 16: ELM – hydrophone system 1 experimental static pressure resolution. The MCU minimum detectable capacitance change of 1 fF is used to calculate pressure resolution.

3.6.2 Frequency Response

The ELM – hydrophone incremental response at different frequencies, referred to as the frequency response, is of great interest to this work. The frequency response was tested up to 50 Hz, which was chosen to be one quarter of the programmed 200 S/s sampling rate. This is not the maximum bandwidth, as is discussed in Section

The bandwidth of each sensor is significantly larger than 50 Hz (see Section 2.5), so the incremental response in this band is not expected to have any effect from frequency. Frequency response at any static pressure is obtained by dividing the ELM's measured peak to peak (p-p) capacitance change by the reference transducer's measured peak to peak pressure change. Examples of such measurements are shown in Fig. 3. 17. The ELM capacitance measurement in (a) reveals a square wave acoustic signal. The reference transducer response in (b) agrees with the ELM. The shape of the acoustic signal is dependent on the voltage profile over the stack actuator, which is dependent on the frequency of signal provided by the function generator. The

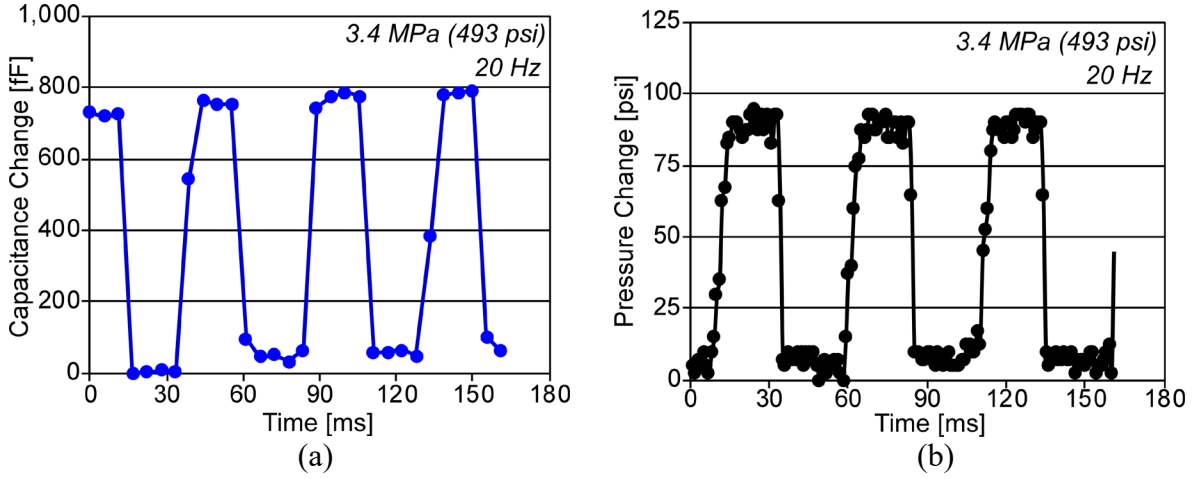

Fig. 3. 17: Typical response (asynchronous) used for experimental incremental response measurements. These measurements were taken at about 3.4 MPa static pressure and 20 Hz signal. (a) ELM – hydrophone system 1 capacitance response of a 20 Hz acoustic signal. Incremental response is calculated by dividing the peak to peak magnitude of the capacitance wave to the peak to peak pressure measurement from the reference transducer in (b). The reference transducer and ELM system are not synchronized.

three voltage/pressure profiles encountered in this work are depicted in Fig. 3. 12. The incremental response is calculated as

$$R(f,P) = \frac{C_{p-p}}{P_{p-p}} = \frac{C_H(f,P) - C_L(f,P)}{P_H(f,P) - P_L(f,P)}, \tag{3.4}$$

where f is frequency, P is static pressure, C_H and C_L are high and low capacitance change values, respectively, and P_H and P_L are high and low pressure change values, respectively. When possible, such as in the case of square waves, the high and low capacitance and pressure values are taken as averages. This is not possible in every situation. It is important to note, however, that the uncertainty provided by random value fluctuation is inconsequential when compared to peak to peak values.

The experimental frequency response of the ELM – hydrophone system 1 can be found in Fig. 3. 18. Three curves are shown, each representing a frequency response at a different static pressure. As expected, the frequency response is unaffected by frequency in this band. The value for 0 Hz was taken from the incremental response calculations in Section 3.6. The units used are dB reference to (1 fF/μpsi)^2, which can also be expressed as

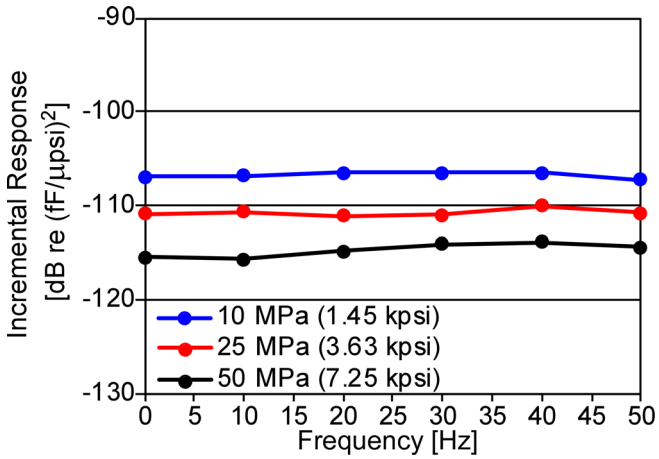

Fig. 3. 18: Experimental ELM – hydrophone system 1 incremental response vs. frequency at three different static pressures. Results show no dependence on frequency in the bandwidth of interest. Incremental response only changes with static pressure. The maximum variation of +/-0.9 dB occurs at 50 MPa.

$$dB\ re\ \left(\frac{fF}{\mu psi}\right)^2 = 10\log_{10}\left[\frac{R}{1\ fF/\mu psi}\right]^2 = 20\log_{10}\left[\frac{R}{1\ fF/\mu psi}\right] . \qquad (3.5)$$

The slight variation in incremental response is a maximum of +/- 0.9 dB at 50 MPa static pressure and is due to several factors including asynchronization between the reference transducer and ELM, as well as random variations in measurements that could not be averaged. Regardless, +/-0.9 dB variation is considered very low and is acceptable for this work.

3.6.3 Incremental Response Change with Static Pressure

Results in Fig. 3. 18 show that the frequency response is only affected by static pressure, which begs for a full characterization of the incremental response as a function of static pressure. This was performed by repeating the preceding procedure and calculation at a single frequency but many different static pressure levels. Results from this test are shown in Fig. 3. 19. As expected, the incremental response is extremely high at low static pressures. The incremental response quickly drops from a maximum of -96.2 dB at 1.67 MPa (16.5 atm) down to -105.9 dB

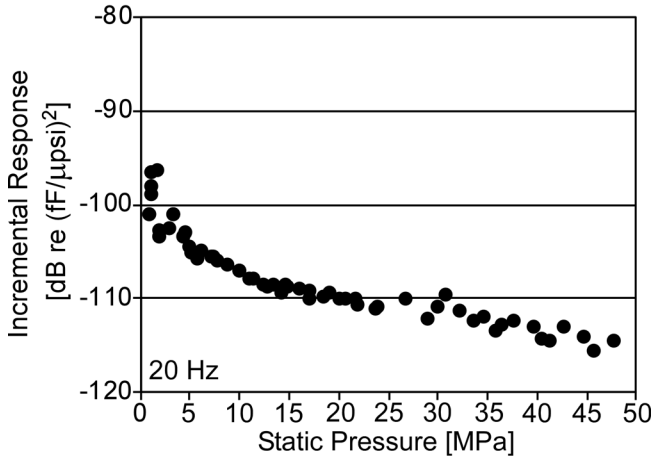

Fig. 3. 19: Experimental ELM – hydrophone system 1 incremental response vs. static pressure. The curve has shape identical to the inverse of the resolution curve in Fig. 3. 16 expressed in dB.

at 7.92 MPa (78.2 atm). The incremental response then drops to -115.5 dB at 47.2 MPa (466 atm).

3.6.4 Noise and Minimum Detectable Acoustic Pressure

The static pressure resolution corresponds to a minimum detectable capacitance change that the MCU is capable of measuring [Cha87b, Sil11]; this is discussed in Section 3.4. A fast Fourier transform (FFT) was performed on resting capacitance data collected over 12 measurement cycles at STP conditions. Experimental capacitance noise vs. frequency can be found in Fig. 3. 20(a). The plot shows significantly reduced noise as frequency increases. The noise value above 2 Hz holds at a low level throughout the remainder of the bandwidth of interest. The minimum detectable pressure (MDP) at the three static pressures is calculated and plotted in Fig. 3. 20(b). According to the datasheet [Sil11], the minimum resolvable capacitance is unchanged for baseline capacitances up to 45 pF. The heterogeneous hydrophone remains

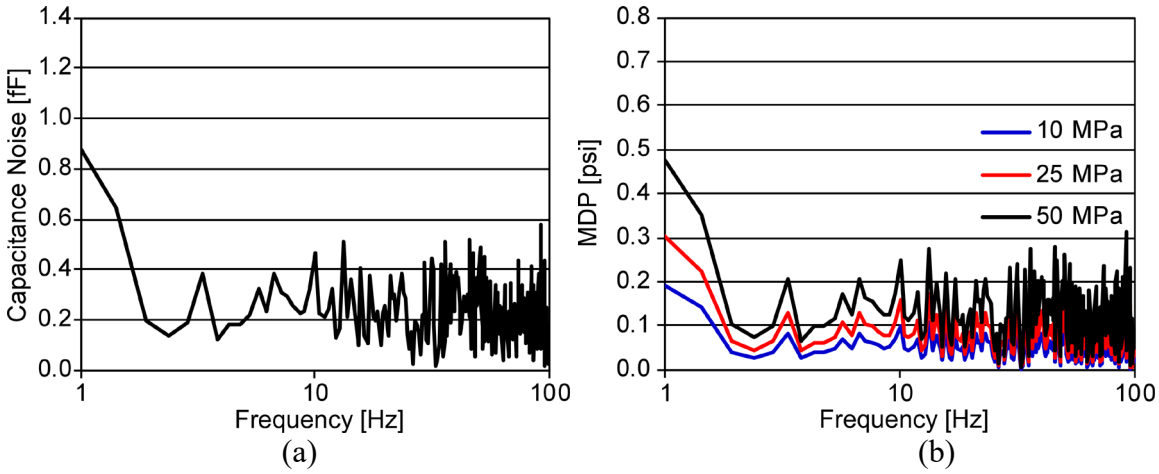

Fig. 3. 20: Frequency components of the resting capacitance measurement from ELM – hydrophone system 1. The 0 Hz component, corresponding to the sensor baseline capacitance, is omitted. (a) Capacitance noise vs. frequency. (b) Minimum detectable pressure (MDP) vs. frequency. MDP is calculated by dividing the capacitance at each frequency in (a) by the incremental response at each static pressure.

Table 3. 9: Tabulated values of interest from Fig. 3. 20(b).

Static Pressure	Average MDP (1.9 Hz – 99.5 Hz)
10 MPa	0.05 psi (344 Pa)
25 MPa	0.08 psi (551 Pa)
50 MPa	0.13 psi (896 Pa)

below 45 pF throughout the static pressure range, which means the data in Fig. 3. 20(a) can be assumed to be unchanged with baseline capacitance. The data at three different static pressure values in (b) are therefore be calculated by dividing the capacitance values in (a) by the incremental response at each static pressure. Some values of interest from this calculation are tabulated in Table 3. 2.

3.6.5 Usable Bandwidth

Preceding data was collected using a sampling frequency of 200 S/s, which was used to measure acoustic data up to 50 Hz. By the Nyquist rate, this sampling frequency could be used to identify signals as high as 100 Hz, although they may not be accurate values for acoustic wave magnitude. Seismic applications typically call for frequencies below 100 Hz, which defines this

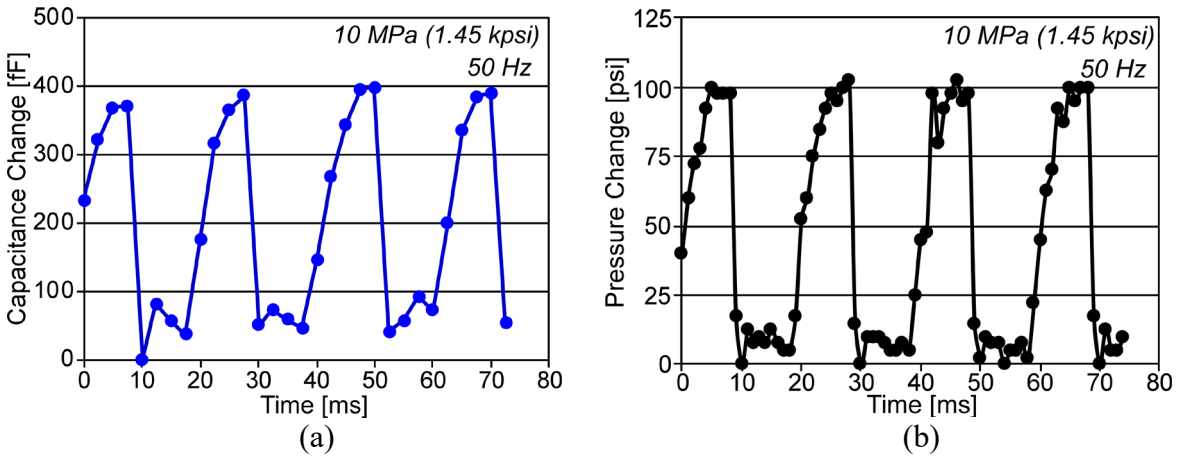

Fig. 3. 21: Data collected from a 50 Hz acoustic signal with an ELM sampling frequency of approximately 375 S/s. (a) Capacitance data collected from ELM – hydrophone system 2. (b) Asynchronous pressure data from the reference transducer.

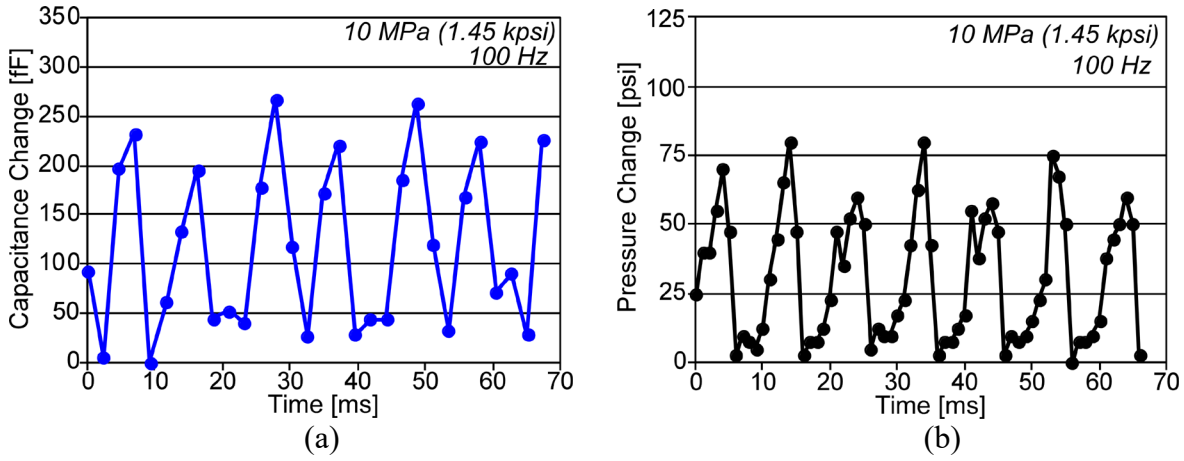

Fig. 3. 22: Data collected from a 100 Hz acoustic signal with an ELM sampling frequency of approximately 430 S/s. (a) Capacitance data collected from ELM – hydrophone system 2. (b) Asynchronous pressure data from the reference transducer.

work's frequency band of interest. Although preceding data is only up to 50 Hz acoustic signals, a separate ELM system (ELM – hydrophone system 2) was used to demonstrate collection of data at higher frequencies.

Acoustic measurements of 50 Hz and 100 Hz are shown in Fig. 3. 21 and Fig. 3. 22, respectively. Both plots were produced using ELM – hydrophone system 2. The 50 Hz signal was collected with a sampling rate of approximately 375 S/s. The curve in Fig. 3. 21(a) shows the capacitance change data as a function of time, while (b) shows the asynchronously measured pressure as a function of time. Both curves show a modified pressure profile, consistent with the voltage applied over the stack. The 100 Hz signal in Fig. 3. 22 was collected with a sampling rate of approximately 430 S/s. The change in sampling rate is due to slight variations in system clock frequency, which changes from system to system. The capacitance profile closely matches the pressure profile in (b); although the measurement looks somewhat jagged, it is an accurate representation of the true acoustic profile present in the pressure vessel. The data in Fig. 3. 21 and Fig. 3. 22 demonstrate that the system can easily be used for seismic sensing applications.

The maximum useable bandwidth of a hydrophone – ELM system is dependent on the size of the ELM, the intended use, the sampling frequency, as well as the amount of available flash memory. The C8051F990's maximum sampling frequency was verified to be over 30 kS/s, which corresponds to capacitance conversion times within the published values of 26 and 50 μs [Sil11]. This sampling frequency could be used to acknowledge acoustic signals as high as 15 kHz but could not produce a smooth curve. Increasing the sampling rate also reduces the low end bandwidth because only a limited number of data points can be measured per measurement cycle. This factor is limited by available flash memory. To obtain accurate measurements at elevated frequency, 1) the acoustic signal should have a wavelength that is much larger than the ELM maximum feature size, 2) the data sampling rate should be at least above the Nyquist rate, and 3) the total sampling time per measurement cycle must be larger than at least one period of the acoustic signal. Assuming an ELM maximum feature size of 8 mm, the frequency corresponding to 80 mm wavelength in seawater at 25°C (c = 1531 m/s [Sel85]) is 19.1 kHz. This frequency is higher than the Nyquist rate; therefore, the useable system bandwidth is limited by the Nyquist rate to approximately 15 kHz.

3.7 Discussion and Summary

The environmental logging microsystem (ELM) is built using commercial off the shelf electronic components, custom pressure sensors and hydrophones, and lithium-based batteries all integrated on a foldable PCB. This work presents the integration and successful testing of a hydrophone sensor that is capable of high incremental response for acoustic purposes over a large range of static pressure. Experimental results show a static pressure response up to 50 MPa as well as full functionality at frequency. Data was collected at up to 100 Hz acoustic signal,

which compared extremely well to that of a reference transducer. The change in incremental response with applied static pressure was fully characterized, as well as the MDP and frequency response at increasing static pressure.

The heterogeneous hydrophone is a complete response to the unanswered call for a micro hydrophone that is: 1) on or below the order of 1 mm^3, 2) can withstand static pressures up to 50 MPa, 3) provides sufficient incremental response for sub-psi resolution for all static pressures up to 50 MPa, 4) can reliably be used to measure seismic waves 100 psi (689 kPa) in magnitude or larger, 5) utilizes one or more sensing elements that is completely sealed from the environment, 6) can easily withstand stresses associated with curing of encapsulating epoxies, and 7) provides a static pressure response. These requirements are defined from considerations of autonomous microsystems for use in oil and gas exploration. Existing hydrophone technology typically involves bulky sensors that require some sort of pressure balancing; these hydrophones are not compatible with microsystems such as the ELM. The heterogenous hydrophone enables seismic sensing in autonomous microsystems, which is not possible with other hydrophones.

Chapter 4: Implementation as an Ultrasonic Transducer

The focus of Chapter 4 is to explore the application of the H106 heterogeneous array to use as an ultrasonic transducer as well as a deep-sea hydrophone. This was accomplished by integrating the hydrophone with a charge amplifier circuit, which was assembled on a printed circuit board. The chapter begins with a short background of possible readout circuits and explains the choice of circuit design. The implemented charge amplifier circuit design and simulation is described. Next, an equivalent electroacoustic model is presented for lumped element modeling of the hydrophone-circuit device. Experimental methods are described in depth before characterization results are presented. Lastly, results are benchmarked with both industrial and academic hydrophones.

4.1 Readout

Use as an ultrasonic transducer requires interface circuitry that can resolve sub-Pascal acoustic pressures as well as provide bandwidth into the MHz region. Accordingly, it is not practical to use a CDC for such readout. There are two common configurations for readout of capacitive acoustic sensors: constant charge readout and constant voltage readout. Use of one configuration over the other is dependent on the nature of the sensor. Constant voltage readout is used in this work for the reasons described in this section.

4.1.1 Constant Charge Readout

Constant charge readout [Sch94] involves biasing the sensor through a large resistor and measuring the change in voltage with respect to sensor capacitance. Charge over the sensor is kept constant, as its name implies. The configuration is shown in Fig. 4. 1: Constant charge readout. A bias voltage is applied to the sensor through a biasing resistor. As the sensor capacitance changes, so does the voltage over the sensor, which is buffered to the output.. The baseline capacitance of the sensor, C_0, changes by the amount ΔC due to incoming acoustic pressure. Using the relationship $Q = CV$, the voltage change cause by this change in capacitance is derived from the following:

$$\Delta V = \frac{Q}{C_0 + \Delta C} - \frac{Q}{C_0} = \frac{C_0 V_B}{C_0 + \Delta C} - \frac{C_0 V_B}{C_0} = -V_B \frac{\Delta C}{C_0 + \Delta C}. \tag{4.1}$$

By including the buffer input capacitance, C_i, and parasitic capacitance, C_{par}, as well as the consideration that $\Delta C << C_0$, equation 4.1 can be rewritten as

$$\frac{\Delta V}{\Delta C} \approx -\frac{1}{C_0 + C_{par} + C_i} V_B . \tag{4.2}$$

Finally, constant charge sensitivity is described as

$$S_{CQ} \equiv \frac{\Delta V}{\Delta P} = \frac{\Delta V}{\Delta C}\frac{\Delta C}{\Delta P} = -\frac{V_B}{C_0 + C_{par} + C_i}\frac{\Delta C}{\Delta P}, \tag{4.3}$$

where the quantity $\frac{\Delta C}{\Delta P}$ is the sensor's pressure incremental response in units of F/Pa. Buffer gain is assumed to be unity. Charge is kept constant over the sensor by making R_B, the biasing resistor, large as well as the input impedance to the buffer. The RC circuit formed by the sensor and bias resistor effectively creates a high-pass filter, with a corner frequency described by equation 4.4, where C_{tot} includes sensor baseline, parasitic capacitance, and buffer input capacitance.

$$f_c = \frac{1}{2\pi R_B C_{tot}} \tag{4.4}$$

Constant charge voltage readout is not favored for this work for two reasons. The first reason is the inverse proportionality between sensitivity and sensor baseline capacitance. The heterogeneous hydrophone has a static pressure response, which is preferred for use in downhole microsystems. However, as static pressure and therefore baseline capacitance increases, the sensitivity of the hydrophone would continuously diminish, regardless of the linearity of the static response. This is not desired because the sensitivity should be constant. The second reason is that this configuration is not compatible with an arrayed architecture such as that employed in the heterogeneous array. For example, say one sensing element has a baseline C_0 and pressure incremental response $\frac{\Delta C}{\Delta P} = pr$. Using equation 4.3, the sensitivity is proportional to pr/C_0. Now, if a second sensing element is added in parallel, the sensitivity is proportional to $2pr/2C_0$. This increases the numerator and the denominator by the same factor, which clearly makes arraying to be fruitless and constant charge readout to be inapplicable to this work.

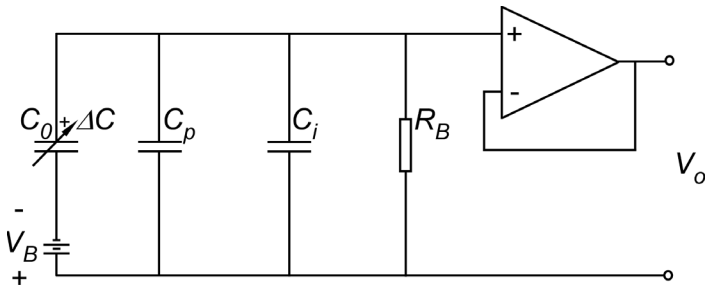

Fig. 4. 1: Constant charge readout. A bias voltage is applied to the sensor through a biasing resistor. As the sensor capacitance changes, so does the voltage over the sensor, which is buffered to the output.

4.1.2 Constant Voltage Readout

Constant voltage readout [Mar07a, Mar07b] can be utilized in a charge amplifier configuration, as shown in Fig. 4. 2. In this setup, a bias is applied over the sensor once again

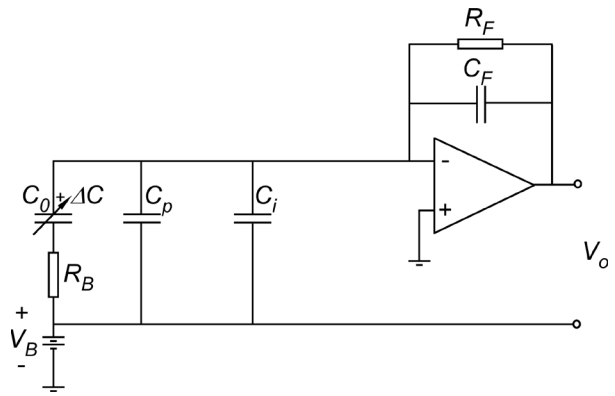

Fig. 4. 2: Constant voltage readout circuit. A bias is applied to the sensor through resistor, to limit transient current as well as to discourage crosstalk with the bias source. Charge is integrated over the feedback capacitor, C_F, which produces a voltage at the op amp's output.

through a biasing resistor. This resistor limits transient current, as well as reduces crosstalk with the bias source. The voltage at the sensor's second terminal is connected to the inverting op amp input, which keeps the DC potential at ground and therefore the voltage over the sensor constant. Parasitic capacitances and any input capacitance are also included in the schematic. Once again starting with the canonical $Q = CV$ relationship, the amount of charge generated by acoustic pressure is described by the following:

$$\Delta Q = V_B \frac{\Delta C}{\Delta P} \Delta P \,, \tag{4.5}$$

where ΔP is acoustic pressure. This charge is generated rapidly, and is integrated over the feedback capacitor, C_F, to produce the following equation:

$$\frac{\Delta V}{\Delta Q} = -\frac{j\omega R_F}{1 + j\omega R_F C_F} \,. \tag{4.6}$$

With a large feedback resistor, R_F, the charge will not have time to flow through the feedback resistor but instead collect over C_F. As frequency increases, equation 4.6 reduces to

$$\frac{\Delta V}{\Delta Q} = -\frac{1}{C_F} \,. \tag{4.7}$$

Now, the acoustic sensitivity can be written as

$$S_{CV} \equiv \frac{\Delta V}{\Delta P} = \frac{\Delta V}{\Delta Q}\frac{\Delta Q}{\Delta P} = -\frac{V_B}{C_F}\frac{\Delta C}{\Delta P}. \tag{4.8}$$

Like the constant charge case, this configuration creates a high pass filter:

$$f_c = \frac{1}{2\pi R_F C_F}. \tag{4.9}$$

The suitability for the constant voltage readout method to be used in this work comes from the relationship between sensitivity and baseline capacitance, C_0: there is no relationship between the sensitivity and baseline capacitance. This is critical for the heterogeneous hydrophone because it is sensitive to static pressure, and the baseline is designed to increase with increasing water depth. This does come with a design tradeoff, though, as increasing the ratio between C_{tot} and C_F has an impact on noise at the charge amplifier's output.

The output noise of the charge amplifier can be solved for analytically using superposition. Fig. 4. 3 depicts a noise model for the circuit. Each noise contribution is expressed as either an RMS noise voltage or current. There are three sources of noise in this circuit: the input impedance Z_i, feedback loop impedance Z_F, and noise from the op amp. The input and feedback loop impedances are described as

$$Z_i = \frac{1}{j\omega C_{tot}} + R_B \tag{4.10}$$

$$Z_F = \frac{R_F}{1 + j\omega C_F R_F}. \tag{4.11}$$

Op amp noise is modeled in Fig. 4. 3 by voltage and noise sources V^2_{na} and I^2_{na}. Input impedance noise is modeled by voltage source V^2_{ni} and feedback impedance noise is modeled by current source I^2_{nF}. Superposition of the output power spectral density (PSD) due to each noise source takes the form

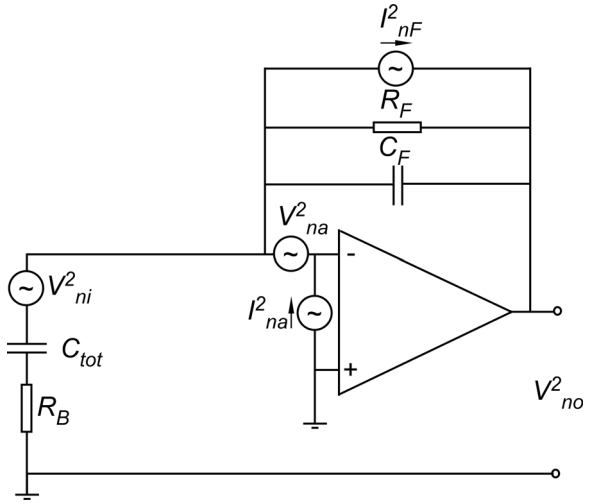

Fig. 4. 3: Noise model of a charge amplifier circuit. The contribution from each source to the voltage at the output is superposed to describe the circuit noise performance.

$$V_{no}^2 = (V_{ni}^2 + V_{na}^2)\left|1 + \frac{Z_F}{Z_i}\right|^2 + (I_{nF}^2 + I_{na}^2)|Z_F|^2 . \tag{4.12}$$

As frequency increases above $1/2\pi R_F C_F$, this can be further expressed as

$$V_{no}^2 = (V_{ni}^2 + V_{na}^2)\left|1 + \frac{C_{tot}}{C_F}\right|^2 + (I_{nF}^2 + I_{na}^2)\left|\frac{1}{j\omega C_F}\right|^2 . \tag{4.13}$$

Equation 4.13 clearly shows that as the pressure increases, the noise at the output will also increase by the ratio of C_{tot} to C_F. The dominant noise source to be affected by this term is from the op amp, which is specified to have 6.6 nV/√Hz noise at 10 kHz [Ana19].

4.1.3 Charge Amplifier Circuit

A schematic of the implemented charge amplifier is shown in Fig. 4. 4. The component values shown were used for acoustic testing; they can easily be replaced depending on application specific needs. The value for feedback capacitor was chosen to be 1 pF, which provides 1V output voltage per pico-Coulomb produced by the hydrophone sensor. A smaller feedback capacitor was not chosen because 1) this hurts the low frequency response of the

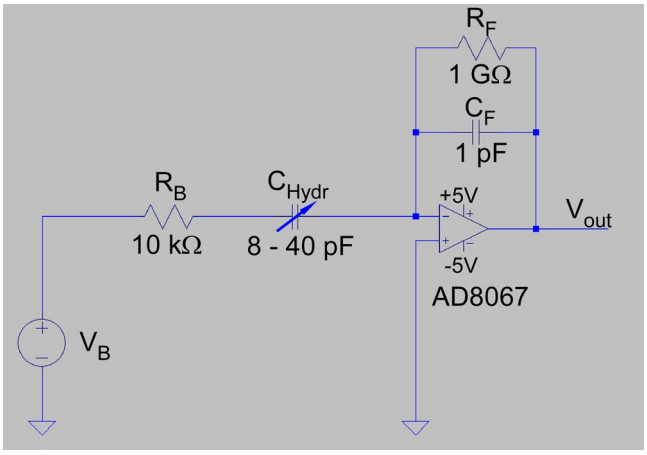

Fig. 4. 4: Charge amplifier schematic developed in LTSpice®XVII.

hydrophone, and 2) output noise would suffer. A relatively high value of 1 GΩ was chosen for the feedback resistor in order to maintain reasonable low frequency response as well as reduce current noise above the low frequency cutoff. The corner frequency of the charge amplifier's high pass filter is 159 Hz in this configuration. An Analog Devices, Inc., AD8067 operational amplifier was chosen due to its extremely high input impedance, low noise characteristics, wide bandwidth, and low cost.

Circuit simulations were performed in LTSpice®XVII. The bias voltage in Fig. 4. 4 was replaced by an AC voltage source, which was driven through a 1 pF capacitor to create an input

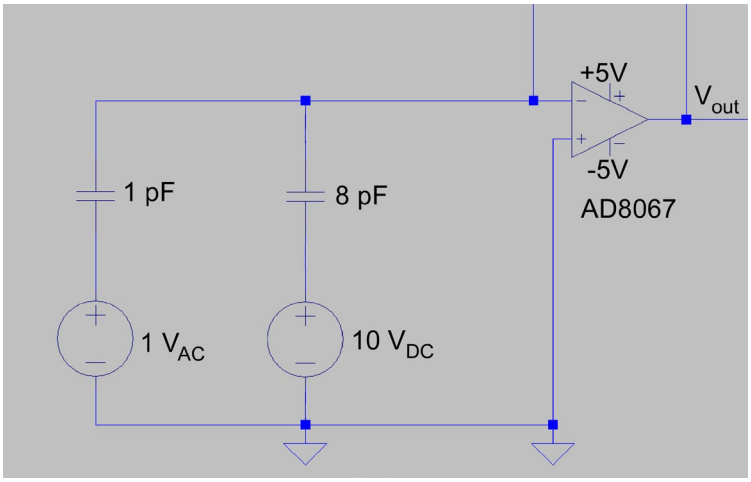

Fig. 4. 5: Circuit configuration for the input signal used in gain simulations. A 1 pF capacitor is driven by a 1V AC signal source, which creates a 1 pF input signal to the charge amplifier. The signal is put in parallel with the baseline capacitance of the sensor.

signal of 1 pico-Coulomb. Please see Fig. 4. 5 for reference. The input signal is placed in parallel with a baseline capacitor to mimic how the circuit will be implemented. The baseline capacitor is biased at 10V DC. The baseline capacitor does not influence gain, but it does influence noise performance.

Simulation results are shown in Fig. 4. 6. Parametric sweeps were performed on the feedback resistor and capacitor to illustrate each component's impact on circuit performance. Fig. 4. 6(a) shows results for the feedback resistor. As expected from equation 4.9, the corner frequency of the high pass filter decreases in value with increasing R_F. Gain is unaffected, as well as performance at high frequency. High frequency gain is dictated by the operational amplifier, which has a specified gain-bandwidth product of 540 MHz [Ana19]. The phase at low frequency is changed because the change in R_F changes the transfer function at low frequency. High frequency phase is unchanged because only the feedback capacitor and op amp dictate the high frequency bandwidth. Fig. 4. 6(b) shows results for the feedback capacitor. The feedback capacitor affects both gain and bandwidth. The plot clearly shows the high pass filter's corner frequency decreasing with increased feedback capacitance. The gain below the corner frequency on all three curves converge because the gain is proportional to ωR_F, which is identical for all three. A decrease in feedback capacitor also allows for higher frequency operation, which follows the gain-bandwidth product of the op amp. There is an instability with 10 pF feedback

capacitor at approximately 90 MHz; this is well outside the bandwidth of interest. Lastly, phase is affected at both high and low frequencies because the feedback capacitor plays a role in performance of both frequency ranges.

Noise simulations were performed using the noise simulation module in LTSpice®XVII. Results are shown in Fig. 4. 7(a) for different sensor baseline capacitances. The sensor baseline shows impact only in the flat band. Fig. 4. 7(b) shows the noise spectral density for the different capacitance values plotted on a linear scale with respect to baseline capacitance. The impact of

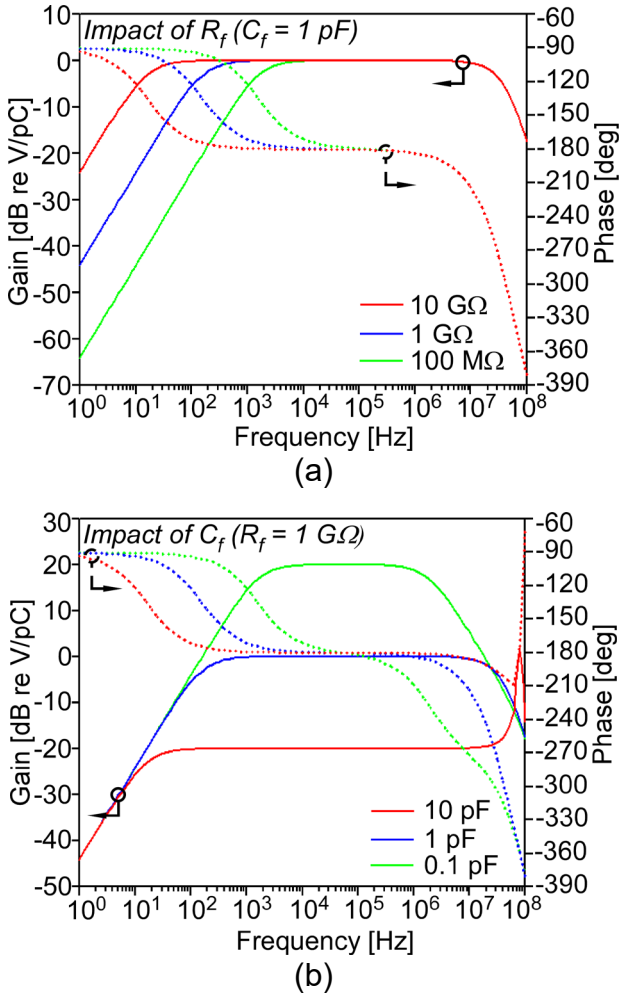

Fig. 4. 6: Charge amplifier simulation results. (a) Impact of feedback resistor R_F on circuit performance. As anticipated, low frequency gain is increased while high frequency gain is unaffected. (b) Impact of feedback capacitor C_F on circuit performance. The gain decreases as C_F increases; the bandwidth changes by the gain-bandwidth specification of the operational amplifier.

sensor baseline has a linear effect on noise, as is predicted by equation 4.13. These simulation results yield much larger noise than anticipated; the simulation must be corrected in future work.

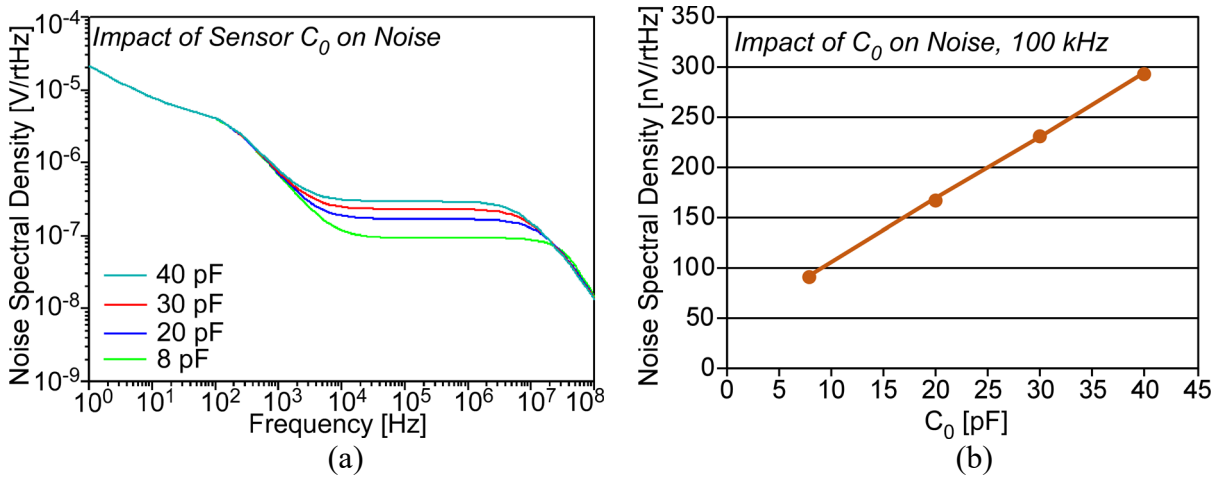

Fig. 4. 7: Impact of baseline capacitance on output noise. (a) Spectral density with varying baseline capacitance, C0. Baseline only has an impact within the -3dB bandwidth. (b) Noise and baseline capacitance have a linear relationship, as predicted by theory.

4.2 Modeling

The lumped diaphragm velocity described in Chapter 2 can be inserted into the small signal equivalent electroacoustic model to conveniently describe behavior in both the mechanical and electrical domains. This model is shown in Fig. 4. 8. The force *f* from acoustic pressure *p* acting over the sensing element diaphragm creates diaphragm velocity $\dot{u}$ that is dependent on the mechanical impedances the force encounters, as is described by equation 2.5. The canonical electroacoustic equations [Kin82] that describe the transducer are as follows:

$$\boldsymbol{v} = \boldsymbol{i}Z_{in} + \dot{\boldsymbol{u}}\phi_{em}Z_{in} \tag{4.14}$$

$$\boldsymbol{p} = \boldsymbol{i}\phi_{me}Z_{in} + \dot{\boldsymbol{u}}Z_r \tag{4.15}$$

where Z_{in} is the input impedance of readout circuit (R_f // C_f), ϕ_{em} is the transduction coefficient from the mechanical to the electrical domain, and ϕ_{me} is the transduction coefficient from the electrical to mechanical domain.. The hydrophone is used as a receiver in this work, so only equation 4.14 is of interest. Transduction coefficient ϕ_{em} is written as

$$\phi_{em} = \frac{C_0 V_B}{d_0}, \tag{4.16}$$

where d_0 is the interelectrode gap and C_0 is baseline capacitance of the sensing element.

The response from each sensing element is calculated individually and superposed in parallel. The resulting electroacoustic model of the hydrophone – circuit device in Enerpac™ LX101 paraffin oil is displayed in Fig. 4. 9. Atmospheric static pressure and 10V sensor bias are assumed. The plot shows analytical sensitivity as a function of frequency from 10 Hz to 10

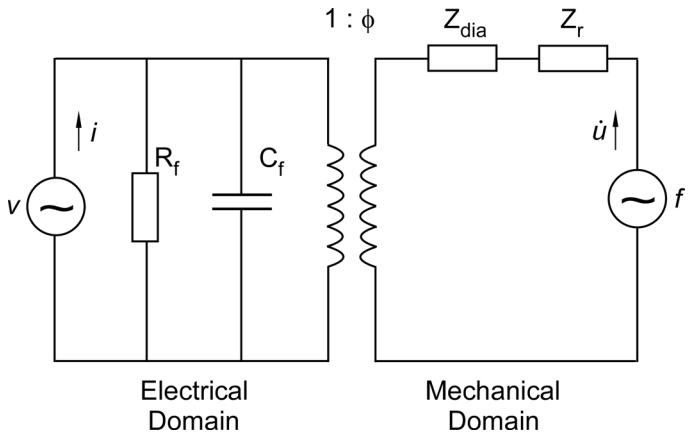

Fig. 4. 8: Equivalent electroacoustic model of a single hydrophone sensing element.

MHz. The low frequency response drops at 20 dB/dec below 100 Hz; this is a direct result from the high pass filter created by the readout circuit's feedback loop. The corner frequency at the low end is approximately 140 Hz. The flat band gain is -221 +/- 3 dB re V/μPa from 161 Hz to 1.6 MHz. The useable bandwidth reaches 6.7 MHz. The contribution to sensitivity of each diaphragm size is plotted in Fig. 4. 10, which includes the response from multiple sensing elements of the same size. Since the response is modelled at atmospheric pressure, most of the sensitivity is from the larger diaphragms. The three smallest diaphragm sizes individually

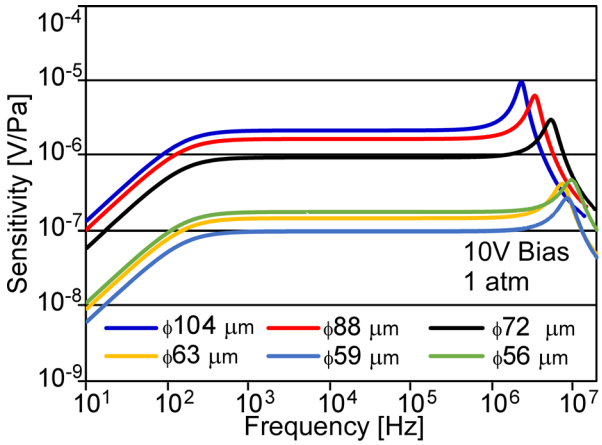

Fig. 4. 9: Analytical sensitivity in oil provided by each diaphragm size at atmospheric pressure and 10V sensor bias. Calculation considers multiple diaphragms of the same size.

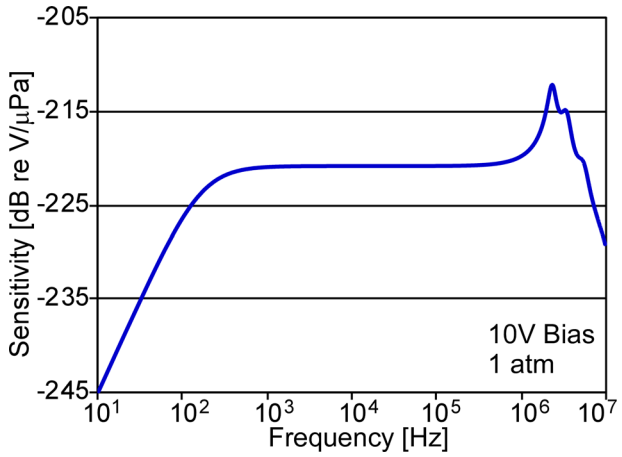

Fig. 4. 10: Analytical frequency response in Enerpac™ LX101 paraffin oil. Low frequency loss of gain is from the high pass filter in the readout circuit feedback loop. Useable bandwidth reaches a 3 dB level of 6.7 MHz.

contribute almost one order of magnitude less than the three largest diaphragm sizes. This changes with static pressure, because the mechanical impedances of the diaphragms change as they enter touch mode. Furthermore, the interelectrode gaps of the smaller sensing elements result in higher contribution to sensitivity at higher static pressures.

The change in sensitivity from increased static pressure is extrapolated from the simulated and experimental static pressure responses. The incremental response, R, of the composite capacitance response is

$$S(P_{static}) = \frac{R(P)V_B}{C_F} = \frac{\Delta C(P)}{\Delta P}\frac{V_B}{C_F}. \tag{4.17}$$

This calculation gives the flat band gain; the sensitivity at atmospheric pressure is subtracted from this value to give the change in sensitivity regardless of frequency within the flat band. Important to note, the calculation may not be accurate near diaphragm resonances; it is common knowledge that the mechanical bandwidth of the diaphragms increases once in touch mode [Ora06]. Results from the experimental and simulated capacitance vs. static pressure responses are shown in Fig. 4. 11. The two curves show general agreement, with peaks in sensitivity

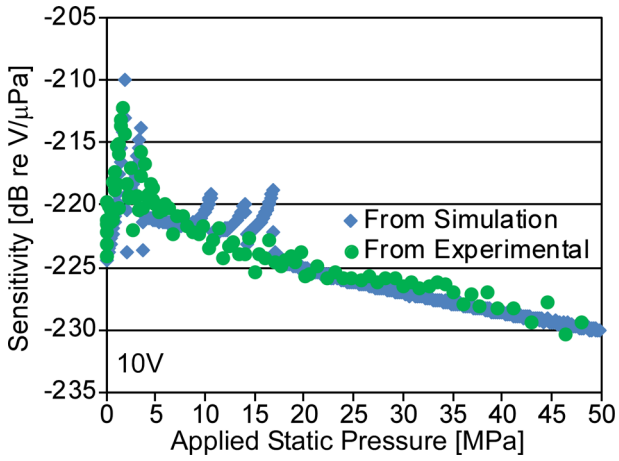

Fig. 4. 11: Estimated impact of applied static pressure on sensitivity for device H106 B1. Both curves are calculated with incremental response extrapolated from respective static pressure responses.

occurring at identical static pressures. The magnitude of the peaks is higher in the curve from simulated static response. This is not surprising, as the response is heavily dependent on non-idealities such as surface roughness and variations in thickness of the insulating dielectric layer. Miniscule differences between simulated and experimental static response can result in such disagreements in sensitivity.

4.3 Experimental Methods

Several testing apparatus were used to characterize the hydrophone. The tests performed were intended to quantify the hydrophone's sensitivity at atmospheric static pressure over a wide frequency band, as well as its change in sensitivity due to increased static pressure. The hydrophone's bandwidth is extremely wide, which necessitated the use of multiple reference transducers and multiple setups for high and low frequencies. This section details and analyzes each testing apparatus, as well as the means by which the hydrophone was implemented.

4.3.1 Hydrophone Implementation

The hydrophone sensor was implemented using a custom-built PCB, which includes quick connectors for easy connect and disconnect. The assembled and disassembled device are shown in Fig. 4. 12. The device consists of three PCBs: a small PCB (4.6 x 4.6 mm^2) in which the sensor is integrated, a circuit board populated with the charge amplifier circuit, and a probe arm that connects the hydrophone sensor PCB to the circuit board. The probe arm allows for the sensor to be inserted into acoustic testing fields while maintaining a low reflection profile. Fig. 4. 13 shows a closeup image of a hydrophone sensor integrated with the sensor PCB.

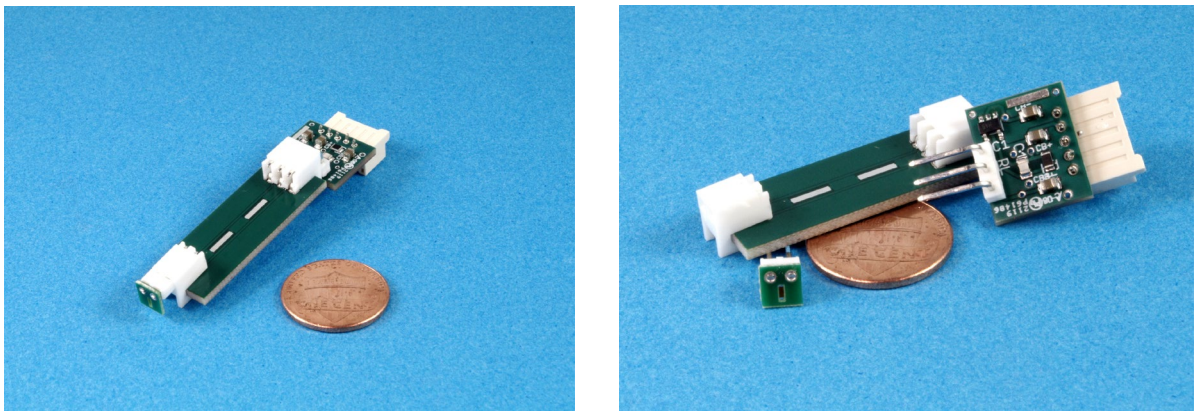

(a) (b)

Fig. 4. 12: Custom PCB used for acoustic testing at atmospheric pressures. The complete device consists of three separate parts, including a circuit board, probe arm, and sensor PCB. (a) The assembled device. (b) Disassembled device.

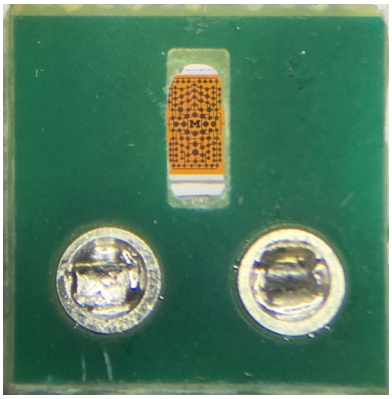

Fig. 4. 13: Closeup image of the sensor PCB. The hydrophone faces downward through a machined slot.

4.3.2 100 kHz, Atmospheric Static Pressure

Acoustic testing at atmospheric pressure was performed in a vertical fluid column. A steel tube 41 mm in diameter and 369 mm tall was filled with paraffin oil (Enerpac®LX101, Milwaukee, WI) and implemented with the top end open to air. Please see Fig. 4. 14(a) for reference. An omnidirectional acoustic source (Aquarian Scientific® AS-1, Anacortes, WA) is placed on the rigid boundary, while a reference hydrophone (Aquarian Scientific® AS-1) is held in place at the exact same axial distance as the DUT. Fig. 4. 14(b) shows a block diagram of the device readout. The AS-1 reference hydrophone is buffered using a preamplifier (Aquarian Audio® PA4, Anacortes, WA) while the DUT is connected to a custom charge amplifier circuit for transduction from charge to voltage. Both devices are held in place by holders that allow for manipulation of the respective device's location in the tube. An acoustic signal is created by applying a sinusoidal voltage (Agilent 33210A function generator, Santa Clara, CA) to the acoustic source through a custom buffer circuit. Each device's voltage response to each discrete

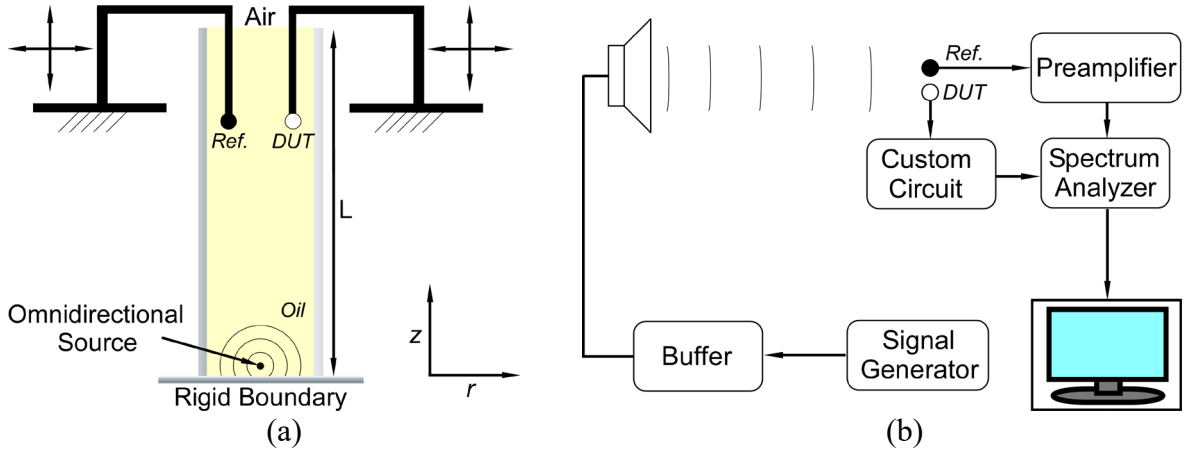

Fig. 4. 14: Experimental acoustic testing at atmospheric pressure up to 100 kHz. (a) A reference device and DUT are placed at an identical location along the tube's axis. (b) Data is read out using a spectrum analyzer.

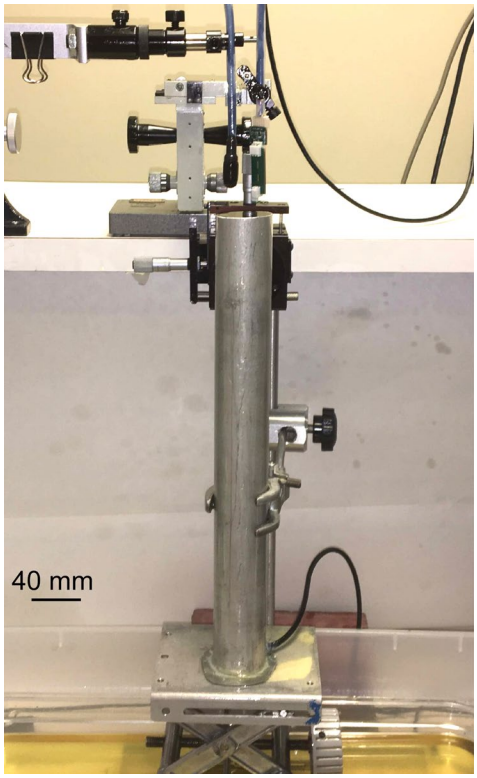

Fig. 4. 15: Optical image of the test setup used for acoustic testing at atmospheric static pressure and up to 100 kHz. A reference and DUT were held in place by holders that allow for precise manipulation of position. A metal tube is used to mitigate interference signals.

frequency is measured using a spectrum analyzer (Agilent 4395A). An optical image of the test setup is shown in Fig. 4. 15. A metal tube mitigates interference signals present in the lab.

Accurate calibration of the heterogeneous hydrophone requires that only planar acoustic waves exist inside the tube. However, the omnidirectional source used in this work must be assumed to create any mathematically possible mode of propagation. Mathematical analysis of the tube was performed in order to understand its acoustic behavior. Background of the following information is available from Kinsler et al and Redwood [Kin82, Red60]. First, the classical wave equation,

$$\nabla^2\phi = \frac{1}{c^2}\frac{\partial^2\phi}{\partial t^2}, \tag{4.18}$$

is converted to cylindrical coordinates and the time factor *exp(jωt)* is introduced. Assuming radial symmetry, the equation becomes

$$\frac{\partial^2\phi}{\partial r^2}+\frac{1}{r}\frac{\partial\phi}{\partial r}+\frac{\partial^2\phi}{\partial z^2}=-\left(\frac{\omega}{c}\right)^2\phi\,. \tag{4.19}$$

In this context, ϕ is a potential function that is related to quantities of interest by the following:

$$p=-\rho\frac{\partial^2\phi}{\partial t^2} \tag{4.20}$$

$$u_r=\frac{\partial\phi}{\partial r} \tag{4.21}$$

$$u_z=\frac{\partial\phi}{\partial z} \tag{4.22}$$

where p is acoustic pressure, u_r is radial displacement, and u_z is z-axis displacement. Next, we assume the function $\phi = R(r)Z(z)$, where R is a function of r only and Z is a function of z only. Inserting into equation 4.15, we get two differential equations.

$$\frac{\partial^2 R}{\partial r^2}+\frac{1}{r}\frac{\partial R}{\partial r}+k_r^2R=0 \tag{4.23}$$

$$\frac{\partial^2 Z}{\partial z^2}+\left[\left(\frac{\omega}{c}\right)^2-k_r^2\right]Z=0 \tag{4.24}$$

k_r is the wave number in the radial direction, and is related to the wave number in the axial direction, k_z, by the following:

$$k_z^2=\left(\frac{\omega}{c}\right)^2-k_r^2\,. \tag{4.25}$$

Solutions to equation 4.24 include both *cos(kzz)* and *sin(kzz)*; the selection of which to use is based on which will correctly satisfy boundary conditions. In this case we will use cosine, which will be explained shortly. Meanwhile, the solution to equation 4.23 is

$$R(r) = AJ_0(k_r r)\,, \tag{4.26}$$

where A is an appropriate constant and J_0 is the zeroth order Bessel function. The solution to ϕ can now be written as

$$\phi = AJ_0(k_r r)\cos(k_z z)\, e^{j\omega t}\,. \tag{4.27}$$

The boundary conditions of the cylindrical tube used for calibration pose restrictions on the waves that can propagate through the tube. The rigid metal tube shown in Fig. 4. 14(a) provides zero radial velocity at $r = a$, where a is tube radius, and zero axial velocity at $z = 0$. Since the tube is open to air at $z = L$, that itself is a boundary condition. For simplicity, we will approximate the air pressure as a vacuum and assume that the acoustic pressure at $z = L$ is zero. Though this isn't true, the vast acoustic impedance mismatch between oil and air will result in acoustic pressure being significantly lower at $z = L$ than values inside the tube and is a reasonable approximation for the purpose of describing modes of propagation. The pressure and displacements derived from equation 4.23 are

$$p = \rho\omega^2 AJ_0(k_r r)\cos(k_z z)\, e^{j\omega t} \tag{4.28}$$

$$u_r = -k_r AJ_1(k_r r)\cos(k_z z)\, e^{j\omega t} \tag{4.29}$$

$$u_z = -k_z AJ_0(k_r r)\sin(k_z z)\, e^{j\omega t} \tag{4.30}$$

Starting with the radial boundary condition, $\partial u_r/\partial t = 0$ at $r = a$ requires that

$$J_1(k_r a) = 0, \tag{4.31}$$

or more specifically that $k_r a = j_{1m}$, where j_{1m} is a root of the first order Bessel function and m is an integer value. Some values of j_{1m} are tabulated in Table 4. 1. Next, we will consider the boundary conditions at $z = L$ and $z = 0$. At $z = L$, the acoustic pressure is approximated to be

Table 4. 1: Values of roots to the first order Bessel function, $J_1(x)$.

m	j_{1m}
0	0
1	3.83
2	7.02
3	10.17
4	13.32
5	16.47
6	19.62

zero. The cosine term in equation 4.28 must therefore equal zero to satisfy the boundary condition. More specifically,

$$k_z L = \frac{\pi}{2}(2n+1)\,, \tag{4.32}$$

where n is an integer value. At $z = 0$, the $\partial u_z/\partial t = 0$ condition is satisfied by the sine term in equation 4.26. This is an artifact of the choice to use cosine as the solution to equation 4.24. The potential function in equation 4.27 can now be rewritten as

$$\phi = AJ_0\left(\frac{j_{1m}}{a}r\right)\cos\left\{\frac{\pi}{2L}(2n+1)z\right\}e^{j\omega t}\,. \tag{4.33}$$

Now that we've solved for both wave numbers, the possible frequencies to propagate through the tube are described as

$$\frac{\omega}{c} = \sqrt{k_r^2 + k_z^2} = \sqrt{\left(\frac{j_{1m}}{a}\right)^2 + \left\{\frac{\pi}{2L}(2n+1)\right\}^2}\,. \tag{4.34}$$

Integer values m and n correspond to acoustic modes in their respective coordinate axes. The m integer is of great interest because it defines the radial profile of propagating acoustic waves. Each value of m corresponds to a different mode that produces its own radial profile.

The radial modes to propagate through the tube can be predicted through the relationship between wave numbers k_z and k_r. These wave numbers arise from the model of plane wave propagation through a cylindrical tube, shown in Fig. 4. 16. Any mode of propagation can be

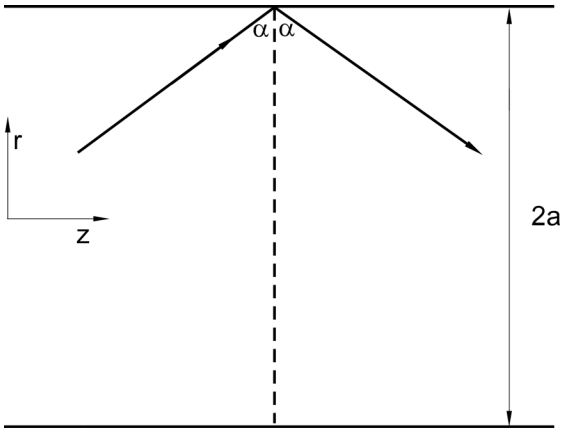

Fig. 4. 16: Wave propagation through a cylindrical waveguide.

thought of as a synthesis of plane waves reflecting at the boundaries and travelling along the waveguide in a zig-zag path [Red60]. Non-planar radial profiles are due to the "interference pattern" formed by these planar waves as they interact with each other [Red60]. In addition to the relationship in equation 4.25, k_z and k_r can be described as

$$k_z = \frac{\omega}{c} sin\alpha \tag{4.35}$$

$$k_r = \frac{\omega}{c} cos\alpha \tag{4.36}$$

where α is the angle of incidence shown in Fig. 4. 16. Another value that arises from these relationships is the phase speed, c_p, which is the speed at which a wave of constant phase will travel down the tube.

$$c_p = \frac{\omega}{k_z} = \frac{c}{sin\alpha} \tag{4.37}$$

Using equations 4.25 and 4.37, the relationship between c_p, c, and ω can be written as

$$c_p = \frac{c}{\sqrt{1 - \left(k_r \frac{c}{\omega}\right)^2}} \ . \tag{4.38}$$

Equation 4.38 is used to predict which acoustic modes will propagate down the tube. Each distinct mode defined by m produces a unique value for k_r. If the value of $k_r c/\omega$ in

equation 4.38 is larger than unity, then k_z is imaginary and negative. The wave is attenuated according to the term *exp(-|k_z|z)* and is described as *evanescent*. In this case, energy is not transmitted along the tube. This condition corresponds to α being equal to zero, in which case the acoustic wave oscillates in the radial direction only and cannot propagate down the tube. Increasing frequency reduces the value of $k_r c/\omega$ until it reaches a value of 1. Above this frequency, denoted as the cutoff frequency, f_{co}, a given mode can propagate.

$$f_{co} = \frac{k_r c}{2\pi} \tag{4.39}$$

The cutoff frequency corresponds to phase speed approaching infinity. As frequency further increases, $c_p \rightarrow c$ in which case $\alpha \rightarrow \pi/2$.

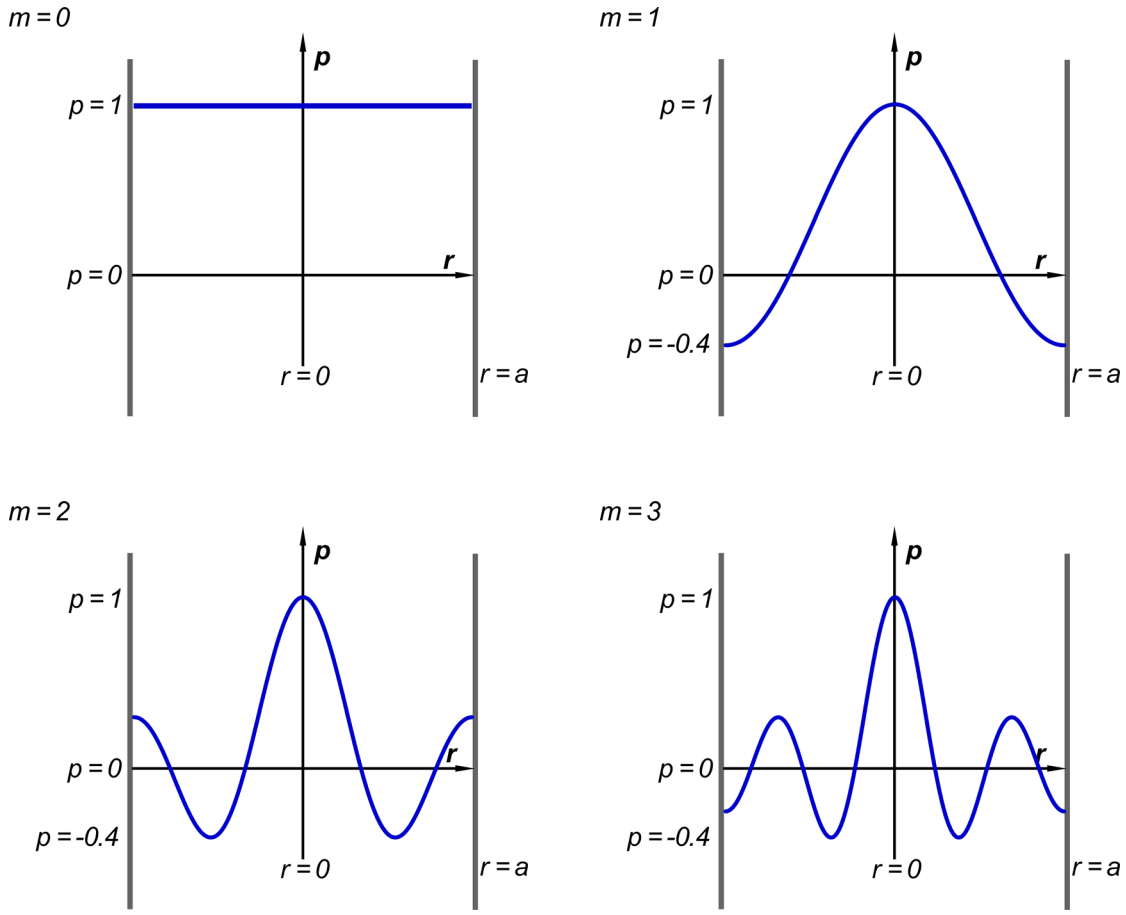

Fig. 4. 17: Normalized radial acoustic profiles for different m values. The value m = 0 corresponds to a plane wave, which propagates at any frequency.

The modes that will exist in the tube at a given frequency are described by the possible combinations of k_z and k_r in equation 4.34. Some of these modes are shown in Fig. 4. 17. The zeroth mode corresponds to a plane wave; from Table 4. 1, $j_{10} = 0$. Therefore, according to equation 4.35, its cutoff frequency is 0 Hz. This means the plane wave can propagate at any frequency and is the only mode present below the cutoff frequency of the first mode, which is

$$f_{co} = \frac{j_{1m}}{a}\frac{c}{2\pi} = \frac{3.83}{0.0205\ m}\frac{1400\ m/s}{2\pi} = 41{,}628\ Hz\,. \tag{4.40}$$

The maximum testing bandwidth in this experiment is limited by the transmitter and reference hydrophone to 100 kHz. Data from Table 4. 1 reveals that this frequency is above the cutoff for the $m = 0, 1,$ and 2 modes, but is below the 110,538 Hz cutoff of the third mode. This means that two extra modes in addition to the plane wave will be encountered in this work.

Accurate calibration requires that only plane waves be present inside the tube. This means that the transmitter can only be operated at select frequencies. The frequencies of operation are chosen from equation 4.34. It is assumed that $m = 0$, and frequency is only determined by values of k_z that satisfy boundary conditions.

$$f = \frac{c}{4L}\,(2n + 1) \tag{4.41}$$

Frequencies chosen from equation 4.41 are natural resonant modes of the tube and will produce standing waves with planar profiles only. This is because there is no possible combination of k_z and k_r that exists at these frequencies without m being equal to zero. Each frequency corresponding to a value of n was simulated using COMSOL Multiphysics® 5.3a Pressure Acoustics module in the frequency domain. A 2D-axisymmetric geometry was implemented. The acoustic source was modeled as a monopole point source, as shown in Fig. 4. 18. The point source was simulated to behave as a simple source with an arbitrary source strength of 1 mm^3/s. The side and bottom of the tube were programmed to behave as a hard

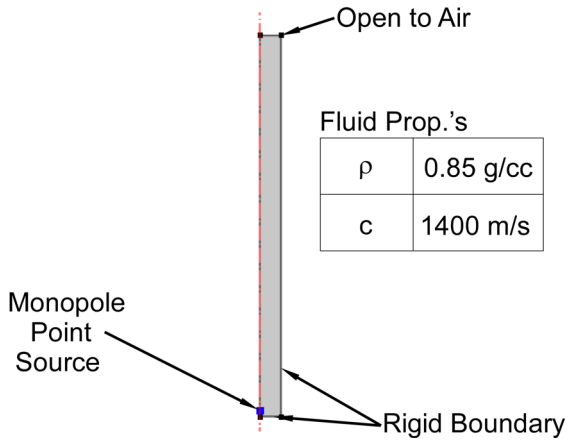

Fig. 4. 18: Simulation geometry. A 2D-axisymmetric simulation was performed using the Pressure Acoustics module in COMSOL Multiphysics® 5.3a.

boundary, whereas the top was programmed to have the acoustic impedance of air. Lastly, the maximum mesh element was programmed to be much smaller than the smallest wavelength simulated.

Results in Fig. 4. 19 reveal that only plane waves are present at these frequencies. The tube profiles are a select few from the entire frequency band, but are representative of all simulated frequencies from equation 4.41 between 0 Hz and 100 kHz. Fig. 4. 19 shows steady state sound pressure levels (SPL) referenced to 1 μPa inside the tube. The number of wavelengths present inside the tube correspond to the frequency and length of the tube, as expected. The SPL at the air oil interface is significantly lower than the SPL inside the tube. This is due to the impedance mismatch between air and oil.

Simulation corroborates which frequencies will produce standing plane waves, but it is important to consider what will happen at frequencies outside what is predicted by equation 4.41. First, remember that the zeroth mode cutoff frequency is 0 Hz. This means that plane waves can exist at any frequency. Above the zeroth mode cutoff and below the first mode cutoff, still only plane waves will exist. However, outside of the frequencies predicted by equation 4.41, waves will not be propagating in a natural resonant mode of the tube. In other words, the plane waves

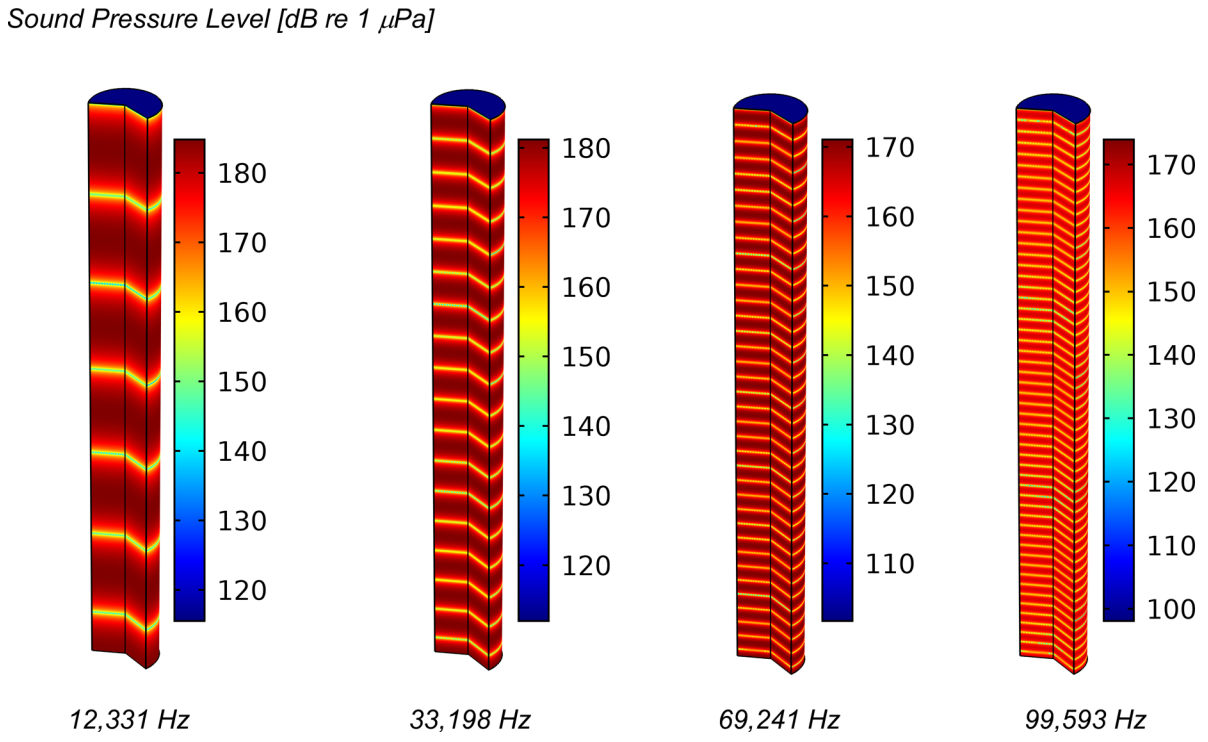

Fig. 4. 19: Sound pressure level simulation results. A selection of frequencies predicted by equation 4.30 are displayed. Results show steady state sound pressure levels inside the tube. The number of wavelengths present correspond to the frequency and tube length, as expected. The radial profile is planar at these frequencies.

will reflect off the tube opening and tube bottom at varying phase to create interference patterns inside the tube. Above the first mode cutoff, the same is true except now the radial profile will be susceptible to interference patterns. As frequency rises above more cutoff frequencies, it is possible for interference between more modes. The presence of different modes is dependent on the acoustic source. An omnidirectional source, as is used in this work, must be assumed to create any mode possible. This highlights the critical importance that only frequencies from equation 4.41 be used for calibration.

4.3.2 High Static Pressure Acoustic Setup

The apparatus used for high pressure acoustic testing is identical to that used for seismic ELM testing in Chapter 3. A 3D representation is shown once again in Fig. 4. 20 for reference.

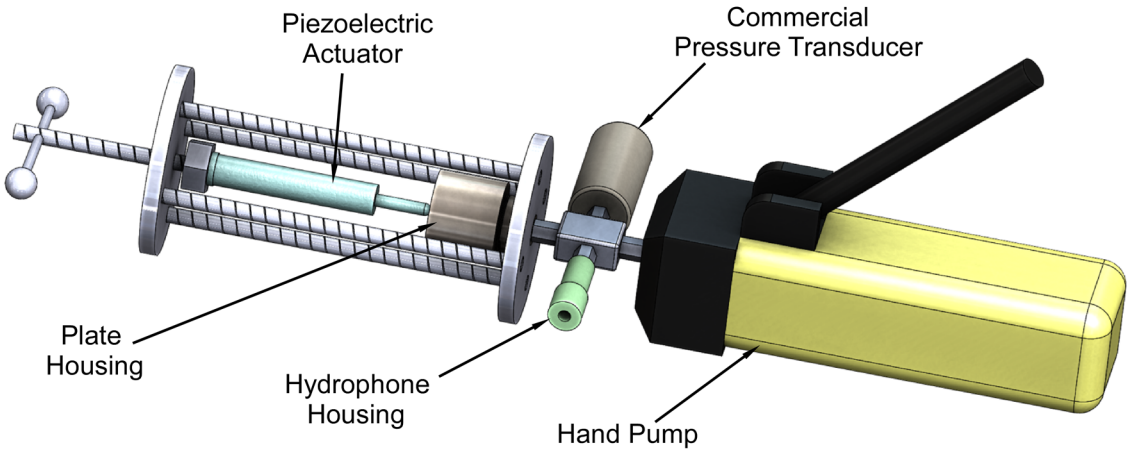

Fig. 4. 20: Overview of the high-pressure acoustic testing apparatus.

The piezoelectric stack actuator deflects a metal plate to create acoustic waves inside the pressure vessel. The hydrophone sensor is connected to a 6-pin connector (Fig. 4. 21) and placed inside the hydrophone housing. The 6-pin connector acts as a plug for holding pressure and also allows electrical feedthrough outside the pressure vessel. The custom readout circuit is equipped with easy connect and disconnect hardware. A testing diagram is displayed in Fig. 4. 22. A signal generator is used with a custom buffer circuit to drive the piezoelectric stack actuator and create acoustic waves inside the pressure vessel. All equipment is identical to description in

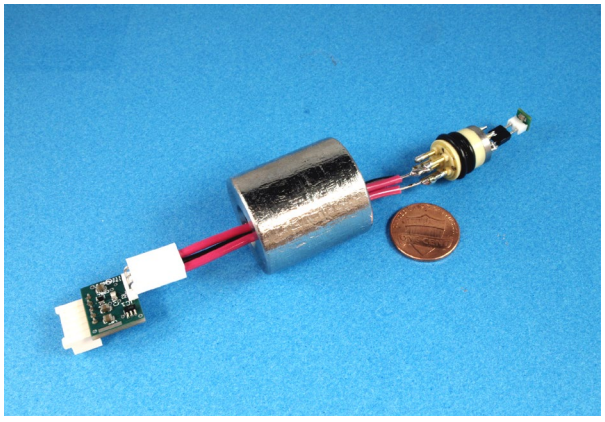

Fig. 4. 21: Electrical connections between the hydrophone and readout circuit. A custom 6-pin connector acts as a pressure plug and provides electrical throughput outside the hydrophone housing (please see Fig. 4. 20 for reference). The readout circuit is equipped with easy connect and disconnect hardware.

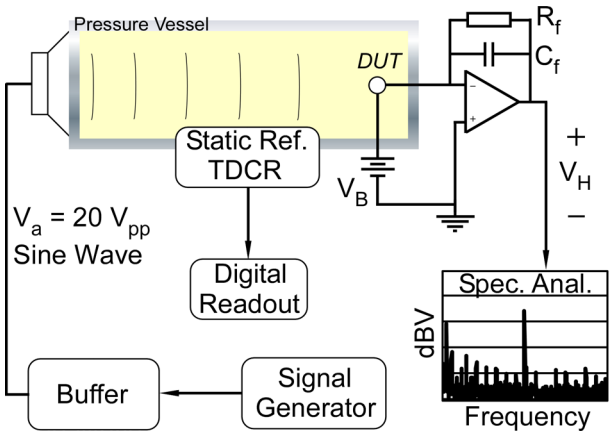

Fig. 4. 22: Testing diagram for the high-pressure acoustic test setup. A signal generator is buffered and used to drive the piezoelectric stack for acoustic wave creation. The hydrophone (DUT) is read out using the custom charge amplifier circuit and a spectrum analyzer.

Chapter 3. The readout circuit is connected to a spectrum analyzer for quantification of the acoustic signal measured by the hydrophone. The commercial pressure transducer is not sensitive enough for use as an acoustic reference and is used only for static pressure measurements. The manual hand pump once again generates applied static pressure up to 50 MPa.

Since there is no acoustic reference sensor, only experimental change in sensitivity due to static pressure is measured. In this case, a single tone at constant voltage is applied to the stack actuator. The measured voltage from the readout is recorded at different static pressures. The change in voltage is identical to the change in sensor sensitivity. This method assumes that the acoustic signal does not change with static pressure, which is true if there are no air bubbles present inside the pressure vessel. The steel pressure vessel does have slight changes in geometry due to the massive static pressure but was found to have minimal impact on the acoustic pressure.

Before beginning experimental testing, it was important to model the setup to determine which frequencies will cause resonance in the stack actuator to avoid major damage to the stack.

The resonant frequency of the combined actuator-plate-vessel system will be different than that of each individual component. When a voltage is applied to the stack actuator, the actuator must work against its own mechanical impedance ($\boldsymbol{Z}_{ms}$), the plate mechanical impedance ($\boldsymbol{Z}_{mp}$), as well as the input mechanical impedance of the pipe ($\boldsymbol{Z}_{m0}$) in order to move the plate. Please see Fig. 4. 23 for reference. Mathematically, the resultant speed of the plate is described by equation 4.42, where $\boldsymbol{f}$ is the force applied to the plate as a function of time.

$$\boldsymbol{f} = \boldsymbol{Z}_{mtot}\boldsymbol{u}(0,t) = \left(\boldsymbol{Z}_{ms} + \boldsymbol{Z}_{mp} + \boldsymbol{Z}_{m0}\right)\boldsymbol{u}(0,t) \tag{4.42}$$

By definition, the system is in resonance when the reactive components of the total mechanical input impedance, $\boldsymbol{Z}_{mtot}$, go to zero. The stack and plate mechanical impedances are determined by respective damping, mass, and stiffness of each component. These impedances are described by equations 4.43 and 4.44, respectively.

$$\boldsymbol{Z}_{ms} = R_{ms} + j\left(\omega m_s - \frac{s_s}{\omega}\right) \tag{4.43}$$

$$\boldsymbol{Z}_{mp} = R_{mp} + j\left(\omega m_p - \frac{s_p}{\omega}\right) \tag{4.44}$$

Here, R_m is a mechanical (real) resistance, m is mass, s is stiffness, and ω is angular frequency. Values for equations 4.43 and 4.44 can easily be calculated. The input mechanical impedance,

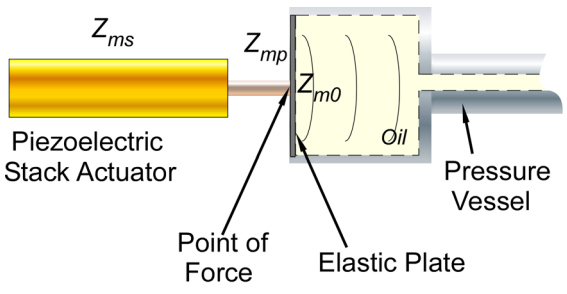

Fig. 4. 23: Acoustic pressure generation. A stack actuator applies a complex driving force to an elastic metal plate. Vibration of the plate generates acoustic waves inside the pressure vessel. The magnitude of pressure waves depends on the total mechanical impedance at the input, including that of the plate and actuator.

$\boldsymbol{Z}_{m0}$, however, is more complicated. The complex quantity $\boldsymbol{Z}_{m0}$ is described in equation 4.45 as the ratio of pressure at the inlet, divided by particle velocity, multiplied by cross sectional area at the input.

$$\boldsymbol{Z}_{m0} = S\frac{\boldsymbol{p_{in}}(t)}{\boldsymbol{u_{in}}(t)} \tag{4.45}$$

The input mechanical impedance was solved for analytically and compared to simulation through use of appropriate boundary conditions. Fig. 4. 24 is used as reference. The plate and plate housing are on the left side of the figure; the diagram has the same orientation as in Fig. 4. 20. The origin of the system is located at the center of the four branches, labelled as (0,0,0,0). Each pipe branch uses its own axis (*w,x,y,z*). There are several assumptions made about some aspects of the pressure vessel. The first assumption is that the acoustic impedance of the vessel walls can be approximated as infinite. The walls of the pressure vessel are steel and have

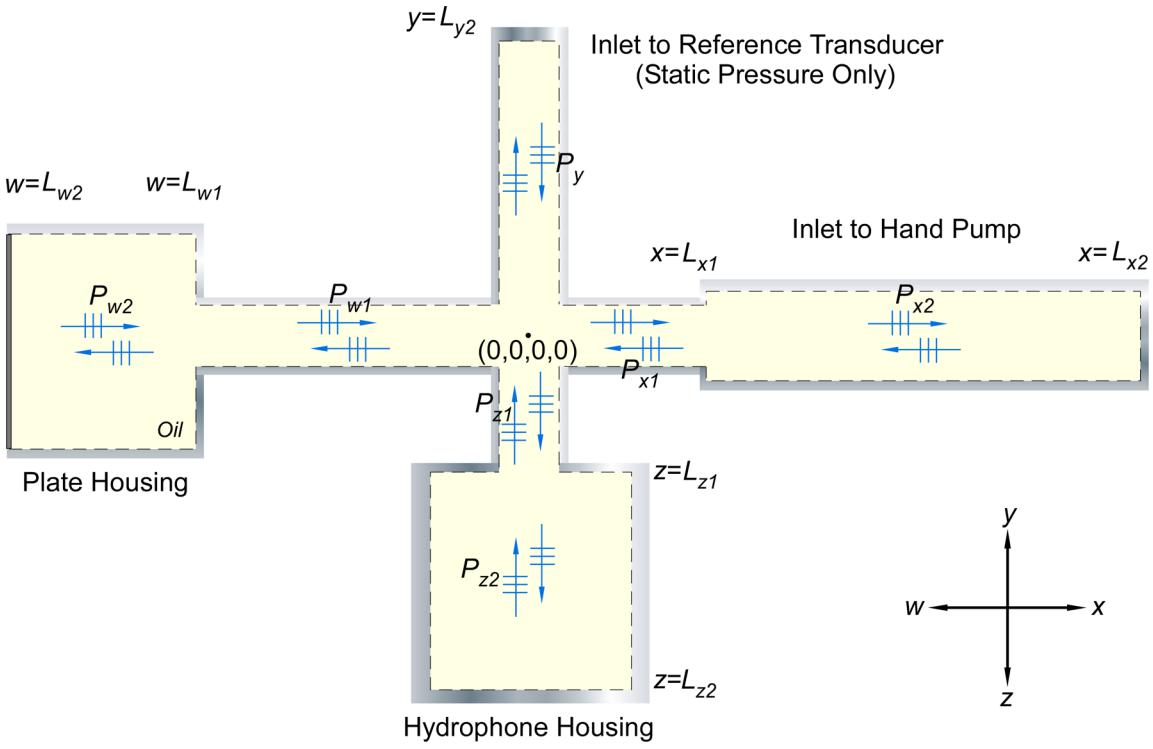

Fig. 4. 24: Internal diagram of the pressure vessel. The components combine to make a system of pipes, which creates a complex pressure field inside the vessel.

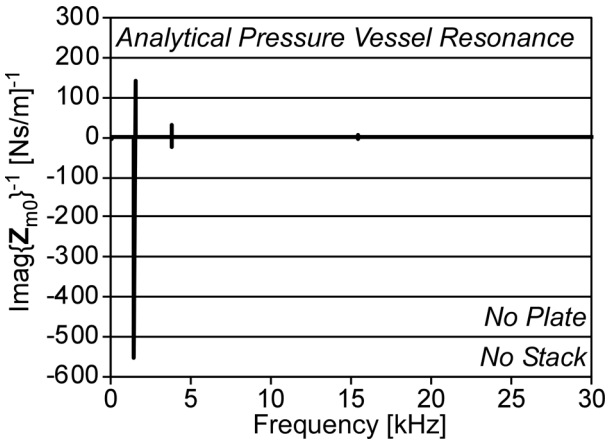

Fig. 4. 25: Analytical resonance of the pressure vessel. Resonance is graphically determined by identifying peaks in the curve. These peaks correspond to frequencies in which Zm0 is close to zero. The plot shows major resonance at 1539 Hz. Figure plotted with 1 Hz increments.

considerably higher acoustic impedance than the oil, which makes this assumption reasonable. The second assumption is that the acoustic signals propagating through the vessel are plane waves only. This assumption is accurate below the cutoff of the first radial mode of propagation, which is estimated to be above 100 kHz. Lastly, the plate deflections of the elastic plate are assumed to be small enough that the plate can be approximated as a lumped element. This means the displacement close to the edge is identical to the displacement at the center.

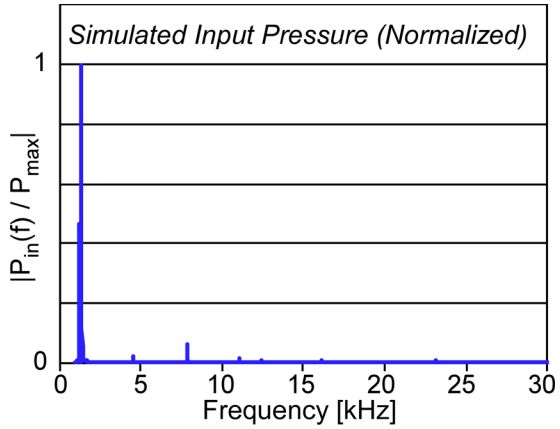

Fig. 4. 26: Simulated input pressure of the pressure vessel. The simulation shows resonance occurring at 1380 Hz. This agrees well with the analytical value, with 11.5% relative error.

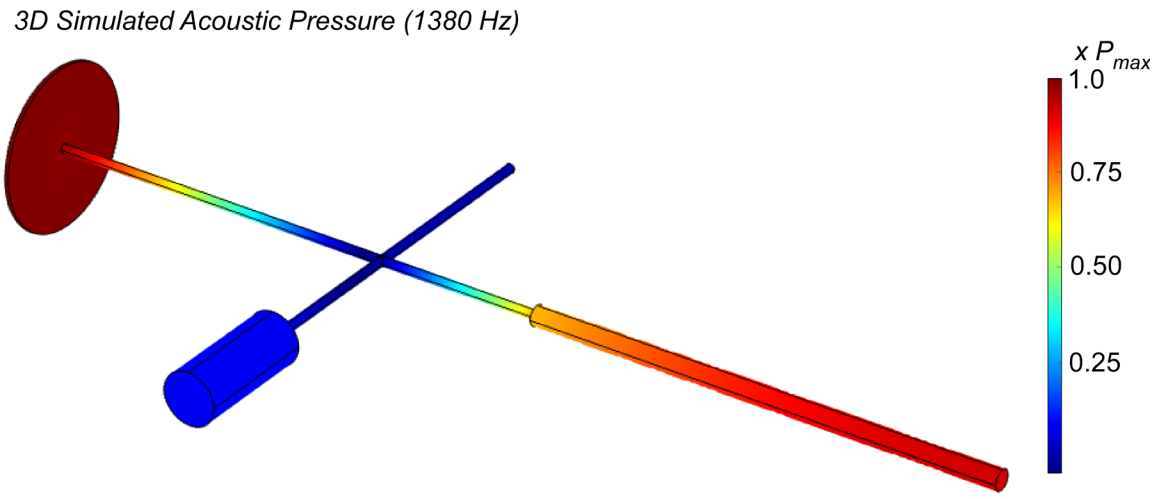

Fig. 4. 27: Simulated acoustic pressure at resonance. The maximum pressure exists at the plate housing, where the actuator contacts the pressure vessel.

Acoustic resonance at the input of the pressure vessel will exist when the velocity per unit force input is at a maximum. This occurs when the imaginary part of $\boldsymbol{Z}_{m0}$ is small or zero. Fig. 4. 25 shows the inverse of Imag$\{\boldsymbol{Z}_{m0}\}$. There is a major peak at 1539 Hz, which reveals the fundamental resonant mode of the pressure vessel. Other less prominent resonances occur at higher frequencies, but are not as critical because they are beyond the first resonant mode that must be avoided. The normalized acoustic pressure was simulated and plotted in Fig. 4. 26 for comparison. The simulation similarly shows a major resonance at low frequency. The simulated resonant frequency at 1380 Hz, which yields a percent relative error of 11.5% when compared to analytical calculation. Both analysis and simulation show additional resonances at below 5 kHz and above 15 kHz. Simulation shows several extra resonances that are not revealed by analysis; only the first resonance is important for this work because the actuator must be driven below this frequency. The close agreement between analysis and simulation for the fundamental resonant mode of the pressure vessel means that analysis can be used as an acceptable tool for estimating the first resonant mode. A depiction of the pressure field inside the pressure vessel at resonance is shown in Fig. 4. 27.

Now that a valid analytical equation for input mechanical impedance of the test setup has been realized, equation 4.42 can be used to find the resonant frequencies of the combined system. The mechanical resonances of the actuator-plate-vessel system can be determined by the mechanical reactance and will be solved graphically due to the complicated nature of these equations. Once again, the inverse of the total mechanical impedance is plotted to aid in identifying resonances.

$$Imag\{\boldsymbol{Z}_{mtot}\}^{-1} = Imag\{\boldsymbol{Z}_{ms} + \boldsymbol{Z}_{mp} + \boldsymbol{Z}_{m0}\}^{-1} \tag{4.46}$$

Fig. 4. 28 shows equation 4.46 plotted with respect to frequency. The inverted quantity of the total input mechanical resistance yields large peaks at frequencies of resonance. Addition of the elastic plate and actuator stack increases the first system resonance from 1539 Hz up to 9335 Hz. This increase in resonance is expected, since the mechanical resonances of the stack and plate are both significantly higher than that of the pressure vessel. For example, the plate's natural frequency is 7181 Hz and the stack actuator's published natural frequency is 20 kHz. This resonance above 9 kHz is expected to damage the stack actuator; as a result, testing was performed below this frequency. Unfortunately, electromagnetic interference, from the voltage

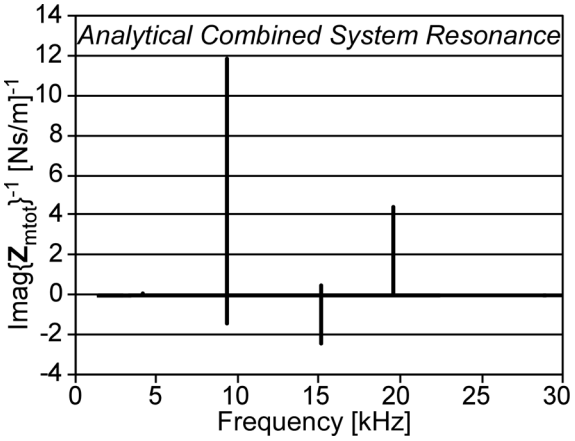

Fig. 4. 28: Analytical resonance of the combined actuator-vessel system, including the elastic plate. The first resonance mode is raised from 1539 Hz to 9335 Hz. This is due to the increased mechanical impedances provided by the actuator and plate.

signal used to drive the stack actuator, precluded experimental verification of the above model. The interference is documented in Appendix B.

4.3.3 MHz Band, Atmospheric Static Pressure

Testing was conducted at atmospheric static pressure to demonstrate the heterogeneous hydrophone's wide bandwidth. This was performed using short acoustic pulses generated by an Olympus Panametrics™ V303-SU ultrasonic transducer inside a tub filled with the same oil used in previous tests. Unlike the low frequency signals measured in the tube, higher frequency signals have shorter wavelength, which allows for pulsed signals that do not interact with the testing environment. A 3D representation of the test setup is shown in Fig. 4. 29 and an optical image of the setup is shown in Fig. 4. 30.

The ultrasonic transducer has significant directional and near field effects that must be taken into consideration. The transducer is a commercial ϕ12.7 mm piezoelectric device that generates acoustic waves with applied voltage and can be modeled as an unbaffled circular piston. Kinsler et al. [Kin82] describe the axial acoustic pressure as

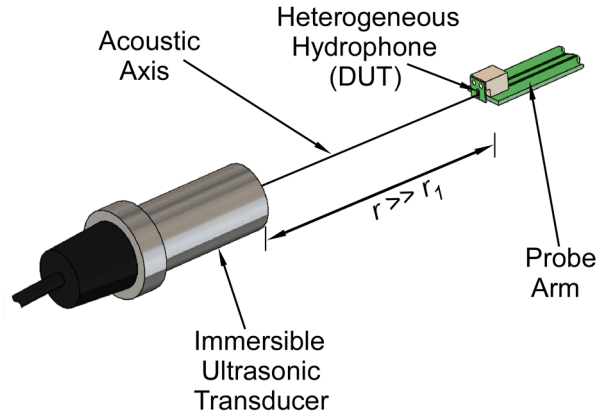

Fig. 4. 29: 3D model depicting the wideband acoustic test setup at atmospheric static pressure. The center of the heterogeneous hydrophone is aligned with the center of the ultrasonic transducer and far enough from the transducer to avoid near field acoustic effects.

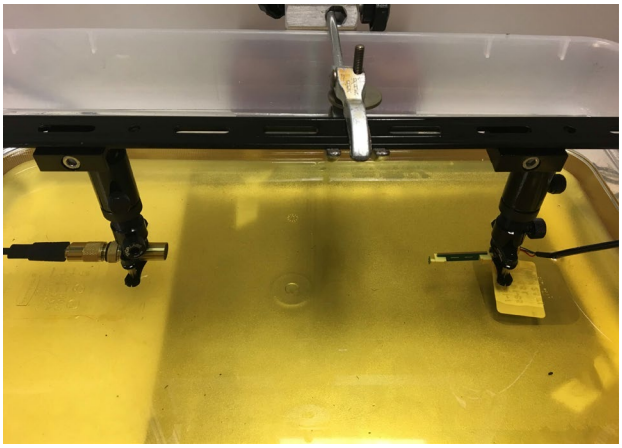

Fig. 4. 30: Wideband test setup used at frequencies into the MHz range. An Olympus Panametrics™ V303-SU ultrasonic transducer is used to create the acoustic signal. Optical grade equipment aligns the devices and enables fine-tuned movement of each.

$$P_{ax}(k,r) = \rho c U_0 \left| sin\left\{ \frac{1}{2} kr \left[\sqrt{1 + \left(\frac{a}{r}\right)^2} - 1 \right] \right\} \right| , \tag{4.47}$$

where U_0 is the uniform velocity magnitude of the oscillating piston face, $k = \omega/c$ is the wave number, r is axial distance from the piston face, and a is the piston radius. When equation 4.47 is plotted with along r with a constant value for ka, near field effects become apparent. Near field

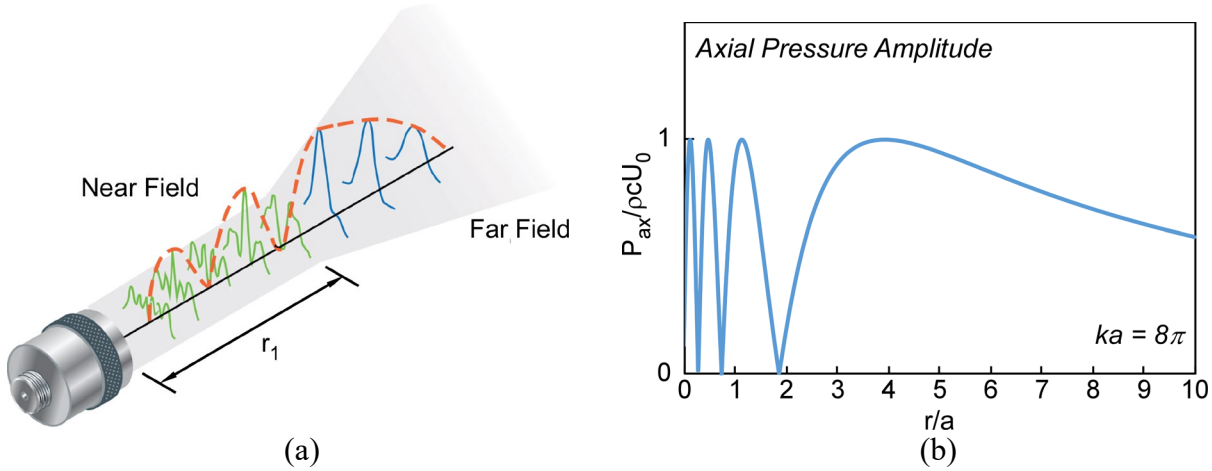

Fig. 4. 31: Anticipated axial behavior of the V303-SU ultrasonic transducer. (a) Depiction of near and far field behavior. Distance r_1 determines the extent of the near field and can be found from equation 4.48 using m = 1. Modified from [Oly18].

axial effects are depicted in Fig. 4. 31(a) and plotted in Fig. 4. 31(b). The axial pressure changes between a normalized value of 0 and 1 until the axial distance reaches the far field. The zeros of Fig. 4. 31(b) (equation 4.47) are given by different values of integer *m* in equation 4.48. The furthest zero from the transmitter, corresponding to $m = 1$, defines the extent of the near field. Beyond r_1, the axial pressure magnitude drops approximately by r^{-1}. Once $a = \lambda/2$, $r_1 = 0$ and there is no near field. The transmitter behavior approaches that of a simple source as frequency further reduces.

$$r_m = \frac{ka^2}{2\pi m} - \frac{\pi m}{2k} \tag{4.48}$$

Lastly, the acoustic beam width is dependent on frequency and distance from the transmitter. Equation 4.49 describes the beam profile, which is dependent on *k* and angle θ from the axis. Please see Fig. 4. 32 for reference. The function J_1 is the first order Bessel function of the first kind. The beam profile varies between 0 and 1, and is multiplied by the axial pressure in equation 4.47 to produce a complete description of the transmitted pressure field.

$$H(k,\theta) = \left|\frac{2J_1(ka\sin\theta)}{(ka\sin\theta)}\right| \tag{4.49}$$

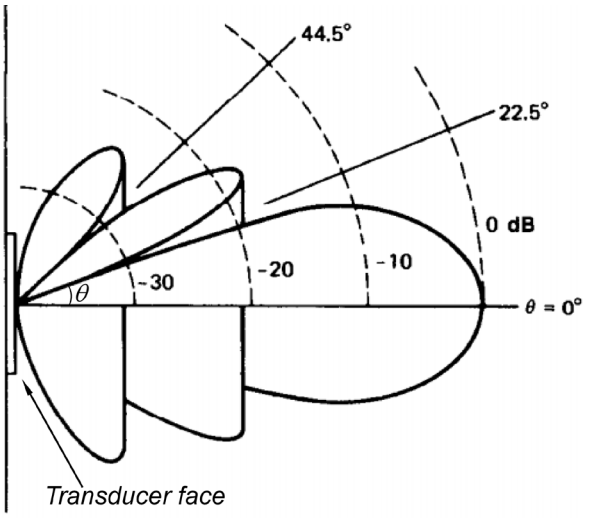

Fig. 4. 32: Beam pattern for an unbaffled circular piston radiating sound with ka = 10. Modified from [Kin82].

The angle θ is shown in Fig. 4. 32. A smaller transducer face will result in less pressure variation at distance *r* from the transducer. The radius *a* of the Olympus™ V303-SU transducer used in this work was 6.35 mm, which results in suitable beam width for use with the heterogeneous hydrophone. No spatial averaging corrections were required to collect accurate measurements.

4.4 Experimental Results

4.4.1 Circuit Characterization

The charge amplifier circuit described in Section 4.1 and pictured in Section 4.3 was experimentally characterized using a network analyzer (NA, Agilent 4395A). A 1 pF input capacitor was connected to the input where an RF signal was applied. The input and output signals were measured by the NA at varying frequency to generate a transfer function. Phase measurements were also recorded. The input voltage acting over the 1 pF capacitor creates 1 pC per volt at the circuit input. The measured transfer function is therefore the circuit gain in units

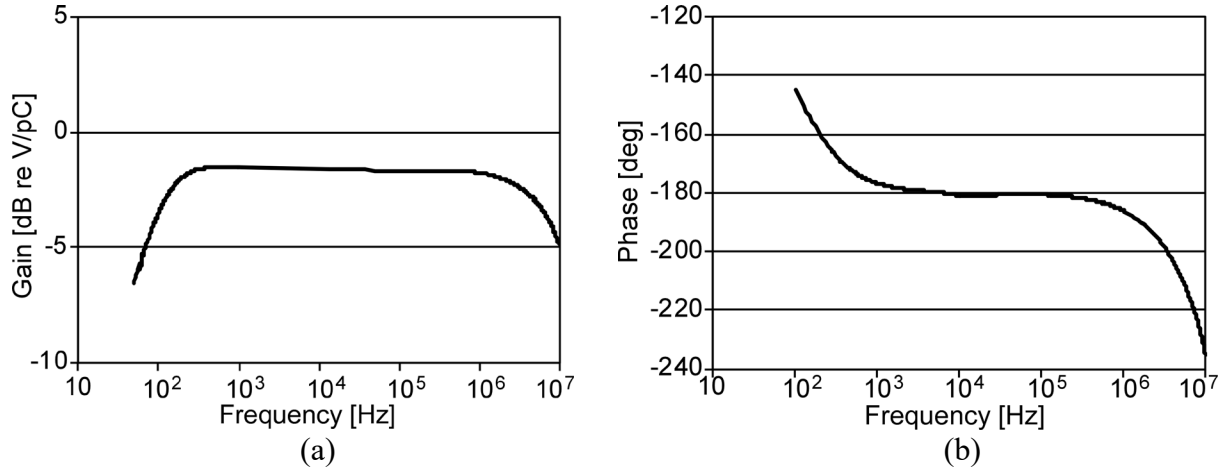

Fig. 4. 33: Experimental circuit characterization results. (a) Circuit gain in units of dB re V/pC. Flat band gain is approximately -1.5 dB, which is lower than the anticipated value of 0 dB. This is attributed to tolerance variation in the feedback capacitor as well as non-zero parasitics present in the PCB. (b) Circuit phase. Phase closely matches expected values.

Table 4. 2: Experimental circuit values of note.

Flat Band Gain	-1.5 dB re V/pC
f_{3dB} Low	77.3 Hz
f_{3dB} High	8.85 MHz

of dB referenced to 1 V/pC, corrected for input capacitor tolerance. Experimental data is shown in Fig. 4. 35. The flat band gain in (a) is approximately -1.5 dB, which is slightly lower than the expected value of 0 dB. This is attributed to the feedback capacitor's tolerance as well as non-zero parasitic capacitance in the PCB. A 1.00 pF feedback capacitor should yield 0 dB of gain; -1.5 dB of gain corresponds to an equivalent feedback capacitance of 1.19 pF, which is not unreasonable. The phase measurements in (b) closely match the expected values. Some parameters of interest are tabulated in Table 4. 2. Noise floor measurements with the sensor are studied in Section 4.4.5.

4.4.2 100 kHz, Atmospheric Pressure

The heterogeneous hydrophone was calibrated up to 100 kHz. The calibration curve is shown in Fig. 4. 34. The testing bandwidth is significantly lower than the resonant frequency of

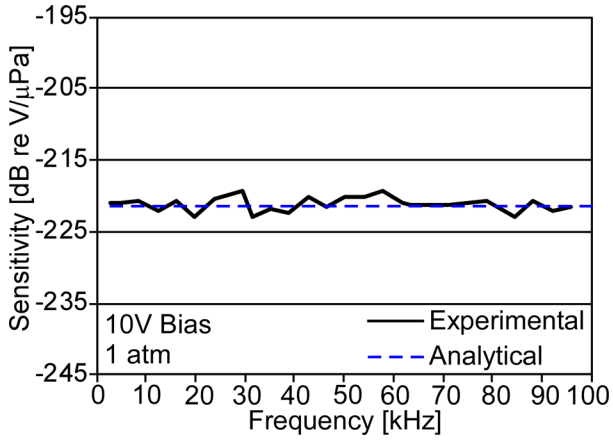

Fig. 4. 34: Hydrophone sensitivity vs. frequency at atmospheric static pressure and 10V bias. The bandwidth was tested up to 100 kHz. This bandwidth is significantly lower than the resonant frequency of any diaphragm, and results in flat response as expected.

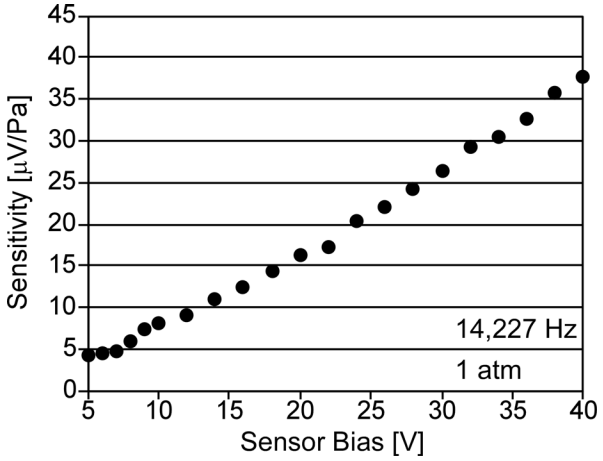

Fig. 4. 35: Impact of sensor bias voltage on acoustic sensitivity. Data was collected using a 14,227 Hz tone at 1 atm static pressure. The curve is mostly linear.

any diaphragm, resulting in a flat response as expected. The sensitivity was experimentally determined to be -221.1 +/- 1.9 dB re V/μPa with a 10V sensor bias. The sensitivity is linearly related to the bias voltage, as is shown in Fig. 4. 35. There is a slight curvature that is from the non-linear nature of variable gap capacitors; however, electrostatic fore is significantly smaller than hydrostatic, meaning there is very little diaphragm, deflection.

4.4.3 High Static Pressure Acoustic Testing

The hydrophone sensitivity at 10V bias and increasing applied static pressure is plotted in Fig. 4. 36. The curve was obtained by recording the measured voltage at each static pressure. Assuming the magnitude of the acoustic signal does not change with static pressure, which is true within a few dB, the voltage change in dB is added to the measured sensitivity at atmospheric pressure. The experimental data is compared to an estimate, which is generated from an approximate slope of the static pressure curve. Both plots show two large peaks in sensitivity, which is from the two largest diaphragms entering transition mode. Both curves show a nearly identical drop in sensitivity vs. applied static pressure above 15 MPa. Both curves

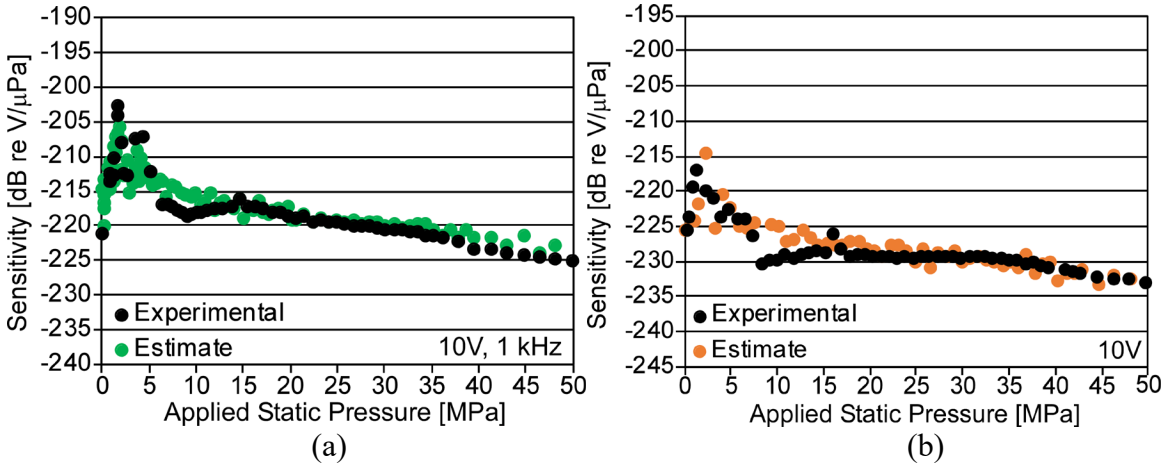

Fig. 4. 36: Hydrophone sensitivity with applied static pressure. The curve is compared to an estimate produced from approximating the slope of the static capacitance response. (a) H106 B1. (b) H106 B5.

show an unexpected drop in sensitivity between approximately 5 and 15 MPa; this is an artifact of the test setup.

4.4.4 MHz Band Testing, 1 atm

Hydrophone bandwidth was demonstrated through pulse – echo measurements at up to 2 MHz frequency. The test setup used to collect this data is presented in Section 4.3.3. The first

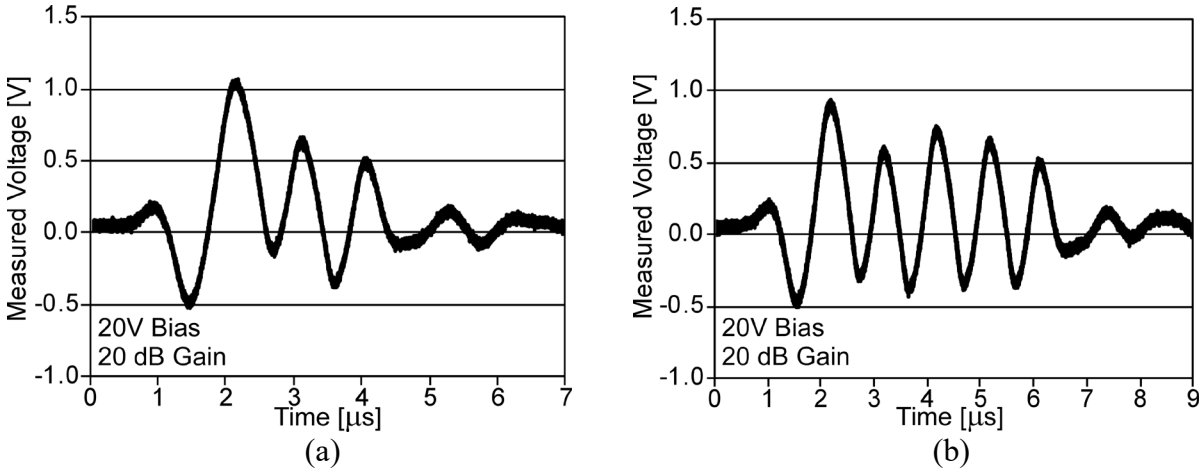

Fig. 4. 37: Pulse – echo test at 1 MHz. Measurements were made with a 20V sensor bias and 20 dB gain through an SR560 preamplifier. Distance was 253 mm from the transmitter. (a) 3 cycle burst. (b) 5 cycle burst.

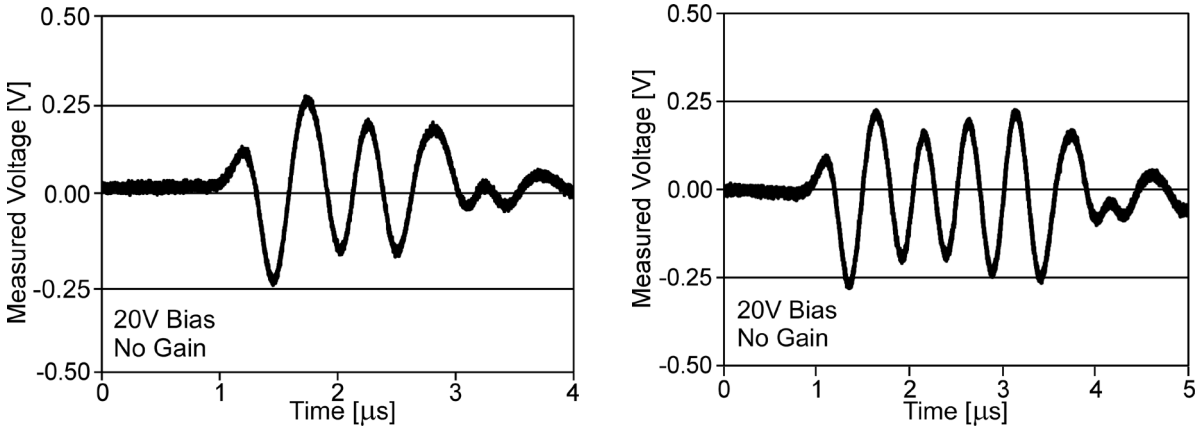

Fig. 4. 38: Pulse – echo test at 2 MHz. Measurements were made with a 20V sensor bias and no gain. Distance was 164 mm from the transmitter. (a) 3 cycle burst. (b) 5 cycle burst.

of these tests is shown in Fig. 4. 37. The piezoelectric transmitter was pulsed for three and five cycles at 1 MHz in (a) and (b), respectively, which each show the measured hydrophone voltage. The curve in (a) shows four peaks, corresponding to three cycles, with the first cycle beginning at under 1 µs. Each peak is 1 µs apart ($T = 1\ MHz^{-1}\ s$), which clearly demonstrates the hydrophone's response into the MHz band. Once the transmitter produces three cycles of acoustic pressure, some transient effects are also measured by the hydrophone. These transient effects are plotted beginning at approximately 4.5 µs. The five-cycle response in (b) shows six peaks, corresponding to five cycles, each peak plotted 1 µs apart. The plot also shows transient pressure beyond approximately 6.5 µs, which is virtually identical to the transient effects in (a). An identical pulse – echo test at 2 MHz is shown in Fig. 4. 38, with three cycles shown in (a) and five cycles shown in (b). The same number of peaks are present in each plot, however, the spacing is approximately 0.5 µs. This corresponds to an acoustic signal of 2 MHz. Both plots once again show virtually identical transient pressures, with (a) occurring beyond approximately 3 µs and (b) occurring beyond approximately 4 µs.

4.4.5 Noise Characterization

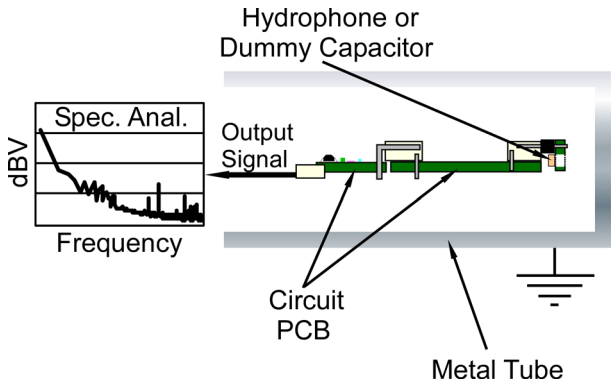

Fig. 4. 39: Test setup for measuring output noise. The circuit PCB and hydrophone are placed inside a grounded metal tube to reduce interference from signals present in the laboratory. The output of the circuit is measured in dBV using a spectrum analyzer.

Hydrophone – circuit electrical noise was characterized using an Agilent 4395A Spectrum/Network/Impedance Analyzer in spectrum analyzer (SA) mode. The circuit and sensor were placed inside a grounded metal tube, as shown in Fig. 4. 39. The noise voltage at atmospheric pressure and increasing sensor bias voltage is shown in Fig. 4. 40, along with the SA noise floor for comparison. The thermal mechanical noise is extremely low due to the hermetic sealing of sensing elements, resulting in no change in noise due to sensor bias voltage. The hydrophone

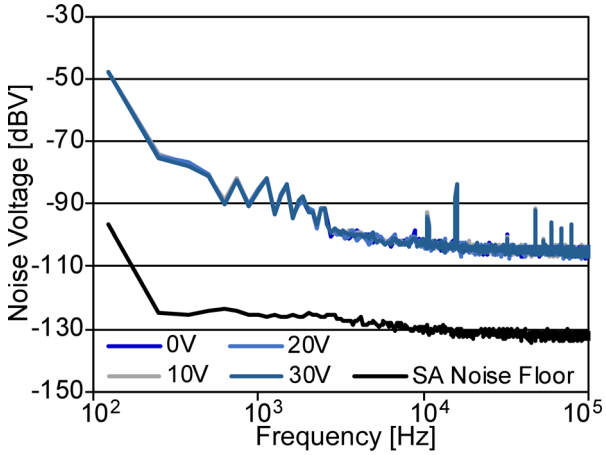

Fig. 4. 40: Measured electrical noise with varying sensor bias. The extremely low thermal mechanical noise is not high enough to surpass electrical noise, resulting in no change due to sensor bias. The spectrum analyzer noise floor is shown for reference.

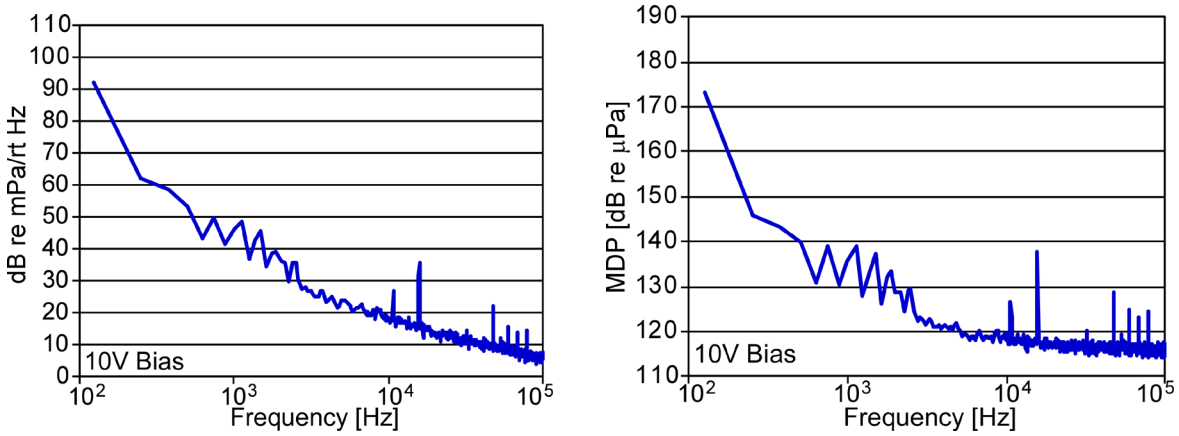

Fig. 4. 41: Pressure data extrapolated from noise voltage in Fig. 4. 40. (a) Equivalent noise pressure spectral density. (b) Minimum detectable acoustic pressure. A 10V bias was assumed in calculations for both figures.

noise curve shows significant spikes; these spikes as well as the jagged response around 1 kHz is due to interference signals present in the lab. These spikes were significantly larger when the tube was not used. The equivalent noise pressure spectral density and the minimum detectable acoustic pressure are shown in Fig. 4. 41. These figures are extrapolated from voltage data in Fig. 4. 40 using equation 4.50.

$$MDP = \frac{Noise\ (Voltage)}{Sensitivity\ \left({}^{Voltage}/_{Pressure}\right)} \tag{4.50}$$

All values are RMS. The sensitivity is taken from 100 kHz calibration results at atmospheric static pressure. A 10V sensor bias is assumed for these calculations. The equivalent noise pressure spectral density is obtained by dividing equation 4.50 by the square root of frequency.

Another noise measurement of interest is the change in noise as static pressure increases. The output voltage is proportional to the ratio of sensor baseline capacitance to circuit feedback capacitor, as explained in Section 4.1. The results are plotted in Fig. 4. 42. The static pressure is emulated through use of dummy capacitors. The largest dummy capacitor is 48 pF, which is larger than the total sensor capacitance of H106 at 50 MPa static pressure, which is usually

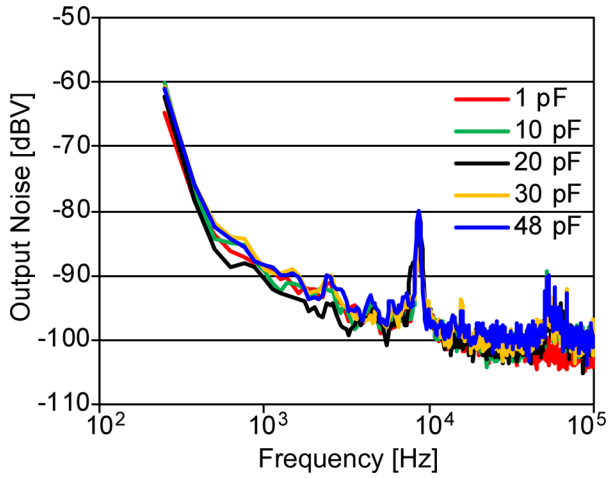

Fig. 4. 42: Measured output voltage with varying dummy capacitor value to emulate the effect of static pressure. The peaks are due to interference signals present in the lab.

around 42 pF. The results show a clear increase in output noise with increasing dummy capacitance value. This effect, however, is quite small with the total increase being less than 3 dBV from 1 pF to 48 pF. The experimental results are much lower than the simulated results; the simulation must be corrected in future work.

4.5 Discussion and Conclusion

The results of Section 4.4 present the full characterization of a surface micromachined heterogeneous hydrophone array. Characterization of the hydrophone is compared to academic and industrial hydrophones in Table 4. 3 and Table 4. 4, respectively. A figure of merit (FOM), γ, is defined for easier comparison.

$$\gamma = \frac{Bandwidth\ (MHZ) \cdot Sensitivity\ \left(^{\mu V}/_{Pa}\right) \cdot Static\ Pressure\ (MPa)}{Size\ (mm^2\ or\ mm^3) \cdot MDP(Pa)} \qquad (4.51)$$

Sensitivity assumes no buffering gain. Academic hydrophones typically focus on chip-level sensor, while industrial hydrophones are packaged. Therefore, the units for γ in the two tables vary slightly. Starting with Table 4. 3, it is quickly noticeable that not all papers presented enough information for calculation of the figure of merit. The optical hydrophone, on the other

.Table 4. 3: Comparison of hydrophones published in academia.

	Sensitivity	Footprint [mm^2]	MDP	BW (demonstrated)	Static Pressure (demonstrated)	γ
Moo10a	-227.5 dB	49	?	100 Hz to 1 kHz	1.5 MPa	N/A
Sul78	-200 dB	N/A (macro)		1 Hz to 1 kHz	4.0 MPa	
Cris09	-202 dB	16	2.5 Pa 1.86 MHz	? to 3.4 MHz	1 atm	
Whi05	-180 dB (in air)	156	7.0 Pa 1 kHz	300 Hz to 15 kHz		
Ber92	-206 dB	?	?	200 Hz to 2 kHz		
Kil11	N/A	28.3	3 mPa 1 kHz	400 Hz to 100 kHz	1 atm, pressure balanced	
Gua12	-180 dB	0.46	0.98 Pa 1 kHz	20 Hz to 2 kHz	1 atm	0.443
This Work	-208.5 dB (40V)	2.24	0.77 Pa 1 kHz	77 Hz to 2.3 MHz	50.0 MPa	2,505

hand, has units of sensitivity of Pa^{-1}, and cannot be easily compared without discarding sensitivity form the figure of merit and only using MDP. Only the piezoresistive hydrophone presented by Guan *et al.* [Gua12], which yields an FOM value of 0.443. This is significantly lower than the heterogeneous hydrophone value of 2,505. The cause of this disparity is the significantly lower bandwidth and static pressure rating. The piezoresistive hydrophone does have a design capable of accommodating static pressure, but there is no demonstration of elevated pressure nor a claim of a depth that can be reached. The extremely wide bandwidth and static pressure rating of the heterogeneous hydrophone prove to be significant factors in FOM.

The industrial hydrophones in Table 4. 4 tend to show better performance than hydrophones in academia, although some of them are very large. Since the heterogeneous hydrophone is not packaged, the size is estimated using the area of the circuit PCB, 1.57 mm thickness of the PCB, and 1 mm on either side to accommodate electrical components and a thin

Table 4. 4: Comparison of hydrophones developed by industry.

	Sensitivity	BW	*Static Pressure	MDP	Size	γ
Benthowave BII-7002	-205 dB	1 Hz to 200 kHz	20 MPa	?	?	N/A
Aquarian Scientific AS-1	-208 dB	1 Hz to 100 kHz	0.2 MPa	?	4,523 mm^3	N/A
Cetacean Research Technology CR3	-207 dB	60 Hz to 180 kHz	9.8 MPa	31.6 mPa 1 kHz	12,723 mm^3	0.196
Ocean Sonics iListen HF	-169 dB	10 Hz to 100 kHz	60 MPa	31.6 mPa 1 kHz	483,152 mm^3	1.39
High Tech, Inc. HTI-94-SSQ	-198 dB	2 Hz to 30 kHz	61 MPa	5.6 mPa 1 kHz	30,561 mm^3	1.35
Bruel & Kjaer Type 8106	-173 dB	7 Hz to 80 kHz	10 MPa	1 Pa 1 kHz	146,373 mm^3	0.0122
This Work	-208.5 dB (40V)	77 Hz to 2.3 MHz	50 MPa	0.77 Pa 1 kHz	742 mm^3	7.57

*Gage pressure

layer of deposited parylene. The FOM value shows that the heterogeneous hydrophone still receives the highest figure of merit, although other hydrophones have a clear advantage in terms of MDP. The closest value of FOM is the Ocean Sonics™ iListen HF hydrophone, which has extremely high sensitivity, excellent bandwidth, and packaging that accommodates up to 60 MPa of static pressure. The MDP is impressively low. The size of the hydrophone, however, hurts its FOM value and is the most obvious area of improvement for this hydrophone.

The work of this chapter has experimentally demonstrated use of the heterogeneous hydrophone as a deep-sea hydrophone as well as a high frequency transducer. The possible applications of this hydrophone are vast; there is no existing hydrophone found that is capable of so many different uses. The distinguishing characteristics are bandwidth, static pressure capability, and size. These characteristics are a result of the unique fabrication process and architecture.

Chapter 5: Conclusions and Future Work

5.1 Summary

The design of a new kind of hydrophone sensor is detailed, along with experimental characterization and demonstration of several applications of interest. Chapter 1 introduces hydrophones and provides background and motivation. Chapter 2 presents a description and characterization of the sensor itself. The chapter begins with a description of the heterogeneous architecture and its design concept. The sensor is fabricated on an insulating sapphire substrate, utilizes 106 sensing elements, and is diced into $1.4 \times 1.6 \times 0.5$ mm^3 chips. Finite element analysis and lumped element modeling is performed. Static pressure response is experimentally verified up to 50 MPa static pressure. Sensor repeatability and usage over time is also demonstrated. The maximum static capacitance change over the 50 MPa range was 34.406 pF. Incremental response was measured up to 3.0 pF/MPa. Electromechanical resonance testing was performed in air and paraffin oil. The first diaphragm resonances are demonstrated to occur in air and oil at 4.105 MHz and 2.319 MHz, respectively. These values match extremely well to the lumped element model.

Chapter 3 details application of the hydrophone to an autonomous microsystem for oil and gas exploration. The millimeter scale (8 mm on a side) microsystems utilize off the shelf electronic components integrated on a flexible printed circuit board and encapsulated in polymer. The hydrophone is integrated with an unpackaged microsystem, which was programmed to measure seismic acoustic signals up to 100 Hz frequency. The seismic signals reached as high as 100 psi (689 kPa) in magnitude. The frequency response is characterized and shown to be

completely flat over the 100 Hz band, as expected. The incremental response vs. static pressure was characterized, along with static response with pressure, static pressure resolution, and MDP at varying static pressure. Above 2 Hz, the MDP was demonstrated to be below 0.1 psi (689 Pa) over almost the entire static pressure range. Lastly, seismic data collection was demonstrated for signals up to 100 Hz.

Chapter 4 explores application as an ultrasonic transducer and a deep-sea hydrophone. The hydrophone is experimentally calibrated in paraffin oil at atmospheric pressure up to 100 kHz (-221 +/-1.9 dB re V/μPa, 10V bias). The response is completely flat, as expected. The sensitivity vs. applied static pressure at 1 kHz is characterized up to 50 MPa applied static pressure. This information is representative of the flat band response, which increases when static pressure is applied. Next, hydrophone response up to 2 MHz frequency was demonstrated using a pulse-echo technique at atmospheric pressure. Noise and MDP were characterized at atmospheric pressure and were found to be 0.92 μV/√Hz and 24.5 mPa/√Hz (40V bias) at 1 kHz, respectively.

5.2 Contributions

The main contributions of this work include the following:

1. Designed and developed a disruptive type of hydrophone that is compatible with autonomous microsystems.
2. Modeled and experimentally verified the extremely wide frequency response afforded by a heterogeneous architecture.
3. Demonstrated repeatability and response change over time for arrayed sensing elements developed in a custom surface micromachining process.

4. Modified existing microsystem programming to measure seismic signals up to 100 Hz frequency. Integrated the H106 hydrophone with a microsystem and demonstrated static performance up to 50 MPa and dynamic (seismic) performance with acoustic signals up to 100 psi in magnitude.
5. Developed and experimentally verified a custom charge amplifier circuit with bandwidth from 77 Hz to 8.9 MHz.
6. Experimentally characterized the hydrophone for use as an ultrasonic transducer as well as a deep-sea hydrophone. A full calibration curve from 1 kHz to 100 kHz was produced at atmospheric pressure, yielding flat sensitivity of -221 +/-1.9 dB re V/μPa (10V bias). The flat band sensitivity as a function of static pressure up to 50 MPa was also produced. Response time was demonstrated through measurements of acoustic signals up to 2 MHz frequency. Lastly, noise was characterized to show MDP as low as 24.5 mPa/√Hz (40V bias) at 1 kHz.

5.3 Future Work

5.3.1 High Pressure Test Setup with Increased Bandwidth

The high-pressure acoustic apparatus in this work was bandwidth limited and not capable of providing acoustic data at high static pressures as well as high frequency. Additionally, correlated double sampling should be implemented to help mitigate the drift encountered in sensitivity vs. static pressure data. The combined stack-plate-vessel system was predicted to have a fundamental resonance at approximately 9.3 kHz, at which frequency major damage to the stack actuator could take place. The stack actuator alone can only provide up to 20 kHz bandwidth. Given the extremely wide flat band of the H106 hydrophone, any resonance evident

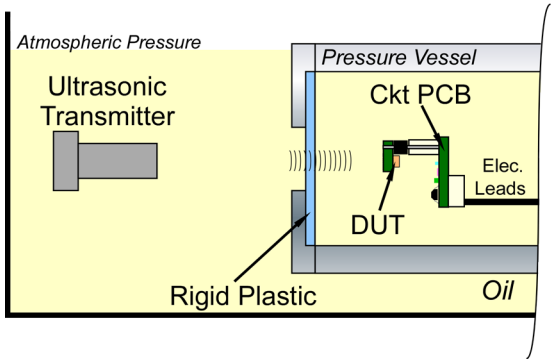

Fig. 5. 1: Proposed high-pressure acoustic test setup for high frequency measurements. A rigid plastic with similar acoustic impedance to oil is used as a sidewall of the pressure vessel and is designed to be acoustically transparent. The readout circuit is integrated inside the pressure vessel to reduce interference.

in the hydrophone response would be without doubt an artifact of the test setup. Increasing the bandwidth of the test setup reveals more information about the hydrophone and facilitates the generation of acoustic cavitation, which is another item of interest. An acoustic source that is inside or in contact with the pressure vessel will be limited in frequency and capability. A new high-pressure acoustic test setup is proposed with this consideration in mind.

The proposed test setup is presented in Fig. 5. 1. The figure shows an acoustic transmitter and pressure vessel submerged in oil. The pressure vessel is also filled with oil. One wall of the pressure vessel is composed of a rigid plastic material with acoustic impedance similar to that of the oil. This rigid plastic wall can be designed to be acoustically transparent. In this configuration, any type of acoustic transmitter can be used without consideration of performance under high static pressure or the change in performance from mechanical interactions with the pressure vessel components. This greatly increases options of equipment, which in turn allows for much wider frequency response. Furthermore, high frequency pulse-echo testing is now a possibility; such testing eliminates problematic electrical interference signals generated to drive the transmitter. The last addition is integration of the readout circuit inside the pressure vessel. Electrical feedthrough from the circuit to the sensor has proven to be

problematic due to interactions with the pressure vessel at the sensor input node. The pressure vessel behaves as an antenna regardless of the grounding scheme.

Preliminary design of the plastic barrier can be performed using analytical calculation of the barrier intensity transmission coefficient, T_I. Kinsler *et al.* [Kin82] describe T_I through a thin barrier with the proposed configuration as

$$T_I = \frac{1}{1 + \frac{1}{4}\left(\frac{z_p}{z_o} - \frac{z_o}{z_p}\right)^2 \sin^2 k_p L}, \tag{5.1}$$

where z_p is acoustic impedance of the plastic barrier, z_o is acoustic impedance of the oil, k_p is wave number in plastic ($k_p = \omega/c_p$), and L is the barrier thickness. The equation assumes plane waves. Since the incident and transmitted areas are identical, T_I can be thought of as a power transfer coefficient. Equation 5.1 shows that for any acoustic impedance, the transfer coefficient is unity at low frequency. At a critical frequency, the sine term in the denominator will eventually surpass unity value and lower the transmission coefficient. Beyond this frequency, the coefficient oscillates proportionally to $\sin^{-2} k_p L$. To eliminate T_I's dependence on frequency, the acoustic impedance of oil and plastic should be as close as possible.

Calculations were performed on low density polyethylene due to its acoustic impedance, low cost, availability, and sufficient rigidity. Table 5. 1 shows material properties for oil and LDPE. Results are plotted in Fig. 5. 2 with varying wall thickness, L. The critical frequency for each curve is around or below 10 kHz, with thicker walls trending towards lower frequency. Once the critical frequency is surpassed for all curves, the transmission coefficient oscillates between 0

Table 5. 1: Acoustic properties of oil and LDPE. See Appendix A for oil characterization.

	Enerpac™ LX101 paraffin oil [Ene18]	Low Density Polyethylene (LDPE) [Sel85]
Density	850 kg/m^3	920 kg/m^3
Speed of Sound	1400 m/s	1950 m/s
Acoustic Impedance	1.19 MRayls	1.79 MRayls

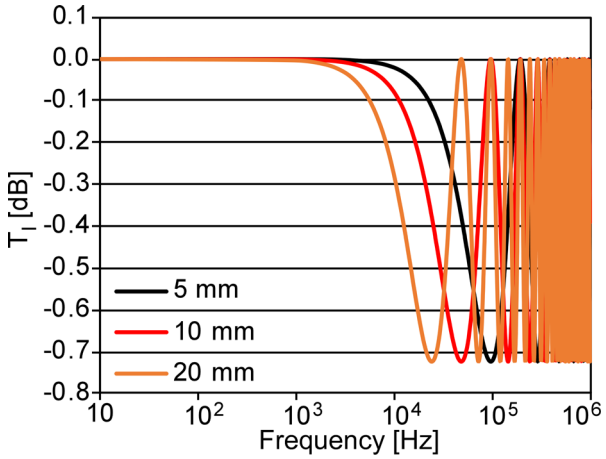

Fig. 5. 2: Analytical intensity transmission coefficient through LDPE with varying wall thickness. The LDPE acoustic impedance results in extremely low losses over a wide frequency band.

dB and -0.7 dB, the latter of which is attributed to the slight impedance mismatch between oil and LDPE. The oscillation continues well past 1 MHz (not shown). This preliminary investigation describes a new acoustic setup for high pressure acoustic testing up to MHz frequencies. Further investigation must be done to identify losses that could occur, including dispersion inside the plastic.

5.3.2 Application to Deep-Sea, High Resolution SONAR

In addition to satisfying requirements for use in autonomous microsystems, the miniature form factor, wide bandwidth, and high static pressure rating shows great promise for application to high resolution SONAR. The millimeter scale chips can be arrayed to provide high resolution images with an unparalleled combination of form factor, bandwidth, and ocean depth capability. An illustration of such an array is shown in Fig. 5. 3, which includes 36 chips for a total size of less than 1 cm on a side. The challenges associated with developing such a system include lead transfer, digital signal processing, and chip alignment, to name a few.

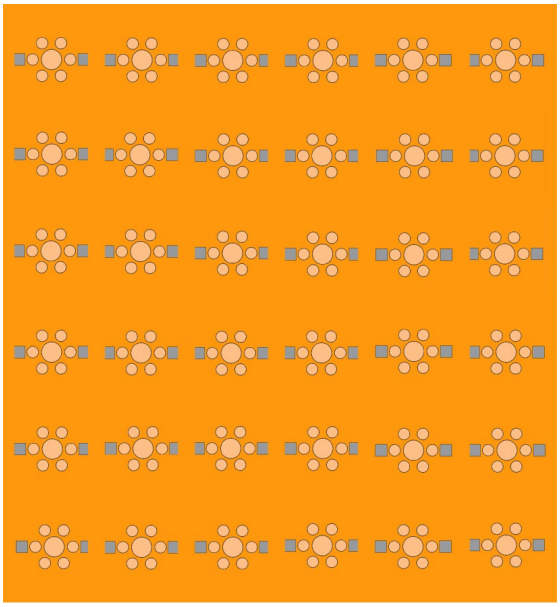

Fig. 5. 3: Individual chips can easily be arrayed for resulting deep-sea, high resolution SONAR. The array can provide unparalleled form factor, bandwidth and ocean depth.

The considerations for designing a heterogeneous array for deep-sea, high resolution SONAR are different than for use in an autonomous microsystem. For example, the baseline capacitance for use in a microsystem is much more important because readout is done with a capacitance to digital converter (CDC). The charge amplifier circuit is chosen because it accommodates large baseline; for this reason, larger sensing elements can be implemented on the hydrophone chips to increase higher sensitivity without degrading readout capability. Larger diaphragms can drastically improve sensitivity at the cost of linearity and baseline capacitance; the output noise of the readout circuit changes linearly with baseline capacitance while the sensitivity increases non-linearly. This results in a net improvement in MDP. Other process improvements would include a thickening of the electrode insulation layer to reduce pull-in voltage for bandwidth tuning capability. The array can also be fabricated on a single chip with more electrical leads, which eliminates chip alignment concerns and significantly reduce form factor.

5.3.3 Addition of Static Response to Ultrasonic Sensing

The charge amplifier used for readout implements a feedback loop that includes a high pass filter. The readout circuit is described in Chapter 4 and shown again in Fig. 5. 4. A finite resistance is used for the feedback resistor to allow for charge and therefore potential to equalize over the feedback components; this DC biasing is a requirement for the op amp. Unfortunately, it does not afford static sensing. For static sensing capability, this circuit could be implemented as a true charge integrator, similar to a switched capacitor charge integrator [Gia06]. The feedback resistor can be replaced with a switch that can be used to tune the low frequency response and even enable static sensing. For higher frequency operation, the switch can be biased to perform like R_F in Fig. 5. 4. For static and low frequency operation, special considerations come into play for the switch timing and sensor bias, as is explained in [Gia06].

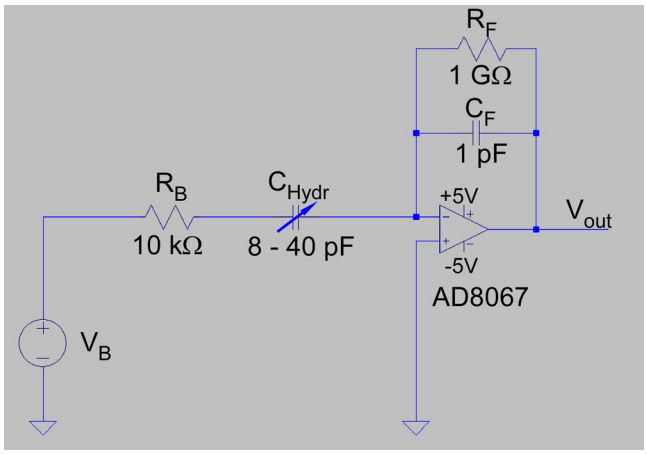

Fig. 5. 4: Charge amplifier readout circuit.

Appendices

Appendix A: Oil Characterization

Experimental speed of sound measurements were made in Enerpac® LX-101 oil (1400.49 m/s +/- 6.59 m/s), white mineral oil (1391.26 m/s +/- 8.39 m/s), and XIAMETER® PMX-200 10 cSt silicone oil (972.97 m/s +/- 4.63 m/s). The LX-101 oil, which is 99% paraffin oil, matches closely to published values for pure paraffin oil. The white mineral oil is slower than the published value; however, there is no detail of the exact brand of mineral oil tested. The data in [Sel85] was from a different brand likely with higher viscosity. The measurement for the silicone oil matches extremely will to data published in [Sel85] of the exact same brand and model of oil. In fact, the published value lies within the measurement uncertainty. The fluids tested are displayed in Table A. 1, along with known specifications. The most cited literature for acoustic measurements in isotropic materials is presented by Selfridge [Sel85].

Table A. 1: Published values for fluids tested in Appendix A.

	LX-101 [Ene18]	White Mineral Oil [Ste18]	PMX-200 Silicone Oil [Kra19]
Manufacturer	Enerpac®	STE Oil Company, Inc.	Krayden (Dow Corning
Density	0.855 g/cc	0.860 g/cc	0.940 g/cc
Viscosity	15 cSt	12.32 cSt	10 cSt
Color	Yellow	Clear (White)	Clear
Measured Speed of Sound	1400.49 +/-6.95 m/s	1391.26 +/- 8.39 m/s	972.97 +/- 4.63 m/s
Published Speed of Sound	*1420 m/s [Sel85]	1440 m/s [Sel85]	968 m/s [Sel85]
Notes	99% paraffin oil	Generic	Excellent match to literature

*Value given for 100% paraffin oil, while LX-101 is 99% paraffin oil

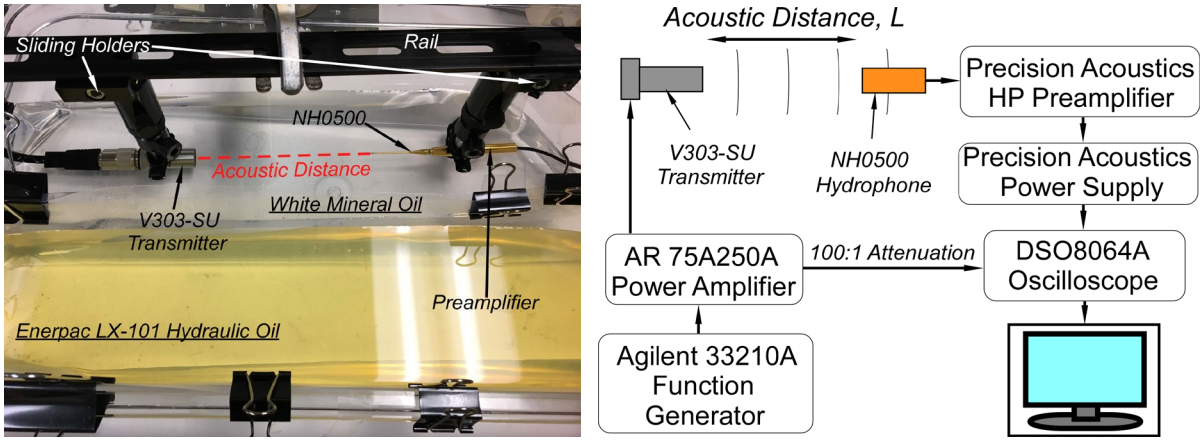

(a) (b)

Fig. A. 1: Acoustic testing setup. (a) Optical image of the test setup. (b) Block diagram of the test setup and methods.

Experimental speed of sound measurements in liquid are performed through acoustic time of flight measurements. This involves placing an acoustic transmitter a fixed distance away from a reference hydrophone and measuring how long an acoustic signal takes to reach the hydrophone. Of course, both the transmitter and hydrophone are immersed in the fluid of interest.

An optical image of the experimental test setup is shown in Fig. A. 1(a). An Olympus Panametrics V303-SU immersion transducer is used as an acoustic transmitter, and is immersed opposite a Precision Acoustics, Inc. NH0500 needle hydrophone. The equipment is submerged in fluid and held a fixed distance apart by sliding holders that are fixed to a rail. The holders can slide freely along the rail or be tightened to stay in place. The bottom side of the rail (not pictured) has tick marks to aid in measurement of the acoustic distance, L. The acoustic distance is the distance the acoustic signal must travel between the transmitter and hydrophone; an accurate measurement is critical to this work.

A flow diagram of the test setup is shown in Fig. A. 1(b). A 900 kHz pulse signal is created using an Agilent 33210A function generator, which is fed into an Amplifier Research ®

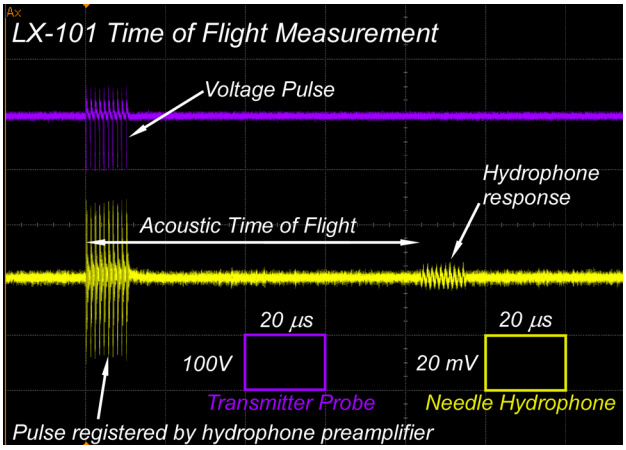

Fig. A. 2: Waveforms from a single time of flight measurement in LX-101 oil. The hydrophone preamplifier reacts to the pulse signal, acquired through shared power lines and/or electromagnetic interference. The needle hydrophone registers an acoustic response approximately 84.5 μs after the pulse.

75A250A power amplifier. The power amplifier drives the V303-SU immersion transducer, which creates acoustic waves that are proportional to the pulsed signal. The pulsed signal is not more than 10 cycles to eliminate measurement of reflections within the oil. The 900 kHz driving frequency was chosen based on the resonant frequency of the transmitter. The NH0500 needle hydrophone measures the acoustic signal. An electrical signal is created that is amplified by a Precision Acoustics HP model preamplifier, which then feeds through a power supply. The power supply removes any DC component that may exist in the signal. The power supply feeds into an Agilent DSO8064A oscilloscope for measurement. Data is then saved and analyzed on a personal computer.

Once the pulse-response measurements are recorded, the data are converted to a .csv file and uploaded to a personal computer. A typical waveform is shown in Fig. A. 2. The voltage pulse (purple) is measured and recorded, along with the signal obtained from the reference hydrophone (yellow). Notice that the reference hydrophone registers the pulse applied to the transmitter. This is due to shared power lines between the preamplifier and the power amplifier. After the transmitter is excited at time $t = 0$, the hydrophone registers an acoustic signal at $t = t_{ac}$,

where t_{ac} is the acoustic time of flight. From the acoustic time of flight and the acoustic distance, the speed of sound, c, in a fluid can be determined using equation A1.

$$c = \frac{L}{t_{ac}} \tag{A1}$$

Testing results are shown in Table A. 2, along with some testing parameters. The number of measurements refers to how many times the acoustic time of flight was measured; Fig. A. 2 shows a single measurement. The measurement uncertainty is simply the standard deviation of the derived speed of sound from each measurement. Lastly, the uncertainty due to L measurements, U_L, is calculated using equation A2.

$$U_L = \frac{0.5\ mm}{L} c_{avg} \tag{A2}$$

The *0.5 mm* is the estimated error (+/-) in measurement of L. Results show that the LX-101 oil has a speed of sound of 1400.49 m/s +/- 6.59 m/s, while the white mineral oil has a speed of sound of 1391.26 m/s +/- 8.39 m/s. The measurement acquired from white mineral oil was compared to published values in [Sel85]. The measured value had a percent error of 3.38%.

All measurement data and uncertainties for the measured oils are shown in Table A. 2. The value for LX-101 matches closely to comparable liquids published in [Sel85]. The value for silicone oil matches extremely closely to the published value; in fact, the published value falls within the total measurement uncertainty. The oil tested is the exact oil published in [Sel85], down to the company and model. The generic white mineral oil has a 3.38% error to the value in [Sel85]. This is a higher error than expected.

While it is bothersome that the measurement for white mineral oil does not completely agree with literature, this does not mean that the measurement is incorrect. The data presented in [Sel85] does not state the viscosity of the mineral oil. It is likely that Selfridge's sample had a

Table A. 2: Measurement results.

	LX-101	White Mineral Oil	PMX-200
Acoustic Distance (L)	117.0 mm +/- 0.5 mm	131.0 mm +/- 0.5 mm	119.5 mm +/- 0.5 mm
Temperature	25.4 °C	25.1 °C	24.0 °C
Number of Measurements	10	9	10
Average Speed of Sound	1400.49 m/s	1391.26 m/s	972.97 m/s
Measurement Uncertainty	+/- 0.61 m/s	+/- 3.08 m/s	+/- 0.56 m/s
Uncertainty due to L Measurement	+/- 5.99 m/s	+/- 5.31 m/s	+/- 4.07 m/s
Total Uncertainty	+/- 6.59 m/s	+/- 8.39 m/s	+/- 4.63 m/s
Relative Uncertainty	+/- 0.47%	+/- 0.60%	+/- 0.47%
Literature Value	*1420 m/s [Sel85]	1440 m/s [Sel85]	968 m/s [Sel85]
% error	1.37%	3.38%	0.51%

*Value given for 100% paraffin oil, while LX-101 is 99% paraffin oil

higher viscosity characteristic, which typically results in higher measured speed of sound. Selfridge does not state the viscosity of his sample.

Appendix B: Electromagnetic Interference Issue

Significant issues were encountered during HP acoustic testing due to electromagnetic interference. This interference was caused by the voltage signal applied over the stack actuator, and as a result is at the exact frequency of the acoustic signal to be measured. This is illustrated in the block diagram in Fig. B. 1. The electromagnetic signal is emitted from the wire connecting the buffer to the stack actuator. Many different shielding techniques were considered, with little success. Some of these shielding schemes are presented in Fig. B. 2.

The most successful scheme was shield scheme 1. There was no apparent repeatable dependency of interference on any particular shielding. Fig. B. 2(d) shows shield scheme 4, in which the electrical leads to the sensor are fed through a grounded metal tube; surprisingly, this was the worst shielding scheme attempted. For most tests, shielding scheme 1 was used.

The grounding used for all shielding schemes is shown in Fig. B. 3. The circuit ground was connected to the ground for the buffer, signal generator, and stack actuator. The system ground, shown in the bottom right corner of Fig. B. 3, is the same ground used in all shield schemes of Fig. B. 2.

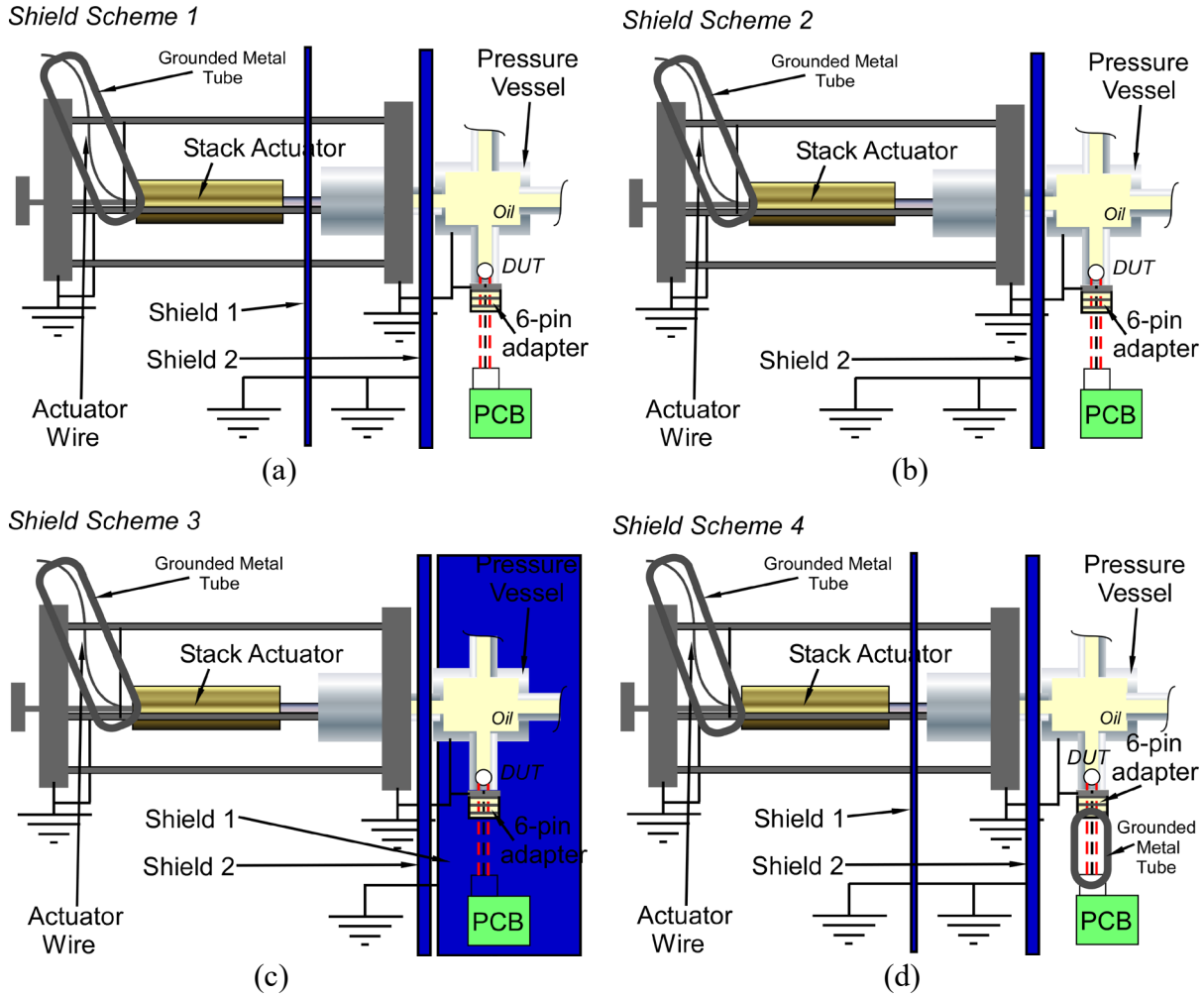

Fig. B. 2: Grounding schemes used in HP acoustic testing. All schemes utilize multiple ground loops on the test apparatus as well as a grounded metal vacuum tube around the stack actuator wire. (a) Scheme 1: two grounded shields. (b) Scheme 2: one grounded shield. (c) Scheme 3: shield 1 is moved to the right of the circuit and leaned on its side to shield the top and side of the circuit. (d) Scheme 4: a grounded tube is placed around the feed-through wires.

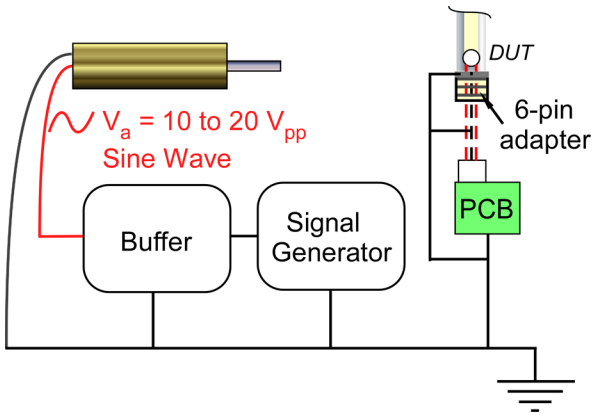

Fig. B. 3: Grounding scheme. All electrical components are connected to the same ground, which is that of the circuit. The interference signal is much larger if this is not the case.

Apparent Dependence on Static Pressure

The interference signal has an apparent dependence on static pressure. Since the sensor input node is intimately in contact with the test setup, it is likely that some aspect (such as parasitic capacitance, resistance, etc.) of the test setup changes with static pressure, which affects how the circuit reacts to the signal at the sensor input node. This is illustrated in Fig. B. 4. Here, the sensor bias is set to 0V. The spectrum of the signal obtained from the readout circuit is plotted up to 2 kHz. Fig. B. 4(a) shows the spectrum at a static pressure of 0.791 MPa while (b)

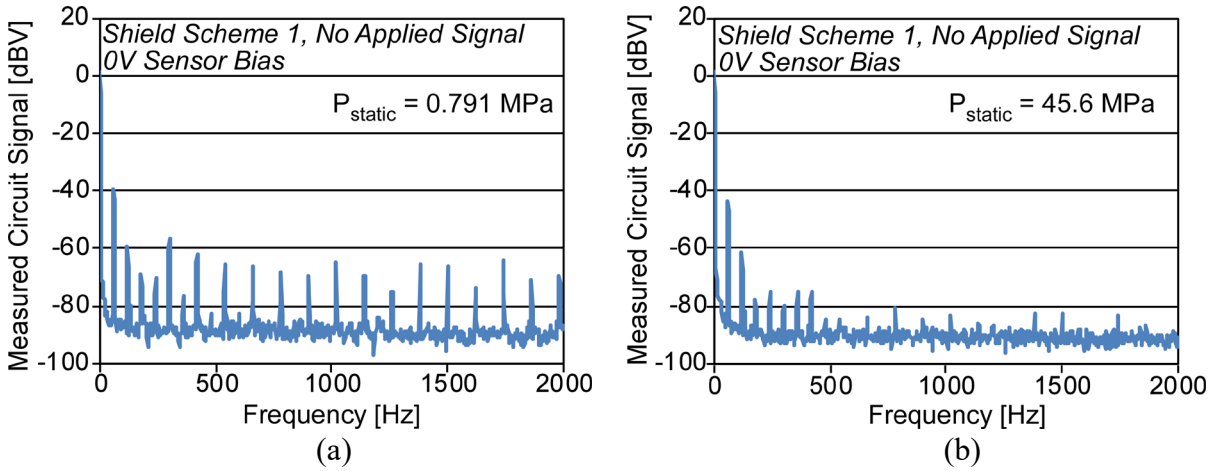

Fig. B. 4: Circuit reading at two separate static pressures. Peaks are interference form random electrical signals present in the lab. There is a clear change in measured signal, dependent on the static pressure. (a) 0.791 MPa static pressure. (b) 45.6 MPa static pressure.

shows the spectrum at 45.6 MPa. The peaks in signal in both plots are random signals that are present in the lab; they are interference signals, but they are not from the piezo stack because the stack is not being driven. Fig. B. 4(b) shows a dramatic reduction in interference peaks when compared to (a). Since there is no applied signal, it is safe to assume that the prominence of any interference signal is dependent on the static pressure inside the vessel.

Further investigation was performed to show exactly how the interference signal changes with static pressure. Fig. B. 5 shows two separate trials. The sensor bias was set to 0V and the piezo stack was driven with a 20 V_{pp} sine wave at 1 kHz. The signal from the readout circuit was measured and recorded using a spectrum analyzer. Fig. B. 5(a) shows the first trial. A similar drop in signal is seen at approximately 5 MPa, then rises to a constant rate by about 10 MPa. Trial 2 was performed with the exact same procedure and no change in setup only several minutes after Trial 1. Trial 2 shows a different curve, although the characteristic drop in signal is also seen. The drop occurs at around 12 MPa and reaches a steady level by 25 MPa. Fig. B. 6 shows an identical procedure, but with shield scheme 2 implemented. The drop is seen, but with

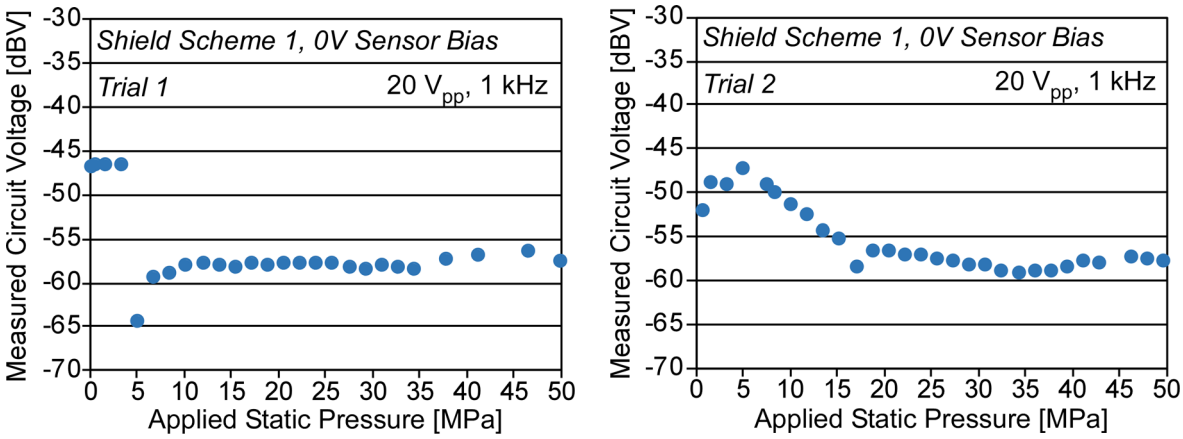

Fig. B. 5: Two separate measurements of the interference signal using shield scheme 1. There was absolutely no change in scheme or procedure between the two trials. (a) Trial 1. The characteristics drop on signal is clearly seen. (b) Trial 2. There is a drop in signal, but the magnitude and shape are not the same as in Trial 1. This reveals how the setup non-ideality is not repeatable.

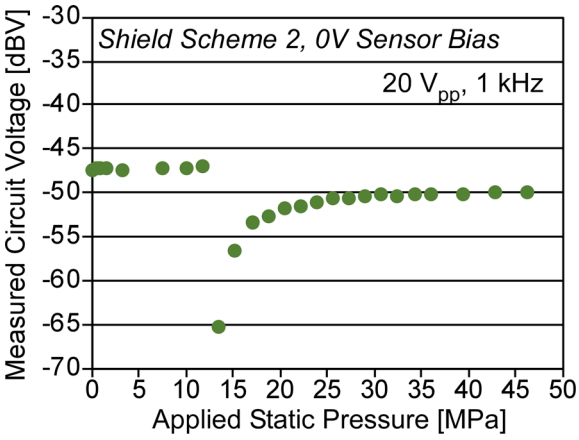

Fig. B. 6: *Repetition of Fig. B. 5 using shield scheme 2. The characteristic drop in signal is seen, but at different magnitude and slightly different static pressure.*

different magnitude and slightly different static pressure. The plots in Fig. B. 5 and Fig. B. 6 illustrate that any signal measured by the readout circuit has some dependence on the static pressure that is not related to the sensor performance. The plots also reveal that this dependence is not repeatable and cannot be accurately predicted.

Interference Relationship to Frequency and Voltage

The measured interference signal showed relationships to frequency and voltage level applied to the stack actuator. The measured signal from a $10V_{pp}$ sine wave at different frequencies

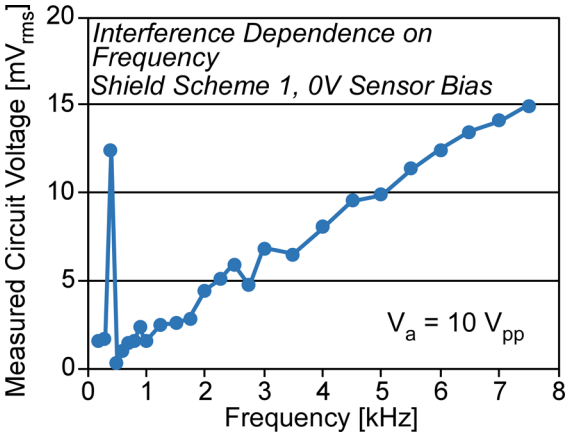

Fig. B. 7: Measured interference signal vs. driving frequency. The sensor is set to 0V bias so that the measured signal is only from the interference generated by the stack driver.

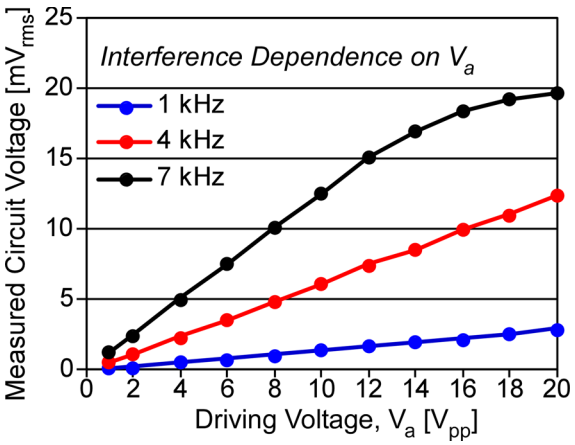

Fig. B. 8: Dependence on stack driving signal, V_a. Each curve represents measurements at a different frequency. The relationship with driving voltage is very linear at 1 and 4 kHz, while the 7 kHz curve appears mostly linear until reaching near 20Vpp.

is shown in Fig. B. 7. Shield scheme 1 is utilized. The curve shows a resonance in measured signal at 400 Hz, followed by a significant drop in signal at 500 Hz. Beyond 500 Hz, the signal appears to have a linear relationship with frequency. This characteristic implies that the interference signal is inducing a current at the circuit input node. An induced current should scale linearly with frequency. Fig. B. 7 also shows that the interference is extremely large and reaches all the way to approximately 15 mV_{rms} at 8 kHz. This makes measurement of acoustic signals virtually impossible due to the signal magnitude requirement to overcome the interference signal.

Next, the relationship between interference signal and stack driving voltage, V_a, was studied (Fig. B. 8). The relationship is highly linear at 1 and 4 kHz. The curve at 7 kHz is mostly linear, until beginning a trend to saturation at around 12Vpp.

References

[Amb10] D. Ambika, V. Kumar, H. Imai, and I. Kanno, “Sol-gel deposition and piezoelectric properties of {110}-oriented Pb(Zr0.52Ti0.48)O3 thin films,” *Applied Physics Letters*, 96, 031909, 2010.

[Aka01] O. Akar, T. Akin, and K. Najafi, “A wireless batch sealed absolute capacitive pressure sensor,” *Sensors and Actuators A: Physical*, vol. 95, pp. 29-38, 2001.

[An13] S. An, N. Gupta, and Y. Gianchandani, “Vacuum sealing using atomic layer deposition of Al2O3 at 250ºC,” *Journal of Vacuum Science & Technology A*, vol. 32, no. 1, 2013.

[Ana19] *High Gain Bandwidth Product, Precision FastFET Op Amp Datasheet, AD8067*, Analog Devices, Norwood, MA, 2019.

[Bag06] P.E. Bagnoli, N. Beverini, R. Falciai, E. Maccioni, M. Morganti, F. Sorrentino, C. Trono, “Development of an erbium-doped fibre laser as a deep-sea hydrophone,” *Journal of Optics A: Pure and Applied Optics*, vol. 8, pp. S535-S539, 2006.

[Bay13] A.M. Cetin and B. Bayram, “Diamond-based capacitive micromachined ultrasonic transducers in immersion,” *IEEE Transactions on Ultrasonics, Ferroelectrics, and Frequency Control*, vol. 60, no. 2, February 2013.

[Ben19] A. Benken, “A High-Yield Microfabrication Process for Sapphire Substrate Pressure Sensors with Low Parasitic Capacitances and 200°C Tolerance,” Ph.D. dissertation, University of Michigan, 2019.

[Ber92] J. Bernstein, "A micromachined condenser hydrophone," *Technical Digest IEEE Solid-State Sensor and Actuator Workshop*, Hilton Head Island, SC, USA, pp. 161-165, 1992.

[Bil93] N. Bilaniuk and G.S.K Wong, “Speed of sound in pure water as a function of temperature” *Journal of the Acoustical Society of America, vol. 93*, 1993.

[Bil97] N. Bilaniuk, “Optical microphone transduction techniques,” *Applied Acoustics*, vol. 50, no. 1, pp. 35-63, 1997.

[Bjø13] L. Bjørnø, “Developments in sonar technologies and their applications,” *2013 IEEE International Underwater Technology Symposium (UT)*, Tokyo, pp. 1-8, 2013.

[Cha01] A.V. Chavan and K.D. Wise, “Batch-processed vacuum-sealed capacitive pressure sensors,” *Journal of Microelectromechanical Systems*, vol. 10, no. 4, December 2001.

[Cha02] A.V. Chavan and K.D. Wise, “A monolithic fully-integrated vacuum-sealed CMOS pressure sensor,” *IEEE Transactions of Electron Devices*, vol. 49, no. 1, 2002.

[Cha12] D. Chapman and W. Trybula, “Meeting the challenges of oilfield exploration using intelligent micro and nano-scale sensors,” in *12th IEEE International Conference on Nanotechnology*, Birmingham, UK, 2012.

[Cha87a] H. Chau, K. D. Wise, “Noise due to Brownian motion in ultrasensitive solid-state pressure sensors,” *IEEE Transactions on Electron Devices*, vol. ED-34, no. 4, pp. 859–865, April 1987.

[Cha87b] H. Chau, K. D. Wise, “Scaling limits in batch-fabricated silicon pressure sensors,” *IEEE Transactions on Electron Devices*, vol. ED-34, no. 4, pp. 850–858, April 1987.

[Che80] P.L Chen, R.S. Muller, R.M. White, and R. Jolly, “Thin film ZnO-MOS transducer with virtually DC response,” *Ultrasonics Symposium*, pp. 945-948, 1980.

[Che09] A. Cheng, “Design of a readout scheme for a MEMS microphone,” PhD Thesis, Delft University, 2009. 64

[Cho17] M. Choi, Y. Sui, R. Meredith, Y. Ma, G. Kim, D. Blaauw, Y.B. Gianchandani, and T. Li, “Autonomous microsystems for downhole applications: design challenges, current state, and initial test results,” *Sensors*, vol. 17, 2190, 2017.

[Cian06] Cianci E., Foglietti V., Minotti A., Caronti A., Caliano G., Pappalardo M. (2006) *Fabrication Techniques in Micromachined Capacitive Ultrasonic Transducers and their Applications*. In: Leondes C.T. (eds) MEMS/NEMS. Springer, Boston, MA

[Col98] A.J. Coleman, E. Draguioti, R. Tiptaf, N. Shotri, J.E. Saunders, “Acoustic performance and clinical use of a fibreoptic hydrophone,” *Ultrasound Med Biol*, vol. 24, no. 1, pp.143-151, 1998.

[Cra03] G. A. Cranch, P. J. Nash and C. K. Kirkendall, "Large-scale remotely interrogated arrays of fiber-optic interferometric sensors for underwater acoustic applications," *IEEE Sensors Journal*, vol. 3, no. 1, pp. 19-30, Feb. 2003.

[Cris09] P. Cristman, Ö. Oralkan, X. Zhuang, T.-J. Ma, S. Vaithilingam, T. Carver, I. Wygant, and B.T. Khuri-Yakub, “A 2D CMUT hydrophone array: characterization results,” *2009 IEEE International Ultrasonics Symposium Proceedings*, Rome, pp.992-995, 2009.

[Dae16] V. Daeichin, C. Chen, Q. Ding, M. Wu, R. Beurskens, G. Springeling, E. Noothout, M.D. Verweij, K.W.A. van Dongen, J.G. Bosch, A.F.W. van der Steen, N. de Jong, M. Pertijs, and G. van Soest, “A broadband polyvinylidene difluoride-based hydrophone with integrated

readout circuit for intravascular photoacoustic imaging," *Ultrasound in Medicine and Biology*, vol. 42, no. 5, pp. 1239-1243, 2016.

[Dow15] D.R. Dowling and K.G. Sabra, "Acoustic remote sensing," *Annual Review of Fluid Mechanics*, vol. 47, no. 1, pp. 221-243, 2015.

[Ell07] D. Ellis and J. Singer, *Well Logging for Earth Scientists*. Springer, 2007.

[Ene18] Enerpac, LX101 product page, <https://www.enerpac.com/en-us/hydraulic-oil/oil/LX101> Visited December 16, 2018.

[Erg03] A.S. Ergun, G.G. Yarioglu, and B.T. Khuri-Yakub, "Capacitive micromachined ultrasonic transducers: theory and technology," *Journal of Aerospace Engineering*, vol. 16, no. 2, pp. 76-84, 2003.

[Far92] A. Fartash, I.K. Schuller, M. Grimsditch, "Thin-film modeling for mechanical measurements: Should membranes be used or plates?" *Journal of Applied Physics*, vol. 71, no. 9, 1992.

[Fil90] L. Filipczynski and J. Etienne, "Capacitance hydrophones for pressure determination in lithotripsy," *Ultrasound Med Biol*, vol. 16, no. 2, pp. 157-165, 1990.

[Fin10] J. Finger and D. Blankenship, "Handbook of best practices for geothermal drilling," Sandia Nat. Labs., Albuquerque, NM, USA, and Livermore, CA, USA, Dec. 2010.

[Gab93] T.B. Gabrielson, "Mechanical-thermal noise in micromachined acoustic and vibration sensors," *IEEE Transactions on Electron Devices*, vol. 40, no. 5, pp. 903-909, 1993

[Gan18] B.A. Ganji, M.S. Nateri, and M. Dardael, "Design and modeling of a novel high sensitive MEMS piezoelectric vector hydrophone," *Microsystem Technologies*, Springer, 2018.

[Gia06] Y.B. Gianchandani, C. Wilson, and J.-S. Park, "Micromachined Pressure Sensors: Devices, Interface Circuits, and Performance Limits" in *The MEMS Handbook, 2nd Edition,* ed. M. Gad-el-Hak, CRC Press, pp. 3.1-3.44, 2006.

[Gra89] B. Granz, "PVDF hydrophone for the measurement of shock waves," *IEEE Transactions on Electrical Insulation*, vol. 24, no. 3, 1989.

[Gua12] L. Guan, G. Zhang, J. Xu, C. Xue, W. Zhang, and J. Xiong, "Design of T-shape vector hydrophone based on MEMS," *Sensors and Actuators A: Physical*, vol. 188, pp. 35-40, 2012.

[Hal94] M.I. Haller and B.T. Khuri-Yakub, "A surface micromachined electrostatic ultrasonic air transducer," *Proceedings of IEEE Ultrasonics Symposium*, pp. 1241-1244, 1994.

[Han04] S.T. Hansen, A.S. Ergun, W. Liou, B.A. Auld, B.T. Khuri-Yakub, "Wideband micromachined capacitive microphones with radio frequency detection," *Journal of the Acoustical Society of America*, vol. 116, no. 2, August 2004.

[Har88] G. Harris, "Hydrophone measurements in diagnostic ultrasound fields," *IEEE Transactions on Ultrasonics, Ferroelectrics, and Frequency Control*, vol. 35, no. 2, pp.87-101, March 1988

[He07] F. He, Q.A. Huang, and M. Qin, "A silicon directly bonded capacitive absolute pressure sensor," *Sensors and Actuators A: Physical*, vol. 135, pp. 507-514, 2007.

[Her86] G. Hernandez, *Fabry-Perot Interferometers*, Cambridge University Press: New York, 1986.

[Ino91] N. Inose and M. Ide, "A miniature hydrophone for high acoustic pressures," *Japanese Journal of Applied Physics*, vol. 31, suppl. 31-1, pp. 272-273, 1991.

[Ino03] N Inoue, T. Nakura, Y. Hayashi, "Low thermal-budget process of sputtered-PZT capacitor over multilevel metallization," *IEEE Transactions of Electron Devices*, vol. 50, no. 10, October 2003.

[Jam15] A. Jamshidi-Rad and F. Ueberle, "An optical hydrophone for the single-shot field measurements of high power pressure fields," *Acta Physica Polonica A*, vol. 127, no. 1, 2015. 66

[Khu11] B.T. Khuri-Yakub and Ö. Oralkan, "Capacitive micromachined ultrasonic transducers for medical imaging

[Kil11] O. Kilic, M.J.F. Digonnet, G.S. Kino, O. Solgaard, "Miniature photonic-crystal hydrophone optimized for ocean acoustics," *Journal of the Acoustical Society of America*, vol. 129, no. 4, pp. 1837-1850, April 2011.

[Kim12] K. Kim, S. Zhang, G. Salazar, and X. Jiang, "Design, fabrication, and characterization of high temperature piezoelectric vibration sensors using YCOB crystals," *Sensors and Actuators A: Physical*, vol. 178, pp. 40-48, 2012.

[Kin82] L. E. Kinsler, A. R. Frey, A. B. Coppens, and J. V. Sanders, *Fundamentals of Acoustics*, New York: Wiley, 1982.

[Köy18] H. Köymen, A. Atalar, S. Guler, I. Köymen, A.S. Tasdelen, and A. Unlugedik, "Unbiased charger circular CMUT Microphone: Lumped-Element Modeling and Performance," *IEEE Transactions on Ultrasonics, Ferroelectrics, and Frequency Control*, vol. 5, no. 1, January 2018.

[Kni04] J. Knight, J. McLean, and F.L. Degertekin, "Low temperature fabrication of immersion capacitive micromachined ultrasonic transducers on silicon and dielectric substrates," *IEEE*

Transactions of Ultrasonics, Ferroelectrics, and Frequency Control, vol. 51, no. 10, October 2004.

[Kra19] Krayden, Inc., "XIAMETER® PMX-200 Silicone Fluid, 5-20 cSt," <https://krayden.com/technical-data-sheet/dow_pmx-200_10cs_tds/> Visited March 13, 2019.

[Lad98] I. Ladabaum, X. Jin, H.T. Soh, A. Atalar, and B.T. Khuri-Yakub, "Surface micromachined ultrasonic transducers," *IEEE Transactions on Ultrasonics, Ferroelectrics, and Frequency Control*, vol. 45, no. 3, May 1998.

[Lee14] H.J. Lee, S. Zhang, Y. Bar-Cohen, and S. Sherrit, "High temperature, high power piezoelectric composite transducers," *Sensors*, vol. 14, pp. 14526-14522, 2014.

[Li97] T. Li, P. Zawadazki, and R.A. Stall, "Microstructure and properties of PbZr1-xTixO3 thin films made by one and two step metalorganic chemical vapor deposition," *Integrated Ferroelectrics*, 18:1-4, 155-169, 1997.

[Lit10] R.J. Littrell, "High performance piezoelectric MEMS microphones," PhD Thesis, University of Michigan, 2010.

[Lum96] P. Lum, M. Greenstein, C. Grossman, and T.L. Szabo, "High-frequency membrane hydrophone," *IEEE Transactions on Ultrasonics, Ferroelectrics, and Frequency Control*, vol. 43, no. 4, July 1996.

[Luo15] X. Luo, "Microtechnologies for discharge-based sensors" Ph.D. dissertation, University of Michigan, 2015.

[Luo16] X. Luo and Y.B. Gianchandani, "A 100 μm diameter capacitive pressure sensor with 50 MPa dynamic range," *Journal of Micromechanics and Microengineering*, vol. 26, no. 4, 2016.

[Mar07a] D.T. Martin, "Design, fabrication, and characterization of a MEMS dual-backplate capacitive microphone," Ph.D. dissertation, University of Florida, 2007.

[Mar07b] D.T. Martin, J. Liu, K. Kadirvel, R.M. Fox, M. Sheplak, and T. Nishida, "A micromachined dual-backplate capacitive microphone for aeroacoustic measurements," *Journal of Microelectromechanical Systems*, vol. 16, no. 6, 2007.

[Mar14] B. Marion, "Cross-well imaging offers higher resolution," in *The American Oil and Gas Reporter*, January 2014.

[McL03] J. McLean and F.L. Degertekin, "Interdigital capacitive micromachined ultrasonic transducers for sensing and pumping in microfluidic applications," *12th International Conference on Solid State Sensors, Actuators, and Microsystems*, Boston, June 8-12, 2003.

[Men16] L. Mengran, Z. Guojun, S. Xiaopeng, L. Yuan, and Z. Wendong, "Design of the monolithic integrated array MEMS hydrophone," *IEEE Sensors Journal*, vol. 16, no. 4, 2016.

[Moo10a] S. Choi, H. Lee, and W. Moon, “A micro-machined piezoelectric hydrophone with hydrostatically balanced air backing,” *Sensors and Actuators A: Physical*, vol. 158, pp. 60-71, 2010.

[Moo10b] S. Choi, H. Lee, and W. Moon, “A micro-machined piezoelectric flexural-mode hydrophone with air backing: A hydrostatic pressure-balancing mechanism for integrity preservation,” *Journal of the Acoustical Society of America*, vol. 128, no. 3, September 2010.

[Nik09] A. Nikoozadeh, Ö. Oralkan, M. Gencel, J.W. Choe, D.N. Stephens, A. de la Rama, P. Chen, K. Thomenius, A. Dentinger, D. Wildes, K. Shivkumar, A. Mahajan, M. O’Donnell, D. Sahn, and P.T. Khuri-Yakub, “Forward-looking volumetric intracardiac imaging using a fully integrated CMUT ring array,” *2009 IEEE International Ultrasonics Symposium Proceedings*, pp. 511-514, 2009.

[Oly18] [Oly18] *Panametrics – NDT Ultrasonic Transducers*, Olympus, Available: http://www.epsilon-ndt.com/upload/file/problar-ve-aksesuarlar-.pdf, Accessed October 2018.

[Ope13] *Smartball Flowable Pressure and Temperature Micro-recorder*, Openfield Technology, Versailles, France, 2013.

[Ora06] Ö. Oralkan, B. Bayram, G.G. Yaralioglu, A.S. Ergun, M. Kupnik, D.T. Yeh, I.O. Wygant, and B.T. Khuri-Yakub, “Experimental characterization of collapse-mode CMUT operation,” *IEEE Transactions on Ultrasonics, Ferroelectrics, and Frequency Control*, vol. 53, no. 8, August 2006.

[Par03] J.S. Park and Y.B. Gianchandani, “A servo-controlled capacitive pressure sensor using a capped-cylinder structure microfabricated by a three-mask process,” *Journal of Microelectromechanical Systems*, vol. 12, no. 2, April 2003.

[Pla87] M. Platte, “PVDF Ultrasonic Transducers,” *Ferroelectrics*, vol. 75, pp. 327-337, 1987.

[Red60] M. Redwood, *Mechanical Waveguides*, Pergamon Press: New York, 1960, Online Access December 2018.

[Rez13] M Rezaei, J. Lueke, D. Raboud, W. Moussa, “Challenges in fabrication and testing of piezoelectric MEMS with a particular focus on energy harvesters,” *Microsyst Technol*, (2013) 19:1195-1219.

[Sch94] P.R. Scheeper, A.G.H. van der Donk, W. Olthius, and P. Bergveld, “A review of silicon microphones,” *Sensors and Actuators A*, vol. 44, pp. 1-11, 1994.

[Sch06] Schlumberger, “Crosswell Electromagnetic Resistivity Imaging: Illuminating the Reservoir,” *Middle East & Asia Reservoir Review*, no. 7, pp. 24-33, Nov. 2006.

[Sel85] A.R. Selfridge, “Approximate material properties in isotropic materials,” *IEEE Transactions on Sonics and Ultrasonics*, vol. SU-32, no. 3, 1985.

[Sen01] S.D. Senturia, *Microsystem Design*, Springer: New Delhi, 2001.

[Shi15] Z. Shi, Y. Chen, M. Yu, S. Zhou, N. Al-Khanferi, “Development and Field Evaluation of a Distributed Microchip Downhole Measurement System,” *SPE Digital Energy Conference and Exhibition*, The Woodlands, Texas, Mar. 2015.

[Sil11] *C8051F99x-C8051F98x Datasheet*, Silicon Laboratories, Austin, Texas, 2011.

[Sin81] Sinha, M.C., Owen, T.R.E. & Mason, M. Marine Geophysical Researches (1981) 5: 173.

[Smi07] S. Smith, T.B. Tang, J.G. Terry, J.T.M. Stevenson, B.W. Flynn, H.M. Reekie, A.F. Murray, A.M. Gundlach, D. Renshaw, B. Dhillon, A. Ohtori, Y. Inoue and A.J. Walton, “Development of a miniaturized drug delivery system with wireless power transfer and communication,” *IET Nanobiotechnology*, vol. 1, no. 5, pp. 80-86, 2007.

[Son15] J. Song, C. Xue, C. He, R. Zhang, L. Mu, J. Cui, J. Miao, Y. Liu, W. Zhang, “Capacitive micromachined ultrasonic transducers (CMUTs) for underwater imaging applications,” *Sensors*, vol. 15, pp. 23205-23217, 2015.

[Sta93] J. Staudenraus and W. Eisenmenger, “Fibre-optic probe hydrophone for ultrasonic and shock-wave measurements in water,” *Ultrasonics*, vol. 31, no. 4, pp. 267-273, 1993.

[Ste18] STE Oil Company, Inc., “Crystal Plus Oil 70FG,” <http://www.steoil.com/wp-content/themes/steoil/pdf/techdata-crystalplus70fg.pdf> Visited December 16, 2018.

[Sul78] T.D. Sullivan and J.M. Powers, “Piezoelectric polymer flexural disk hydrophone,” *Journal of the Acoustic Society of America*, vol. 63, no. 5, 1978.

[Sus05] M. Suster, N. Chaimanonart, J. Guo, W.H. Ko, and D.J. Young, “Remote-Powered High-Performance Strain Sensing Microsystem,” *18th IEEE International Conference on Micro Electro Mechanical Systems*, pp. 255-258, 2005.

[Tim59] S. Timoshenko and S. Woinowsky-Krieger, *Theory of Plates and Shells*, New York: McGraw-Hill, 1959.

[Tro04] S. Trolier-Mckinstry and P. Muralt, “Thin film piezoelectrics for MEMS,” *Journal or Electroceramics*, vol. 12, pp. 7-17, 2004.

[Wan17] R. Wang, Y. Liu, W. Xu, B. Bai, G. Zhang, J. Liu, J. Xiong, W. Zhang, C. Xue, and B. Zhang, “A ‘fitness-wheel-shaped’ MEMS vector hydrophone for 3D spatial acoustic orientation,” *Journal of Micromechanics and Microengineering*, vol. 27, 2017.

[Wen13] Y. Wencai, *Reflection Seismology: Theory, Data Processing, and Interpretation*, Elsevier, 2014 69

[Whi05] R.D. White, L. Cheng, and K. Grosh, “Capacitively sensed micromachined hydrophone with viscous fluid-structure coupling,” *Proceedings of SPIE*, vol. 5718, Bellingham, WA, 2005.

[Wij11] M.B.J Wijesundara and R.G. Azevedo, *Silicon Carbide Microsystems for Harsh Environments*, Springer: New York, 2011.
[Wis09] K. D. Wise, "Wireless integrated microsystems: Wearable and implantable devices for improved health care," International Conference on Solid-State Sensors, Actuators and Microsystems (Transducers), Denver, CO, 2009, pp. 1-8.

[Wod11] S. Wodin-Schwartz, M.W. Chan, K.R. Mansukhani, A.P. Pisano, and D.G. Senesky, “MEMS sensors for down-hole monitoring of geothermal energy systems,” in *Proceedings of the ASME 2011 5th International Conference on Energy Sustainability*, Washington, DC, USA, 2011.

[Yam15] F.Y. Yamaner, X. Zhang, and O. Oralkan, “A three-mask process for fabricating vacuum-sealed capacitive micromachined ultrasonic transducers using anodic bonding,” *IEEE Transactions on Ultrasonics, Ferroelectrics, and Frequency Control*, vol. 62, no. 5, May 2015.

[Yu12] M. Yu, S. He, Y. Chen, N. Takach, P. LoPresti, S. Zhou, N. Al-Khanferi, “A Distributed Microchip System for Subsurface Measurement,” *SPE Annual Technical Conference and Exhibition*, San Antonio, Texas, Oct. 2012.

[Zhu07] X. Zhuang, A. Nikoozadeh, M. A. Beasley, G.G. Yarioglu, B.T. Khuri-Yakub, and B.L. Pruitt, “Biocompatible coatings for CMUTs in a harsh, aqueous environment,” *Journal of Micromechanics and Microengineering*, vol. 17, pp 994-1001, 2007.